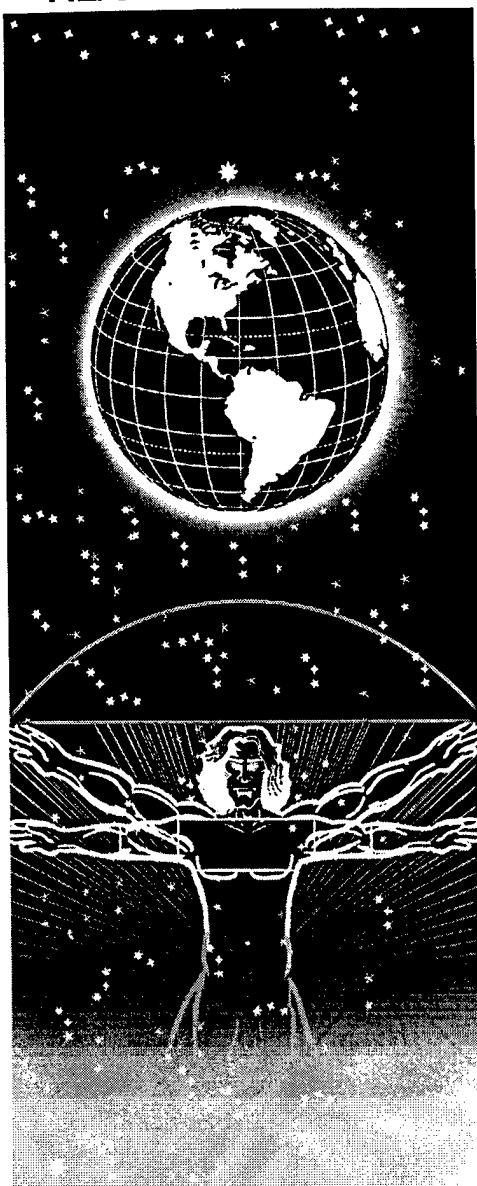


UNITED STATES AIR FORCE
ARMSTRONG LABORATORY

Electromagnetic Radiation Inverse
Scattering

Thomas Roberts

Operational Technologies Corporation
4100 NW Loop 410
San Antonio, TX 78229



19980410 010

August 1997

DTIC QUALITY INSPECTED 3

*Approved for public release;
distribution is unlimited.*

Occupational and Environmental Health
Directorate
Mathematical Products Division
2503 Gillingham Street
Brooks Air Force Base TX 78235-5102

NOTICES

This report is published as received and has not been edited by the staff of the Directed Energy Bioeffects Division, Human Effectiveness Directorate.

Publication of this report does not constitute approval or disapproval of the ideas or findings. It is published in the interest of scientific and technical information (STINFO) exchange.

When Government drawings, specifications, or other data are used for any purpose other than in connection with a definitely Government-related procurement, the United States Government incurs no responsibility or any obligation whatsoever. The fact that the Government may have formulated or in any way supplied the said drawings, specifications, or other data, is not to be regarded by implication, or otherwise in any manner construed, as licensing the holder or any other person or corporation; or as conveying any rights or permission to manufacture, use, or sell any patented invention that may in any way be related thereto.

The mention of trade names or commercial products in this publication is for illustration purposes and does not constitute endorsement or recommendation for use by the United State Air Force.

The Office of Public Affairs has reviewed this report, and it is releasable to the National Technical Information Service, where it will be available to the general public, including foreign nationals.

This report has been reviewed and is approved for publication.

Government agencies and their contractors registered with Defense Technical Information Center (DTIC) should direct requests for copies to: Defense Technical Information Center, 8725 John J. Kingman Rd., STE 0944, Ft. Belvoir, VA 22060-6218.

Non-Government agencies may purchase copies of this report from: National Technical Information Services (NTIS), 5285 Port Royal Road, Springfield, VA 22161-2103.



RICHARD L. MILLER, PhD
Chief, Directed Energy Bioeffects Division

REPORT DOCUMENTATION PAGE			Form Approved OMB No. 0704-0188	
Public reporting burden for this collection of information is estimated to average 1 hour per response, including the time for reviewing instructions, searching existing data sources, gathering and maintaining the data needed, and completing and reviewing the collection of information. Send comments regarding this burden estimate or any other aspect of this collection of information, including suggestions for reducing this burden, to Washington Headquarters Services, Directorate for Information Operations and Reports, 1215 Jefferson Davis Highway, Suite 1204, Arlington, VA 22202-4302, and to the Office of Management and Budget, Paperwork Reduction Project (0704-0188), Washington, DC 20503.				
1. AGENCY USE ONLY (Leave blank)	2. REPORT DATE August 1997	3. REPORT TYPE AND DATES COVERED Final, April 1993 - October 1994		
4. TITLE AND SUBTITLE Electromagnetic Radiation Inverse Scattering		5. FUNDING NUMBERS C: F41624-92-D-4001 PE: 62202F PR: 7757 TA: OS WU: 03		
6. AUTHOR(S) Thomas Roberts				
7. PERFORMING ORGANIZATION NAME(S) AND ADDRESS(ES) Operational Technologies Corporation 4100 NW Loop 410 San Antonio Texas 78229		8. PERFORMING ORGANIZATION REPORT NUMBER		
9. SPONSORING/MONITORING AGENCY NAME(S) AND ADDRESS(ES) Armstrong Laboratory Occupational and Environmental Health Directorate Mathematical Products Division 2503 Gillingham Street Brooks Air Force Base Texas 78235-5102		10. SPONSORING/MONITORING AGENCY REPORT NUMBER AL/OE-TR-1997-0107		
11. SUPPLEMENTARY NOTES				
12a. DISTRIBUTION AVAILABILITY STATEMENT Approved for public release; distribution is unlimited.			12b. DISTRIBUTION CODE	
13. ABSTRACT (Maximum 200 words) The report is divided into four parts. Part one is about nonlinear microwave amplification and the further use of nonlinear Schrodinger equations to model amplifiers. Part two is about speeds of frequency components of electromagnetic pulses, and a related inversion method. Our numerical computation of precursors shows that damping increases the speed of frequency components to a degree that is consistent with energy velocity. The speed-up here is slight, and a medium that has been called "highly absorptive" exhibits no speed-up. These small effects lead us to question the extent to which energy velocity would be more useful than group velocity in the laboratory. We also introduce an especially simple method for measuring permittivity. Part three is about an inversion method for depth-dependent dispersive objects that are flat, and whose properties vary only with depth. Tissue and soil are discretely layered examples of such media. But this paper's algorithm also applies to dispersive media that are continuously layered. A time-domain layer stripping method that uses wave splitting and Krueger-Ochs Green functions is presented. Part four is about general rules of pulse propagation for dispersive media, with applications to inversion. We develop some new methods for describing pulse propagation for general dispersive media, using a Debye model for water as an example. Short-pulse, long-pulse, short-time, and long-time approximations are presented. We explain a factor-of-nine effect in the speed of waves in water, which seems to have been previously unnoticed. We provide sharp upper bounds for the propagated amplitude and reduce the computation of those bounds to a calculator exercise. These bounds may be useful in controlling the electromagnetic interference on damage produced in dispersive media.				
14. SUBJECT TERMS Electromagnetic radiation Inverse scattering			15. NUMBER OF PAGES 120	
			16. PRICE CODE	
17. SECURITY CLASSIFICATION OF REPORT Unclassified	18. SECURITY CLASSIFICATION OF THIS PAGE Unclassified	19. SECURITY CLASSIFICATION OF ABSTRACT Unclassified	20. LIMITATION OF ABSTRACT UL	

THIS PAGE INTENTIONALLY LEFT BLANK

TABLE OF CONTENTS

	Page
I COMMENT ON A PAPER'S NONLINEAR-AMPLIFICATION MODEL	
Equations	I-1
Experimental Validation	I-4
Conclusion	I-7
References	I-8
 II SPEEDS AND INVERSION	
Introduction	II-1
Instantaneous Frequency	II-7
Wave Speed	II-12
Debye Media	II-23
Comparisons of Group and Energy Velocity	II-25
Open Questions	II-25
Empirical Similarities	II-25
Empirical Differences	II-28
Elementary Inversion	II-29
Conclusion	II-32
Appendix A: Direct-Scattering Algorithm	II-32
Appendix B; Error Bars	II-36

	Page
Appendix C: Perturbation of Inflection Points	II-41
References	II-42
 III INVERSION METHOD FOR DEPTH-DEPENDENT DISPERSIVE MEDIA	
Problem Statement	III-1
Method of Solution	III-3
Computational Algorithm	III-5
Related Work	III-8
Conclusion	III-9
References	III-9
 IV PROPAGATION AND RELATED TOPICS, INCLUDING INVERSION	
Introduction	IV-1
PDE Formulation and Results	IV-3
PDEs	IV-3
Green Functions	IV-6
Derivations	IV-13
PDEs	IV-13
Green Functions	IV-15
Numerical Validation and Laboratory Experiments	IV-27
Conclusion	IV-36
Appendix A: Error Estimates	IV-37

	Page
References	IV-42

THIS PAGE INTENTIONALLY LEFT BLANK

Summary

Each item of work described in this report was paid for, in whole or in part, by the present contract. There are four items. The first item is about nonlinear microwave amplification. The second item is about speeds of frequency components of electromagnetic pulses, and a related inversion method. The third item is about an inversion method for depth-dependent dispersive media, which uses electromagnetic pulses. The fourth item is about general rules of pulse propagation in dispersive media, with applications to inversion.

Some of the work was done jointly with others or with some help from others. I will now list these people and identify those who work in San Antonio. For the first item I would like to thank Gary Thomas who told me about an error in an equation and its correction. A project with the Naval Weapons Support Center required rederivations done in this first work item. The second item was done jointly with Mike Hobart. Some computer programs came from Robert Krueger and Ronald Winther, and I am grateful for conversations about error bars with Phelps Crump, who is a defense contractor working in San Antonio. The fourth item was done jointly with Peter Petropoulos while he was employed by Optech, and Fred German allowed us to use his finite-difference program.

This summary concludes with a brief, item-by-item description of the remainder of this report.

Comment on a Paper's Nonlinear-Amplification Model

The paper commented on is significant because its claims of laboratory success have motivated further use of nonlinear Schrödinger equations to model amplifiers. Some of the paper's inaccurate equations are corrected here, and others identified. Questions are also raised about the claims of success in the laboratory.

Speeds and Inversion

Our numerical computation of precursors shows that damping increases the speed of frequency components to a degree that is consistent with energy velocity. The speed-up here is slight, and a medium that has been called "highly absorptive" exhibits no speed-up. These small effects lead us to question the extent to which energy velocity would be more useful than group velocity in the laboratory. We also introduce an especially simple method for measuring permittivity. The method is useful when damping affects wave speed no more than slightly, as happens in all numerical simulations cited or reported here.

Inversion Method for Depth-dependent Dispersive Media

This item describes an inverse scattering algorithm for electromagnetically dispersive objects that are flat, and whose properties vary only with depth. Tissue and soil are discretely layered examples of such media, but this paper's algorithm also applies to dispersive media that are continuously layered. The inversion algorithm uses time-dependent reflection data as a function of the angle of incidence. These data are represented by a function of two variables $R^\theta(t)$. A count of the variables

suggests that the data $R^\theta(t)$ should be sufficient to determine the two-variable function $g(x, t)$ that represents depth-dependent dispersion. A time-domain layer stripping method that uses wave splitting and Krueger-Ochs Green functions is presented.

Propagation and Related Topics, Including Inversion

We develop some new methods for describing pulse propagation for general dispersive media, using a Debye model for water as an example. Short-pulse, long-pulse, short-time, and long-time approximations are presented. We explain a factor-of-nine effect in the speed of waves in water, which seems to have been previously unnoticed. We also study the following problem: Knowing only the peak amplitude and power density of an incident pulse, what can be said about the peak amplitude of the propagated pulse? We provide sharp upper bounds for the propagated amplitude and reduce the computation of those bounds to a calculator exercise. These bounds may be useful in controlling the electromagnetic interference or damage produced in dispersive media.

Comment on a Paper's Nonlinear-Amplification Model

Continued citation of Gary E. Thomas's paper [1] makes comment worthwhile. In this comment, the numbers of equations, figures, tables, and sections are of those in [1].

Equations

This section identifies twelve inaccurate equations in [1], which are corrected here or proven inaccurate. The inaccurate equations are (10a), (10b), (11)–(13), (15a), (15b), (21), the first two unnumbered equations that follow (15b), and two of the equations between (33) and (34). The signs of the paper's functions J_1 , $-B_0$, and $-C_0$ affect the accuracy of (34) and the equation for τ that is between (33)

and (34). Those two equations are replaced here by ones that are valid regardless of the signs of J_1 , $-B_0$, and $-C_0$.

Each equation in the following list corrects a corresponding equation in [1], or is used immediately below to correct a larger concept.

$$E = A \operatorname{sech}[A(x - u_e t)/\sqrt{2}] \exp[iu_e(x - u_c t)/2] \quad (10a)$$

$$E = B \tanh[B(x + u_e t)/\sqrt{2}] \exp[iu_e(x + u_c t)/2] \quad (10b)$$

$$\partial_\xi^2 f + 6(\operatorname{sech}^2 \xi) f - (1 - 2k_z^2/A^2) f \approx +2\gamma g/A^2 \quad (15a)$$

$$\partial_\xi^2 g + 2(\operatorname{sech}^2 \xi) g - (1 - 2k_z^2/A^2) g \approx -2\gamma f/A^2 \quad (15b)$$

$$\xi = A(x - u_e t)/\sqrt{2} \quad (15c)$$

$$K^2 = 2k_z^2/A^2 \text{ and } \Gamma = 2\gamma/A^2 \quad (15d)$$

$$u_e = u_c \pm \sqrt{u_c^2 + 2A^2} \quad (21)$$

$$ia\partial_t E + b\partial_x^2 E + c\partial_z^2 E + J|E|^2 E = 0 \quad (33a)$$

$$a = -2\omega D_0 \quad b = -2B_0 k_x^2 \quad c = C_0 \quad J = J_1 \quad (33b)$$

$$\tau = t|J/a| \quad \xi = x\sqrt{|J/b|} \quad \zeta = z\sqrt{|J/c|} \quad (33c)$$

$$\operatorname{sign}(a/J) = 1 \quad (33d)$$

$$i\partial_\tau E + [\operatorname{sign}(b/J)]\partial_\xi^2 E + [\operatorname{sign}(c/J)]\partial_\zeta^2 E + |E|^2 E = 0 \quad (34)$$

In (10a): A , u_e , and u_c are real-valued constants that satisfy $u_e(2u_c - u_e) = 2A^2$ and $u_e(u_e - 2u_c) > 0$. In (10b): B , u_e , and u_c are new real-valued constants that satisfy $u_e(2u_c - u_e) = 2B^2$ and $u_e(u_e - 2u_c) > 0$.

Table I and Fig. 3 are from [1, Ref. 8]—which is the eighth reference in [1]—provided (15d) replaces similar equations in [1], and provided [1, Ref. 8] uses, in its notation, $N^2 = 1$. Reference [1] does not say whether [1, Ref. 8] uses $N^2 = 1$.

Equations (33)–(34) correct a corresponding set of equations in [1] only if a , b , c , and J are real valued and independent of the real variables t , x , and z . Equation (33d) is not in [1]; the equation comes from [2]. There are no more corrections.

Equation (11) is false because it and definition (9) have identical right sides, though the left sides have different units. Equation (11) is not from [1, Ref. 7], nor does (11), (12), or (13) follow from direct application of [1, Ref. 7]. The right sides of (9), (12), and (13) have identical units, though the units of the left sides of (12) and (13) differ from the units of the left side of definition (9). That is, (11)–(13) have errors. Those equations are a foundation for the paper's predictions about power.

Some work reported after publication of [1] relates to foundational equations mentioned in the previous paragraph. In particular, much of (8)–(13) concerns the energy-like term (9), which is said to be conserved for a nonlinear Schrödinger equation with one spacial variable, and to be unconserved for spacial dimension two. Later work [3] shows that $i\partial_t E + \partial_x^2 E + \partial_z^2 E + |E|^2 E = 0$ implies that the different energy-like term $\iint dx dz (|\partial_x E|^2 + |\partial_z E|^2 - |E|^4/2)$ is conserved and the term $\iint dx dz |E|^2$, which is proportional to an integral of the right side of (13), also is conserved.

This section has identified twelve inaccurate equations and corrected most of them. The focus has been on equations themselves, not their relevance in modeling amplifiers. The strongest argument in [1] for the relevance of its equations is that

they are said to make predictions that are validated experimentally. However, the degree to which this comment's corrections would affect those predictions is unknown because [1] omits numerical values of some important variables. (The variables are used in (36)–(38) and (44) to define apparently significant signs of coefficients in a nonlinear Schrödinger equation (33).) That is, predictions in [1] are questionable because of errors, but the magnitude of the errors is unknown because the predictions are not reproducible.

Experimental Validation

The model in [1] was derived nonrigorously, so its scientific relevance is based on claims of experimental validation. The paper says that predictions and experiments agree closely, so if the numerical effect of errors in [1] is large, then there is no need to examine [1] further. However, if the errors affect predictions only slightly, then the scientific relevance of [1] relies on claims that (flawed) predictions agree with experiments. This section examines all such claims of experimental validation.

Figure 10 and Tables II and III contain all the experimental data in [1], and Table II is illustrated in Figs. 6 and 7. Every claim of experimental validation naturally refers to those data. The claims are in the second and third paragraphs of Section V, and in the fourth and fifth paragraphs of Section VI. We will examine claims in that order.

The claims of experimental validation that concern Tables II and III are affected by “transition shifts.” The shifts change numerical predictions. Shifts are explained qualitatively in [1], but their numerical values are unexplained. One shift in Fig. 4 changes a prediction by an unexplained 32%.

Let us examine at length a single prediction. Section V predicts an increase in the slope of a graph at the voltage $0.63V_H$, which is shifted by 17% to $0.74V_H$ in Fig. 4. The text says that experimental data have an increasing slope at the nearby voltage $0.79V_H$, and Fig. 7 is cited. Linear interpolation is used in every interval of Fig. 7, except for one that has an unexplained, nonlinear interpolation. The initial slope of the nonlinear interpolation is chosen to agree with the predicted increase; yet the slope *decreases* to the right of $0.79V_H$, and throughout the interval. Fig. 6, which has the same data as Fig. 7, illustrates the decreasing slope more plainly. Thus, two graphs contradict a predicted increase in slope, while the text claims close agreement. In another matter concerning the same prediction, a table does not distinguish experiment from theory. In particular, the voltage $0.79V_H$ comes from analysis of experimental data, but Table II portrays that voltage as a prediction. A larger set of related data also does not clearly establish that theory and experiment agree. For instance, a 7.2kV "predicted value" is placed in the same row of Table II as a 7.2kV applied voltage, a -13.7dBm power, a 240.0 degree phase shift, and a 0.02A current; but the relation of the 7.2kV prediction to any of the four measurements in its row is unexplained. Is the unexplained placement of a 7.2kV prediction meant to support the text's claim that theory and experiment agree? Does that placement rely on the extraordinary interpolation technique that earlier produced two contradictions? Those questions can be repeated for the other predictions in Table II, which are also affected by shifts. Questions have now been raised about the claims of experimental validation that refer to Table II. Those claims are in the second paragraph of Section V.

Only one claim of experimental validation [1, page 32] mentions Table III. The claim refers to a voltage $1.13V_H$, which is shifted twice: first by 8% to $1.22V_H$; second, by an unmentioned quantity whose sign might be implied by the text, which says, "For a forward-wave CFA, negative phase velocity effects increase with increasing frequency." This doubly-shifted, indeterminate voltage is said to explain a feature in Table III. The resulting claim of experimental validation is unconvincing because the numerical value of the first shift is unexplained and the numerical value of the second shift is unmentioned.

Questions have now been raised about the claims of experimental validation that concern Tables II and III. All validation claims will have been examined once we consider those that refer to Fig. 10. The claims about Fig. 10 are in the fourth and fifth paragraphs of Section V. The subject is phase shifts.

Phase predictions in (23) are affected by an error in (21), which is corrected in the previous section of this comment. It is not clear whether corrected predictions would agree with the data presented. The paper says, "phase shifts are scaled according to power output," but the paper does not further define a scaling formula with which the variable A in (21) could be replaced by the power graphed in Fig. 6. A scaling formula would allow the phase in (23) to be graphed, but the paper offers only qualitative analysis and sketches. Scaling, which is not fully explained, is a crucial part of claims that qualitative analysis and data agree closely. Here and in the case of transition shifts, experimental validation relies on the accuracy of incompletely-reported work.

Conclusion

Reference [1] apparently is the first paper to use a nonlinear Schrödinger equation to describe microwave amplifiers. The model in [1] is not rigorously derived; instead, the model's relation to amplifiers is based on claims that predictions and experiments agree closely. Those claims have motivated other papers that use similar nonlinear models.

This comment has examined some equations that underly predictions, and it has reviewed all claims of experimental validation. Questions have been raised about both the equations and the claims of validation.

Although no attempt has been made to re-derive every equation in [1], most of the twelve known inaccurate equations in [1] have been corrected here. The effect of corrections on numerical predictions in [1] is unknown because the values of some critical parameters are omitted from [1]. Another fundamental concern is the paper's development of an energy-like term (9). That development is flawed and uncorrected, yet it is a foundation for predictions about an amplifier's power.

The effect of errors on numerical predictions in [1] has unknown magnitude, so it is possible that the effect is small. In that case, claims of experimental validation are crucial because they are the only connection between [1] and the amplifiers it models. Most of those claims involve "transition shifts," which are large changes in predictions. The numerical values of shifts are unexplained, but not every prediction is shifted: all unshifted predictions are "scaled" in a way that is also not fully explained. Shifts and scalings are both documented incompletely, and they both bring predictions into closer agreement with experiments. The paper's most

prominent claim—the subject of Fig. 7—relies on both an unexplained 17% shift and an extraordinarily questionable interpolation.

In summary, several papers have been motivated by the development in [1] of a nonlinear-Schrödinger-equation (NLS) model. If the numerical effect of twelve inaccurate equations in [1] is not too large, then the argument for an NLS model relies on shifts, scalings, and questionable interpolations. The shifts and scalings will not be reproducible unless [1] is further documented.

References

- [1] Gary E. Thomas, "The Nonlinear Operation of a Microwave Crossed-Field Amplifier," *IEEE Transactions on Electron Devices*, vol. ED-28, no. 1, pp. 27–36, January 1981.
- [2] Gary E. Thomas, "Solitons and non-linear gyro-TWT theory," *Int. J. Electronics*, vol. 51, no. 4, pp. 395–413, October 1981.
- [3] Mark J. Ablowitz and Harvey Segur, *Solitons and the Inverse Scattering Transform*. Philadelphia: SIAM, 1981, p. 258. Let $A = E/\sqrt{2}$ in (3.8.46) and (3.8.47).
- [4] Thomas M. Roberts and Harold A. Sabbagh, "Review of Nonlinear Analysis for Crossed-Field Amplifiers," final report to Naval Weapons Support Center, Code 80312, Crane, Indiana, 47553, 20 January 1989.

1. INTRODUCTION

There are several velocities of light,^{1,2} among which group and energy velocity predict most successfully the speeds of a pulse's frequency components. This paper compares those group- and energy-velocity predictions, and says that two predictions differ significantly only if there is numerical evidence that the difference could be noticed in a laboratory. A simple method for measuring permittivity is also examined from an empirical point of view, and is found to be useful in some cases.

Group velocity $v_g = d\omega/dk$ (with $k = \omega\sqrt{\epsilon}/c$) is often used for undamped media, but is widely considered useless for damped media.^{1,3,4} First, we assert to the contrary that waves computed⁵ for a "highly absorptive⁵⁻⁸" medium and reported in this journal are described with equal accuracy by group and energy velocity. That is, damping negligibly affects the speed of frequency components in Ref. 5. Second, we report simulations in which damping increases speed noticeably, though slightly. Our experience of finding several media in which damping negligibly affects speed (before finding the exceptional media reported here) is more anecdotal evidence that the effect of damping on wave speed is slight. Third, we observe that precursors in waves computed for a Debye medium and reported in this journal⁹ are also consistent with a hypothesis that damping affects wave speed slightly. We view those three observations as the first numerical tests of the empirical usefulness of energy velocity. The tests are reviewed after equation (3), and in Sections 4 and 5. We conclude that there is no numerical evidence that energy velocity could be much better than group velocity at predicting speeds of frequency components that are observable in a laboratory. However, the available numerical

tests are not exhaustive, and the tests reported here tend to improve the stature of energy velocity.

Finally, we use wave speed in an elementary technique for inferring permittivity from transmitted waves. The technique is truly elementary: It is not mathematically advanced; indeed, we prove limitations. The elementary technique is worthwhile because it is simple, and potentially useful in some cases.

This paper is mainly about Lorentz media, which appear to be the only damped media for which energy velocity has been calculated explicitly.^{3, 10} Lorentz media are defined¹¹ by the Maxwell equations, $\nabla \times E = -\partial_t B$ and $\nabla \times H = \partial_t D$, and by the constitutive relations $B = \mu_0 H$ and

$$D(t) = E(t) + \int_0^\infty ds g(s) E(t-s) \quad (1)$$

$$g(t) = \omega_p^2 e^{-\delta t} \nu^{-1} \sin \nu t.$$

The media are parameterized by a plasma frequency ω_p , a damping constant δ , and a natural frequency ν . In the frequency domain, $D(\omega) = \epsilon(\omega) E(\omega)$ and

$$\epsilon(\omega) = 1 - \omega_p^2 / (\omega^2 - \omega_r^2 + 2i\delta\omega) \quad (2)$$

with $\omega_r = \sqrt{\nu^2 + \delta^2}$. Media with electric dipoles of strength ω_p^2 that oscillate with damping δ and resonant frequency ω_r as $\ddot{x} + 2\delta\dot{x} + \omega_r^2 x = \text{constant} \times e^{i\omega t}$ are Lorentz media¹¹ in the sense of (1) and (2). The frequency components of pulses in Lorentz media travel at the energy velocity³

$$v_e = c[(\text{Re}k) + \omega(\text{Im}k)/\delta]^{-1} \quad k = \text{Re}k + i\text{Im}k = \omega\sqrt{\epsilon}/c \quad (3)$$

which generalizes group velocity in the sense that³ $v_e \rightarrow v_g$ as $\delta \rightarrow 0$.

Comparisons of group and energy velocity (Section 5) may be the parts of this paper that have the most general interest. Figures 1 and 2 illustrate one such comparison of v_g and v_e , and the comparison also relies on Ref. 5. That paper computes precursors for a Lorentz medium (2) whose parameters $\langle \omega_p, \omega_r, \delta \rangle$ are on the order of 10^{16} /sec. For one computed precursor, the instantaneous frequency ω_{inst} was measured at 60 different instants. (Notice that *measurement* here refers to a numerical simulation, not a laboratory experiment.) The measurements are graphed in Fig. 6 of Ref. 5, and some of that graph's features are sketched here. All 60 measurements lie in the outer dashed regions of Figs. 1 and 2.

Figure 1 shows that v_e for the medium $\langle \omega_p, \omega_r, \delta \rangle$ of Ref. 5 and v_g for a medium $\langle \omega_p, \omega_r, 0 \rangle$ —which has the same ω_p and ω_r , but has $\delta = 0$ —differ considerably over only 5–10% of the frequency range for which Ref. 5 has measurements; but no frequency measurement actually lies in that narrow (5–10%) range. In the complementary region, where v_g and v_e are approximately equal, Fig. 6 of Ref. 5 has six unusual measurements that seem, at first, to be inconsistent with both v_e and v_g ; but those six frequency measurements are unreliable* for reasons

* The six measurements that are unreliable for our purposes are useful in the context of Ref. 5. That paper says correctly that the zigzags, or oscillations, in the graph of the six measurements are caused by interference of Sommerfeld (high frequency) and Brillouin (low frequency) parts of a precursor. The paper then

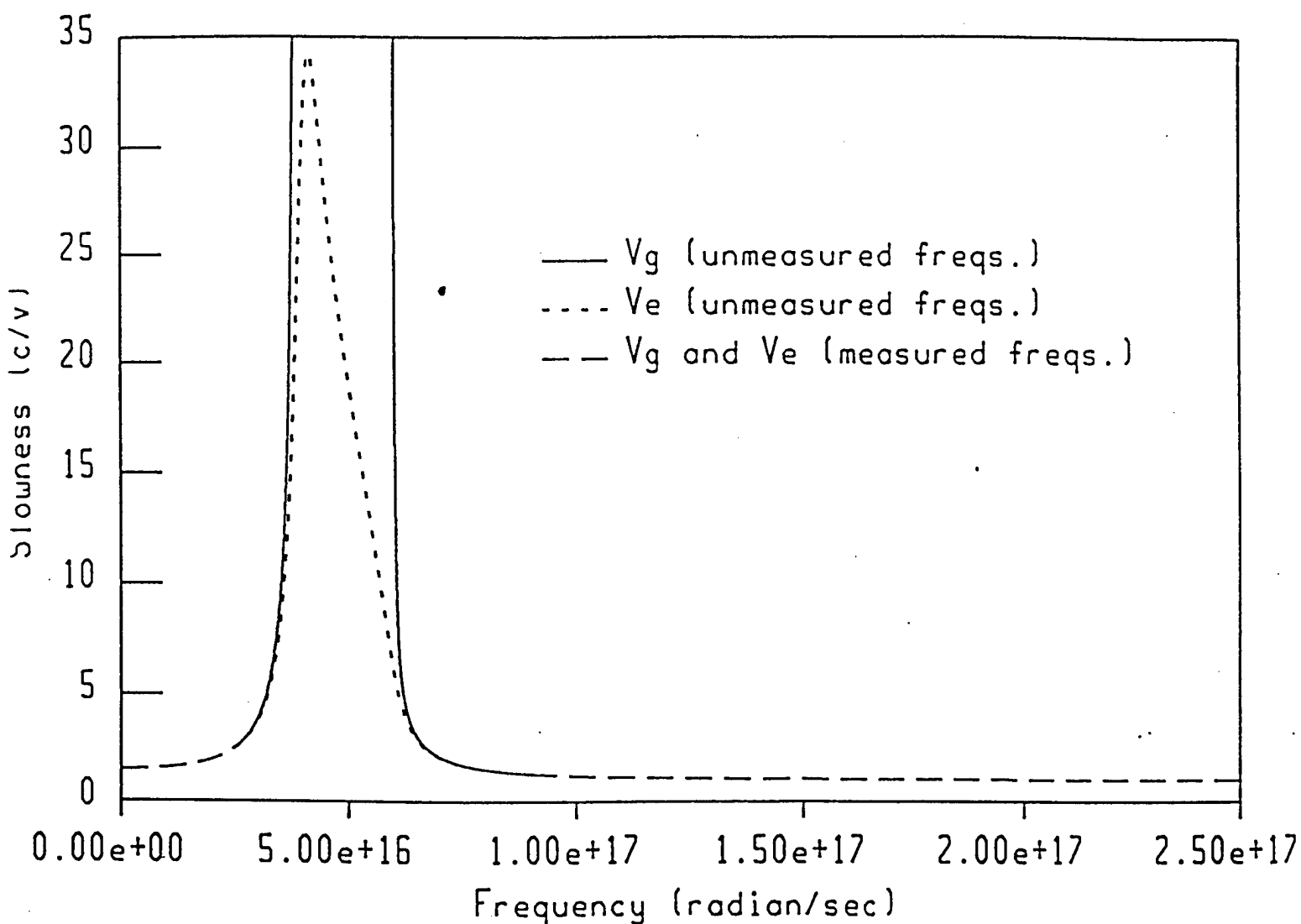


Fig. 1. Precursor measurements in Ref. 5 are equally well described by v_e for $\langle \omega_p, \omega_r, \delta \rangle$ and v_g for $\langle \omega_p, \omega_r, 0 \rangle$. Group and energy velocity differ significantly near the stop band (4×10^{16} /sec, 6×10^{16} /sec), but instantaneous frequency was not measured there.

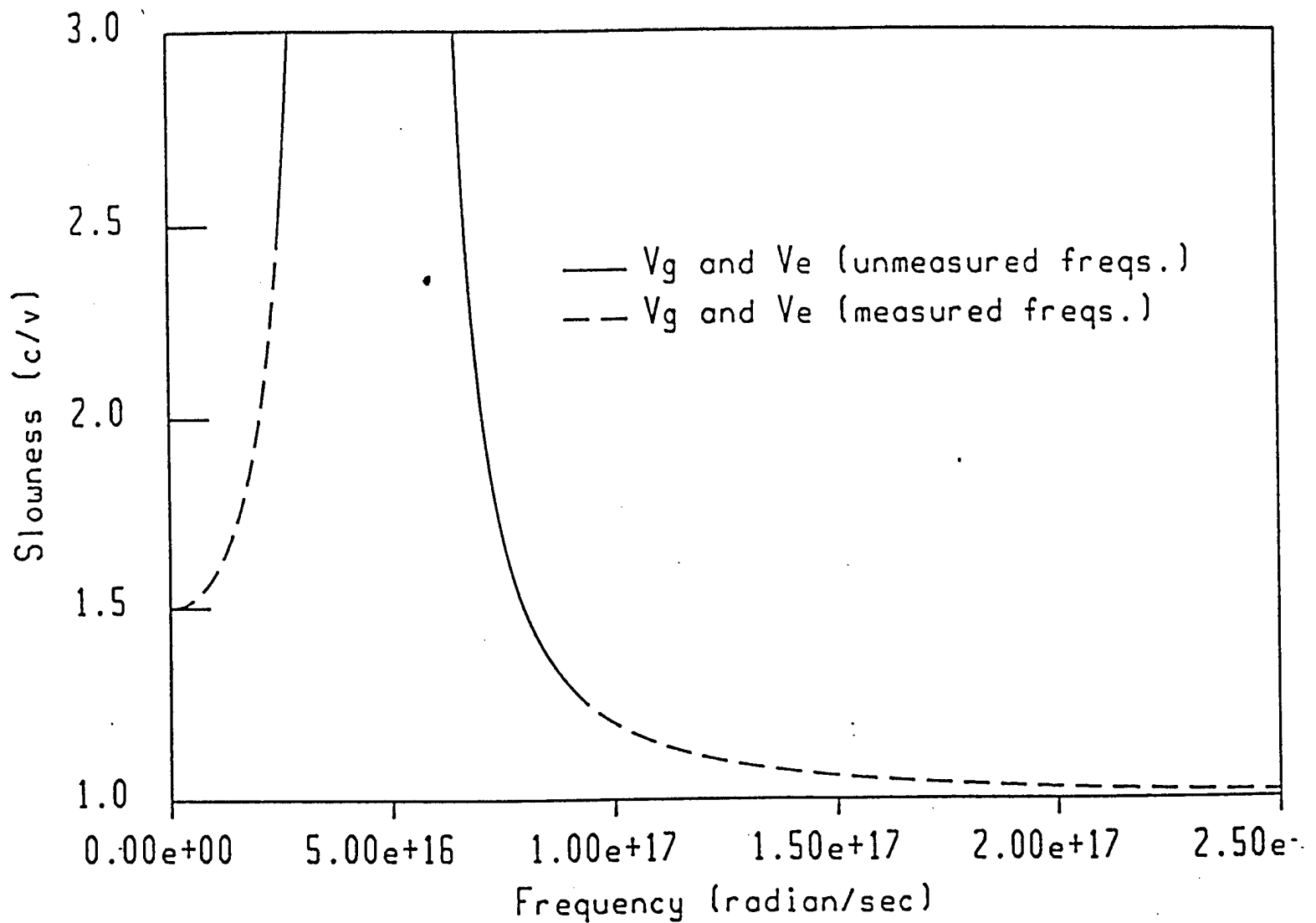


Fig. 2. Detail from Fig. 1. Group and energy velocity overlap here, to within the width of a pen stroke. In contrast, many measurements in Fig. 6 of Ref. 5 deviate from theoretical curves by the width of a few pen strokes, owing to small measurement errors.

described here in Section 5, in a discussion of "zigzags" and multiple-valued speeds. The other 54 measurements in Fig. 6 of Ref. 5 are reliable and are equally well described by v_g and v_e . Figure 2 shows the high degree of accuracy with which v_e for $\langle \omega_p, \omega_r, \delta \rangle$ and v_g for $\langle \omega_p, \omega_r, 0 \rangle$ agree over the (dashed) range of reliable measurements. This paragraph and the one previous explain our earlier statement that waves computed for one highly absorptive medium are described with equal accuracy by group and energy velocity. Section 5 compares v_g and v_e further.

The oscillator that underlies the Lorentz medium studied in Ref. 5 has a natural frequency ν that differs from the resonant frequency ω_r by 0.25%. That small difference accounts for the similar values of v_g and v_e in Fig. 2. Increasing the damping δ would broaden the frequency range over which v_e for $\langle \omega_p, \omega_r, \delta \rangle$ and v_g for $\langle \omega_p, \omega_r, 0 \rangle$ differ significantly; but, in a competing effect, a larger damping would also severely attenuate a broader range of frequency components. With those competing effects in mind, we searched for Lorentz media in which v_g and v_e would differ significantly for some frequency components that could be observed and measured. Our best results—for which the differences between v_g and v_e are the greatest we have seen—are in Section 3. The section describes what appears to be the first evidence that damping affects speed noticeably, though the effect is slight. Section 4 identifies a similar small effect in a paper⁹ on Debye media. Section 5 reviews comparisons of group and energy velocity. Section 6 introduces and examines an elementary method for measuring permittivity. The elementary method may be useful when damping affects wave speed slightly, as happens in all numerical simulations that are reported or cited here.

relates the onset of interference to a prediction.

2. INSTANTANEOUS FREQUENCY

Pleshko¹² was the first to measure in a laboratory the instantaneous frequency of a precursor, which is a frequency-modulated wave. Pleshko assumed, for the sake of measurement, that consecutive zero crossings of a time trace are separated by a half-period, as is true for a sine wave of fixed frequency. The corresponding approximation to instantaneous frequency

$$\omega_{\text{inst}} := \pi / (T - t) \quad (4)$$

is assigned to the instant half-way between zero crossings $T > t$. The zero-crossing technique is not always useful. For example, Figs. 3 and 4 have no zero crossing after 2.3×10^{-11} sec, although frequencies there obviously decrease at those late times.

This section examines measurement techniques in which extrema and inflection points replace zero crossings in (4). The techniques are examined carefully because they are used to get the paper's main result (Section 3), which is about a small effect. Our technique for measuring instantaneous frequency consists of two guidelines:

(a) *Infer frequencies from pairs of inflection points*

or pairs of extrema; do not mix types. (5)

(b) *Inflection points yield better accuracy.*

Use of technique (5), instead of the zero-crossing technique, could have improved measurements in Refs. 5 and 7.

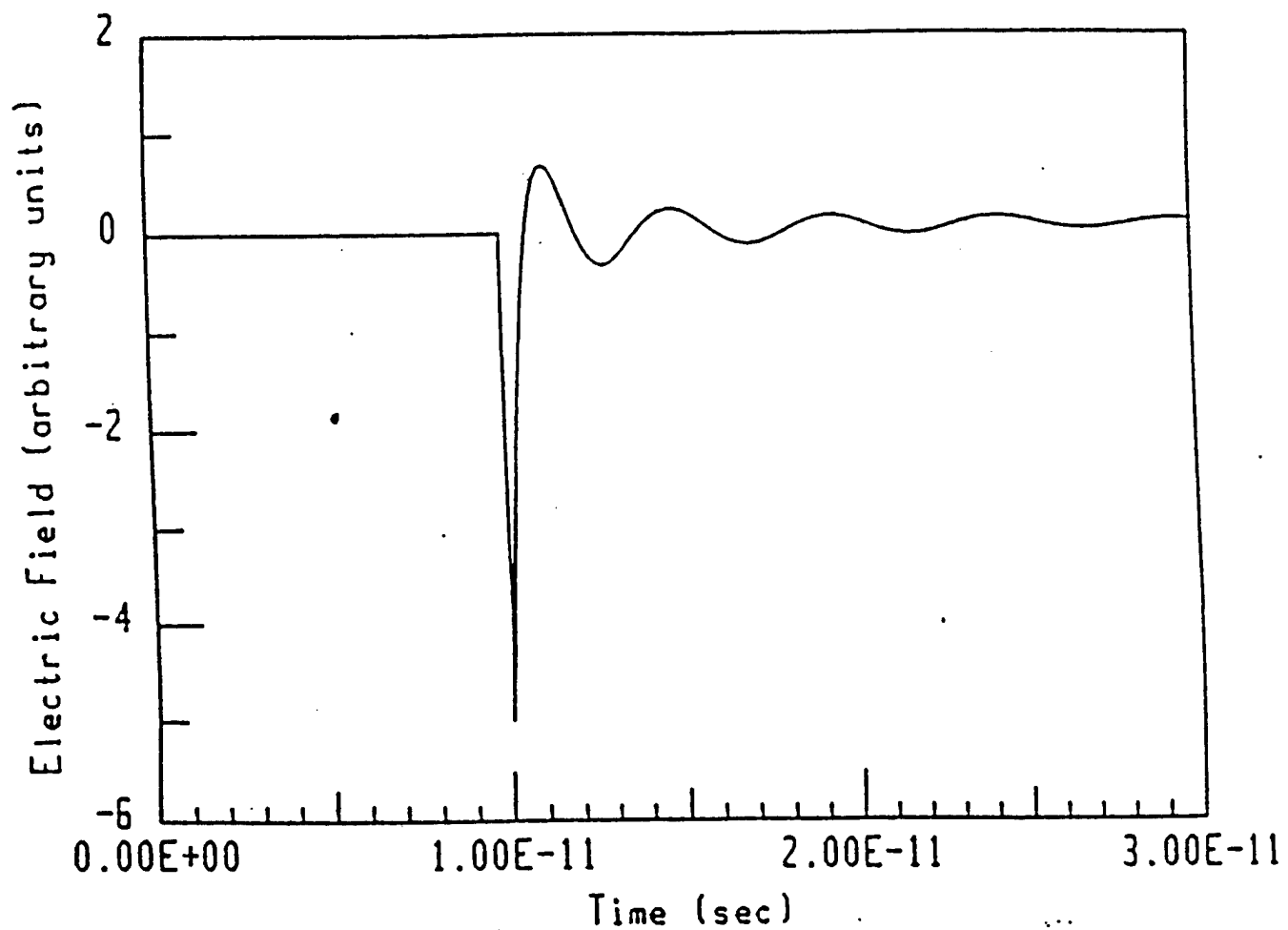


Fig. 3. Time trace of a transmitted field produced by a sharp incident pulse. The medium is undamped.

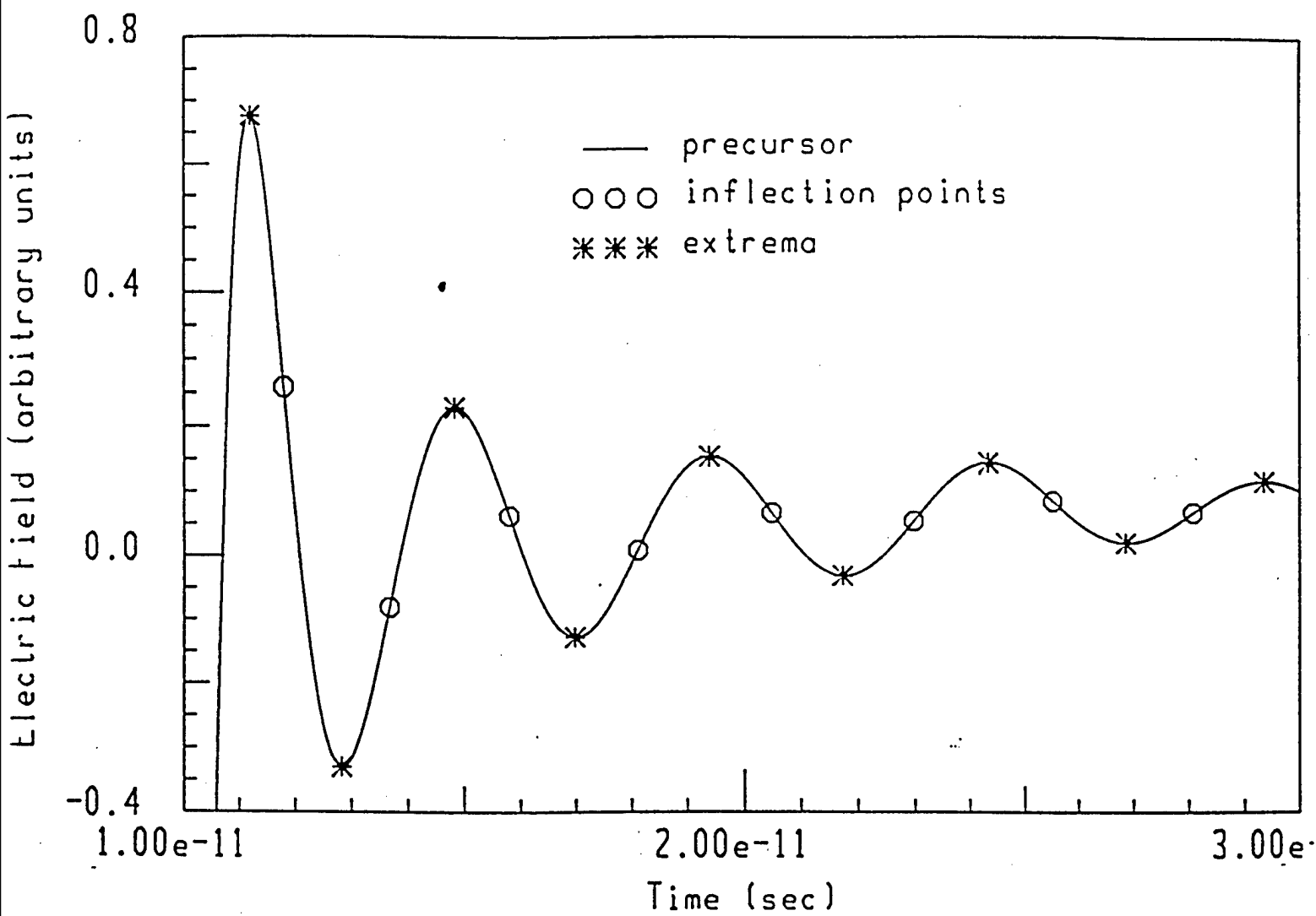


Fig. 4. Detail from Fig. 3.

This section tests candidate techniques on a simulated precursor. The simulation uses computer programs from Krueger and Winther (personal communication) that are described in Appendix A. The simulation is for a 3-mm-thick homogeneous slab of Lorentz medium (1) that has plasma frequency $\omega_p = 10^{12}$ /sec, resonant frequency $\omega_r = 5 \times 10^{11}$ /sec, and damping $\delta = 0$. Outside the slab is free space with unit permittivity. The incident field is specified just inside the slab's left wall, and the response is computed just inside the slab's right wall.

An incident delta pulse produces a transmitted field that is a delta function plus a remainder, which is called a precursor. The precursor is illustrated in Fig. 3 and is defined analytically in the paragraph after (A6). We use inflection points and relative extrema, but not the absolute extremum, to measure instantaneous frequency in three ways. Figure 4 focuses on the useful part of Fig. 3; its circles mark inflection points and its asterisks mark extrema. Inflection points in Fig. 4 do not follow the slow, upward rise expected of a low-frequency component; yet we will see that inflection points give the best reconstructions.

Figure 5 illustrates the slowness (c/v) measured from Fig. 4 using three techniques. Circles in Fig. 5 come from substituting consecutive inflection points for consecutive zero crossings in (4); the asterisks come from consecutive extrema; and diamonds come from pairs consisting of an inflection point and an adjacent extremum. The curve is the group-velocity prediction (c/v_g) for the medium, which is undamped. Figure 5 is numerical evidence that the inflection-point technique (circles) is the most accurate of the three considered. We will now explain this numerical evidence.

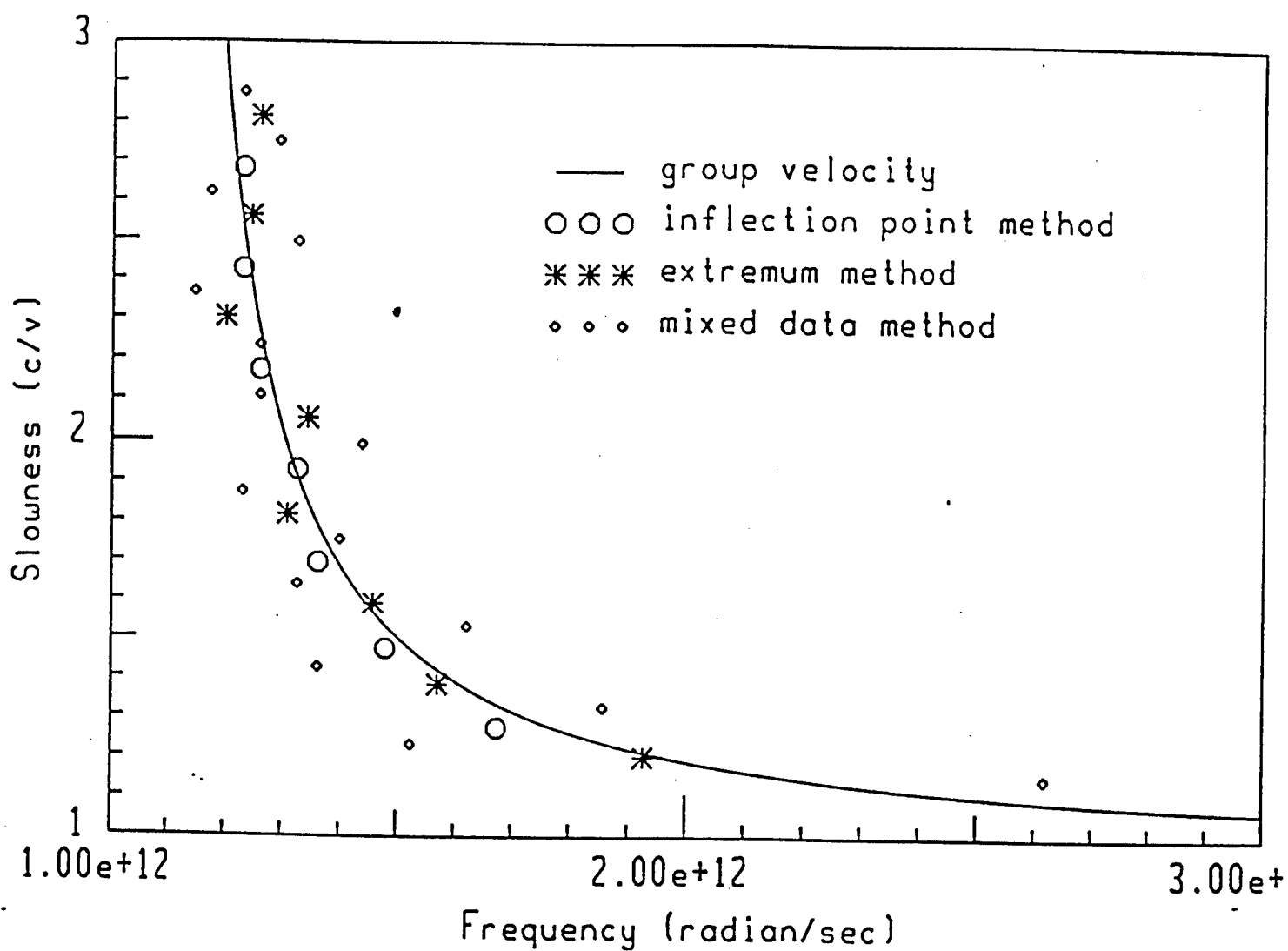


Fig. 5. Slowness, as inferred from Fig. 4 by three different methods. The curve is c/v_g . The medium is undamped.

The signal in Fig. 4 has a high-frequency oscillation and a low-frequency, upward drift. A low-frequency drift whose effect is constant between two extrema should cause little error in measuring ω_{inst} because extrema are zeros of the first derivative, and the derivative of a constant is zero. The error should be larger for a drift that is linear but non-constant between extrema, though such a linear drift between inflection points (zeros of the second derivative) produces little error. Thus, frequency measurements based on inflection points should be more accurate than measurements based on extrema, and far more accurate than zero-crossing measurements. Further, systematic errors from extrema and from inflection points should differ. The source of those differing systematic errors may be seen in Fig. 4, in which each inflection point is closer to the extremum on its immediate left than to its other neighbor. However, some of that shift is expected because wavelengths increase with time.

Instantaneous frequency is the reciprocal of a difference (4). Therefore, the effect of differing systematic errors is reduced considerably by pairing inflection points with other inflection points, and extrema with extrema. These last three paragraphs are summarized in (5).

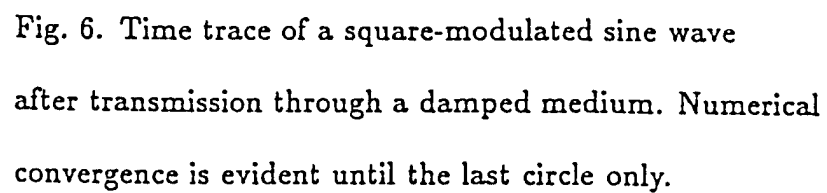
3. WAVE SPEED

This section examines three precursors in damped media. The precursors' wave speeds are measured in accordance with the guidelines in (5). This section's last three paragraphs describe the paper's main results.

Figure 6 shows a precursor computed, by the method in Appendix A, for a half-space of Lorentz medium that has plasma frequency $\omega_p = 10^{12}/\text{sec}$, resonant frequency $\omega_r = 5 \times 10^{11}/\text{sec}$, and damping $\delta = 2 \times 10^{11}/\text{sec}$. The natural frequency $\nu = \sqrt{\omega_r^2 - \delta^2}$ differs from the resonant frequency by 8%. The incident field is a square-modulated sine wave that, just inside the material, has amplitude 10, has carrier frequency $\omega_c = 9 \times 10^{11}/\text{sec}$, consists of ten periods, and is directed into the medium. The field is computed for a depth 3 mm inside the medium. In the simulation, each 3-mm spatial interval is represented by 700 points and each 6-mm/c time interval is also represented by 700 points, defining a space-time grid.* The simulation was compared with one for which each 3-mm-by-6-mm/c patch is represented by a 450-by-450-point grid. The simulations agree until $1.6 \times 10^{-11}\text{sec}$ but disagree thereafter, owing to accumulated discretization errors. In particular, the extrema and inflection points marked in Fig. 6 occur at the same times in the two simulations, to within the resolution of the coarser (450 by 450) grid. All other simulations in this section passed similar convergence tests.

Extrema in Fig. 6 are marked by asterisks and inflection points by circles. Instantaneous frequency [(4) and (5)] and arrival time are inferred from pairs of inflection points and from extrema. Each frequency component is assigned a speed $v = 3 \text{ mm}/T_a$, where T_a is arrival time at the 3-mm depth. The slowness c/v of each component is compared in Fig. 7 with three slownesses c/v_e , which correspond to energy velocity (3) for media that have zero damping (solid curve),

*Even though $\Delta t = 2\Delta x/c$, the simulation's evenly-staggered grid $g_{ij} = (i\Delta x, (i+2j)\Delta x/c)$ has slope c between adjacent points, as can be shown by graphing the points.



the correct damping ($\delta = 2 \times 10^{11}/\text{sec}$, dashed curve), and critical damping ($\delta = \omega_r = 5 \times 10^{11}/\text{sec}$, dash-dotted curve). Data from inflection points are plotted as circles and those from extrema as asterisks. The effect of discretization error is illustrated in Fig. 7 wherever an error bar exceeds a point marker's width. The smallest un-illustrated error bar is half the width of a marker. Vertical error bars are minute. Appendix B defines the error bars and Appendix C has further error analysis.

The most error-prone points in Fig. 7 are not useful for distinguishing among energy velocities. Figure 8 focuses on the useful data. The slowness inferred from inflection points (circles) is consistent with energy velocity for damping $2 \times 10^{11}/\text{sec}$ and is less consistent with zero damping. Slowness inferred from extrema (asterisks) is less conclusive; however, we showed in Section 2 that data from extrema are less accurate than those from inflection points.

We computed a second precursor for the medium that underlies Figs. 6–8. This time the incident pulse is a delta function. (The paragraph after (A6) discusses delta functions.) The response 3 mm inside the dispersive half-space is a delta function plus the remainder illustrated, in part, in Fig. 9. The positions of extrema and inflection points change negligibly when the number of grid points is reduced by 60%, implying numerical convergence throughout Fig. 9. The simulation's absolute minimum (-50 units, which is attained at 10^{-11}sec) is not graphed because it is not used to compute wave speed.

Slowness for Fig. 9 is computed with inflection points and extrema. The result is Fig. 10, in which circles represent data from inflection points, asterisks represent extrema, and curves represent energy velocity for the same damping

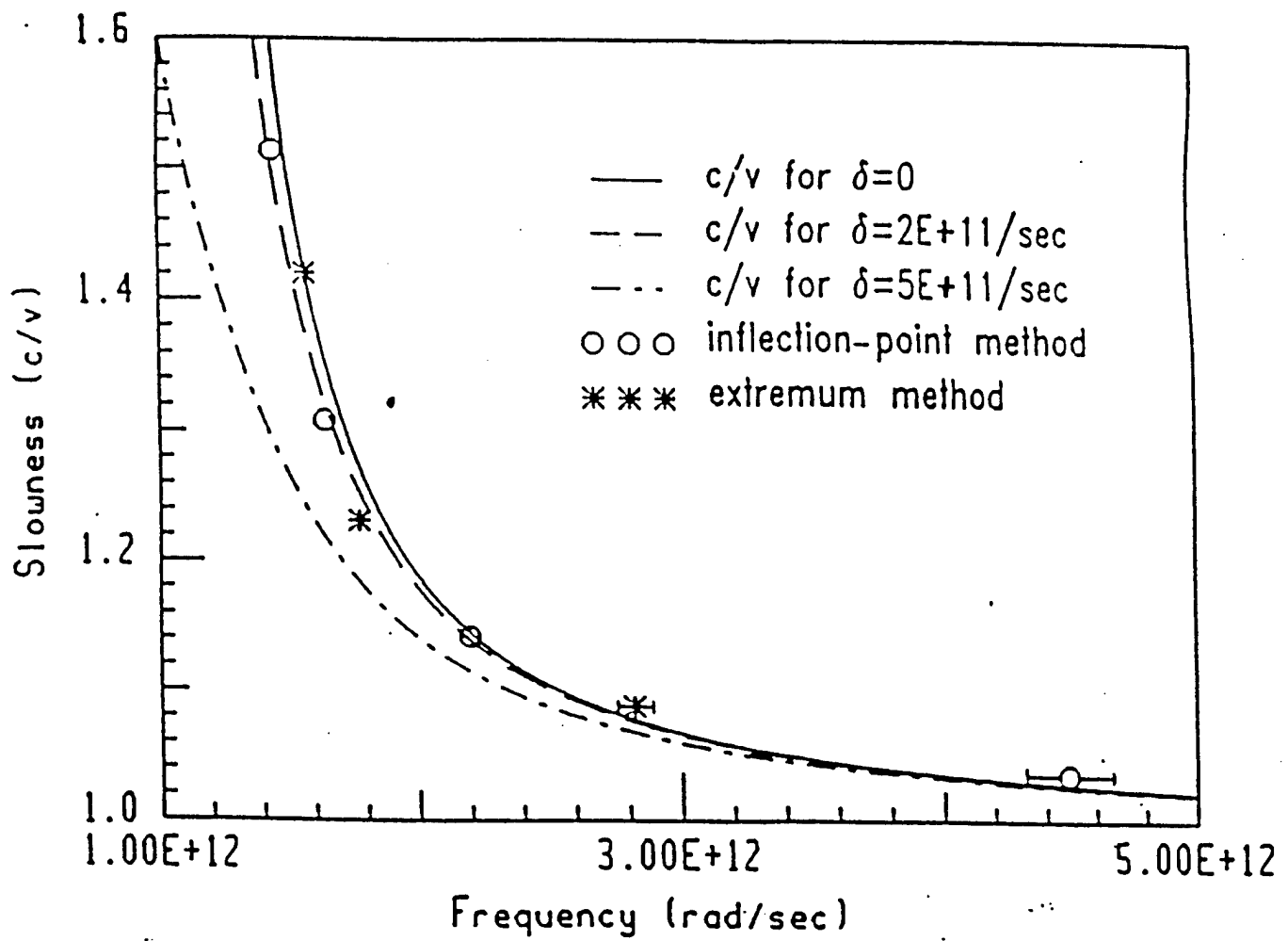


Fig. 7. Slowness, as inferred from Fig. 6, for which $\delta = 2 \times 10^{11}/\text{sec}$. Measurements are consistent to varying degrees with c/v_e curves for the underlying medium (dashed), and for undamped (solid) and critically damped (dash-dotted) media.

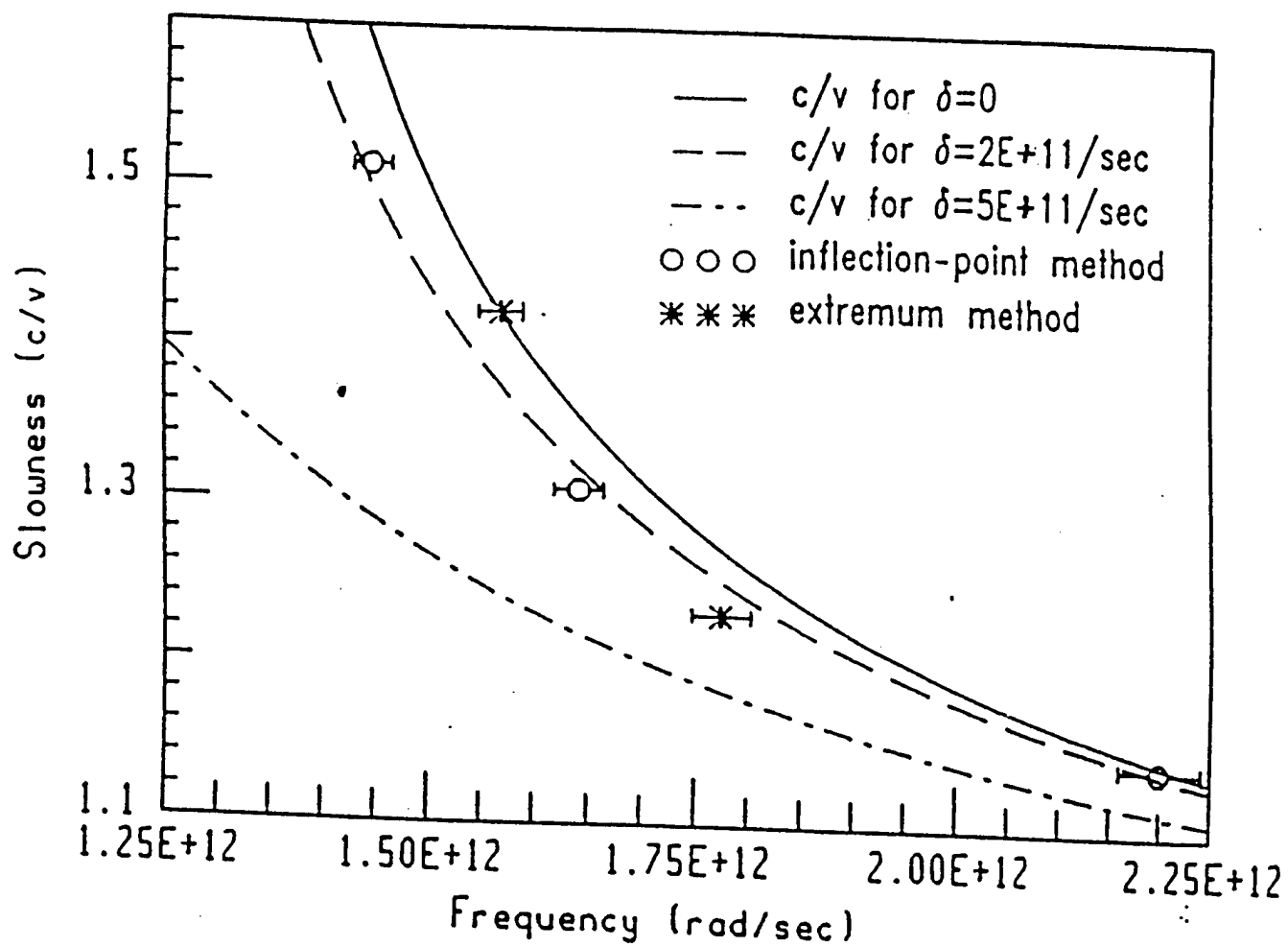


Fig. 8. Detail from Fig. 7.

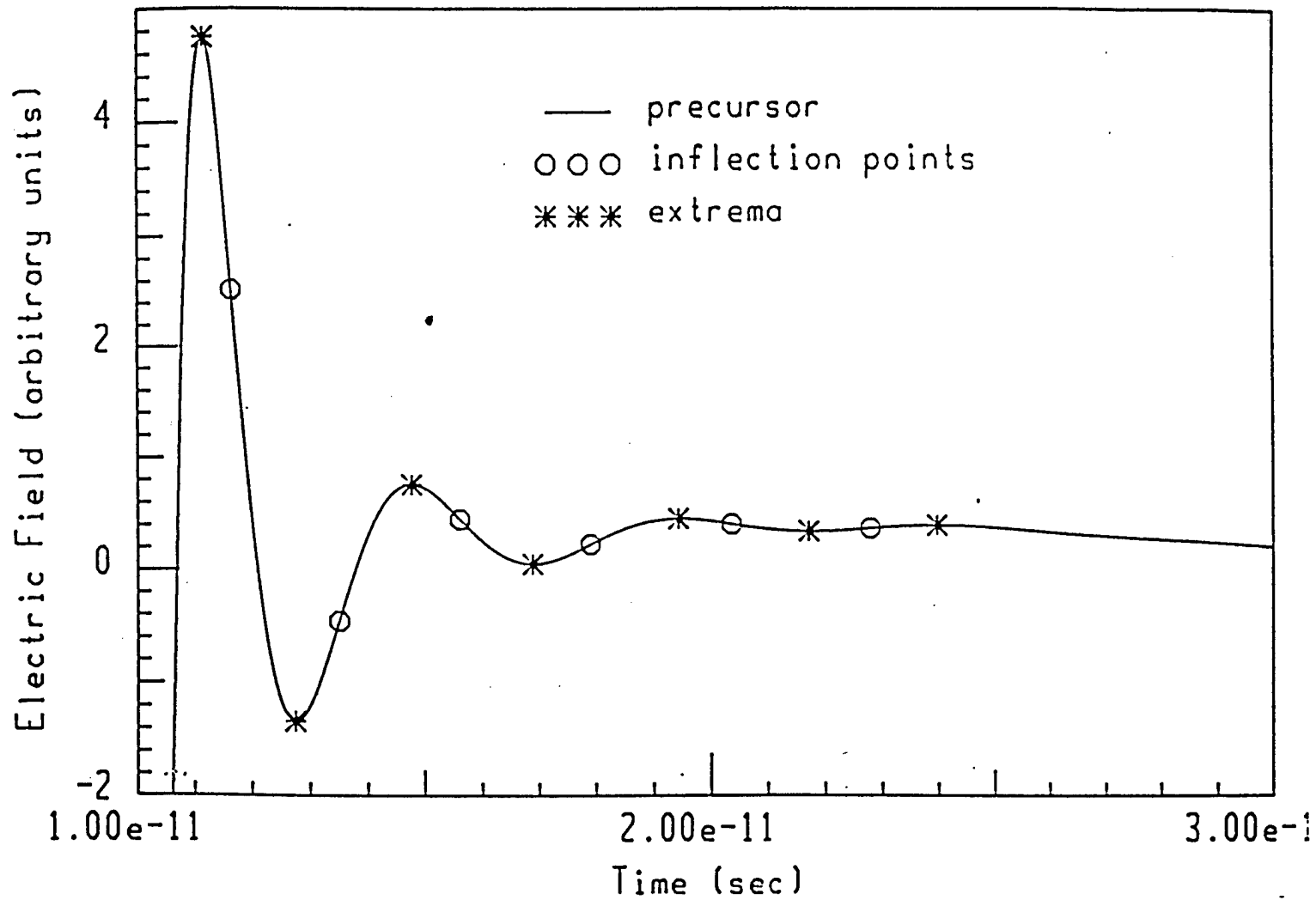


Fig. 9. Part of the time trace of a sharp pulse after transmission through a medium with $\delta = 2 \times 10^{11}/\text{sec}$.

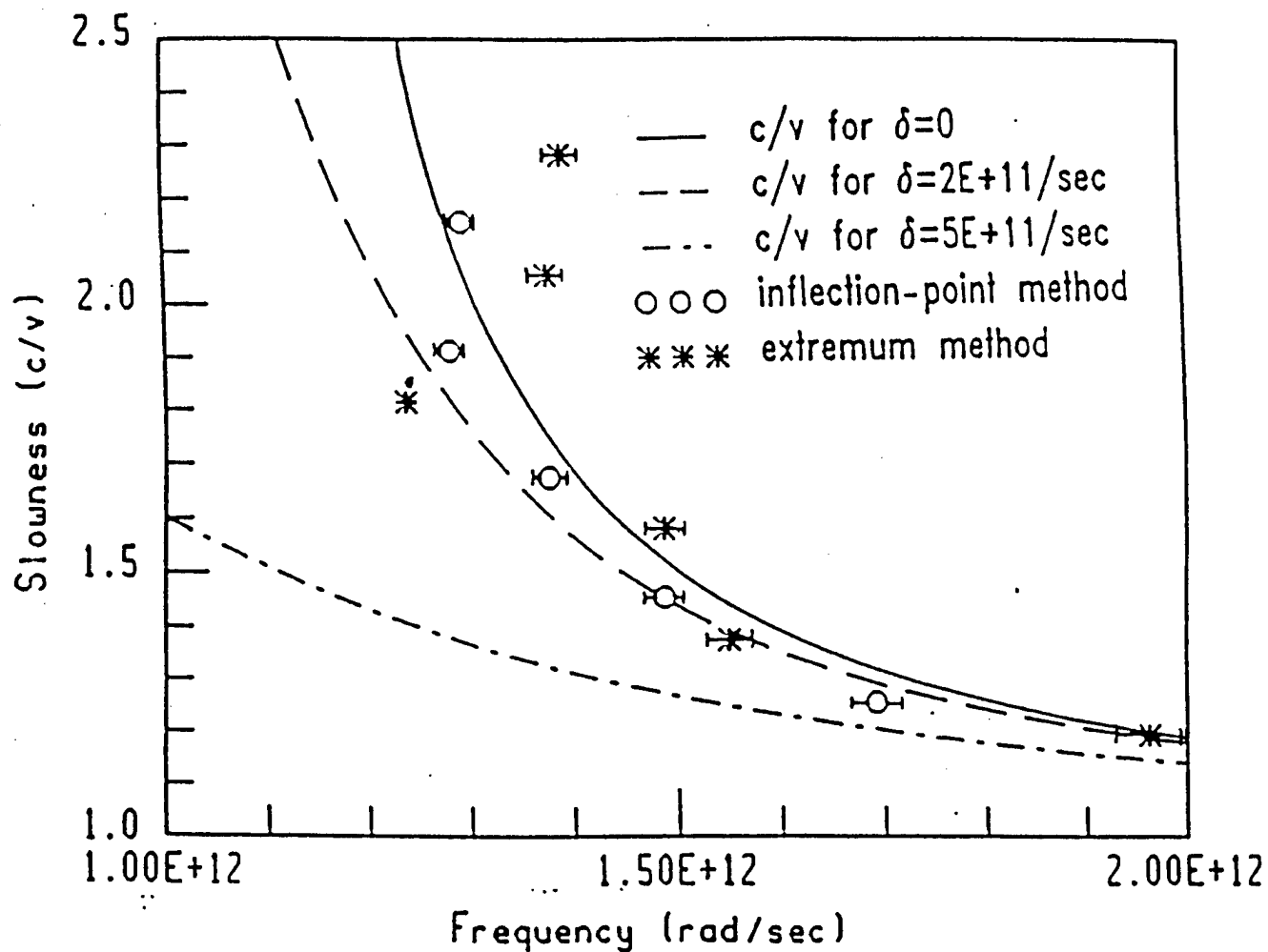


Fig. 10. Slowness, as inferred from Fig. 9, for which $\delta = 2 \times 10^{11}/\text{sec}$. Measurements are consistent to varying degrees with c/v_e curves for three different media.

constants as in Figs. 7 and 8. All figures omit error bars that are narrower than point markers.

In Fig. 10, inflection-point data (circles) are consistent with energy velocity for 2×10^{11} /sec damping, except possibly for the slowest component, which comes from oscillations in Fig. 9 that have the smallest amplitudes. Data from extrema, which are less accurate than data from inflection points, zigzag across Fig. 10. Zigzags are most likely caused by inaccuracy of the extremum technique (5). (The scattered asterisks would otherwise imply nonphysically that some frequency components arrive twice. For example, the component $\omega = 1.3 \times 10^{12}$ /sec would have speeds $v = c/1.75$ and $v = c/1.9$.) Conversely, the smoothness of inflection-point data, with a single exception owing to oscillations of small amplitude, is further evidence of those data's reliability.

The last simulation uses the same plasma frequency ω_p and resonant frequency ω_r as before. The damping δ is increased to 3×10^{11} /sec, so the natural frequency ν differs from the resonant frequency ω_r by 20%. The incident pulse is a delta function and the response 3 mm inside the dispersive half-space is a delta function plus the remainder in Fig. 11. There is numerical convergence throughout the simulation. Slowness is illustrated in Fig. 12, in which the dotted curve represents energy velocity for 3×10^{11} /sec damping and other notation is as in previous figures.

We have now compared wave speeds of three precursors with predictions from energy velocity (dashed and dotted curves) and group velocity (solid curves). No single data set is dramatically more consistent with v_e (with damping) than with v_g (no damping.) However, the evidence—Figs. 8, 10, and 12—is more conclusive

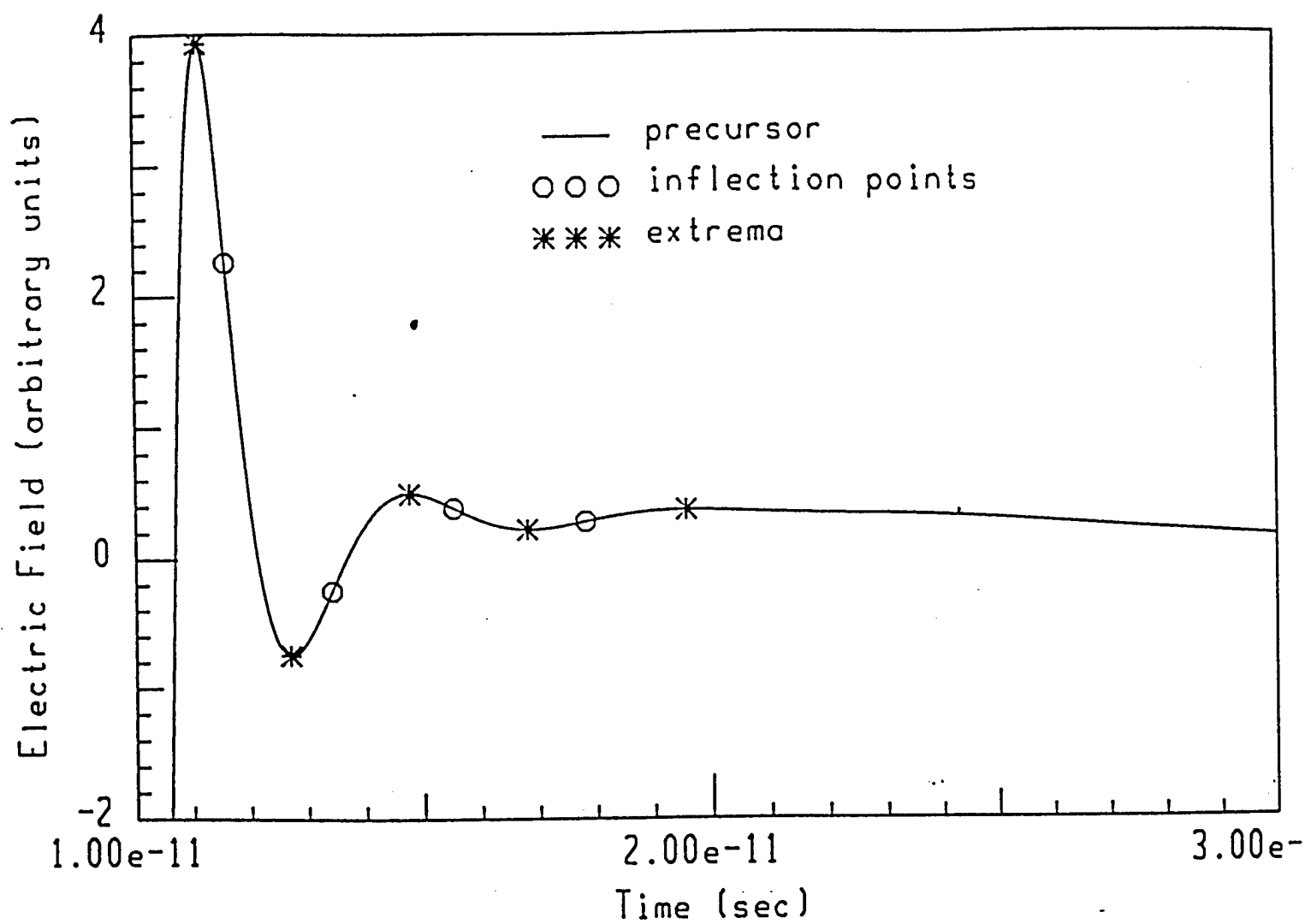


Fig. 11. Part of the time trace of a sharp pulse after transmission through a medium with $\delta = 3 \times 10^{11}/\text{sec}$.

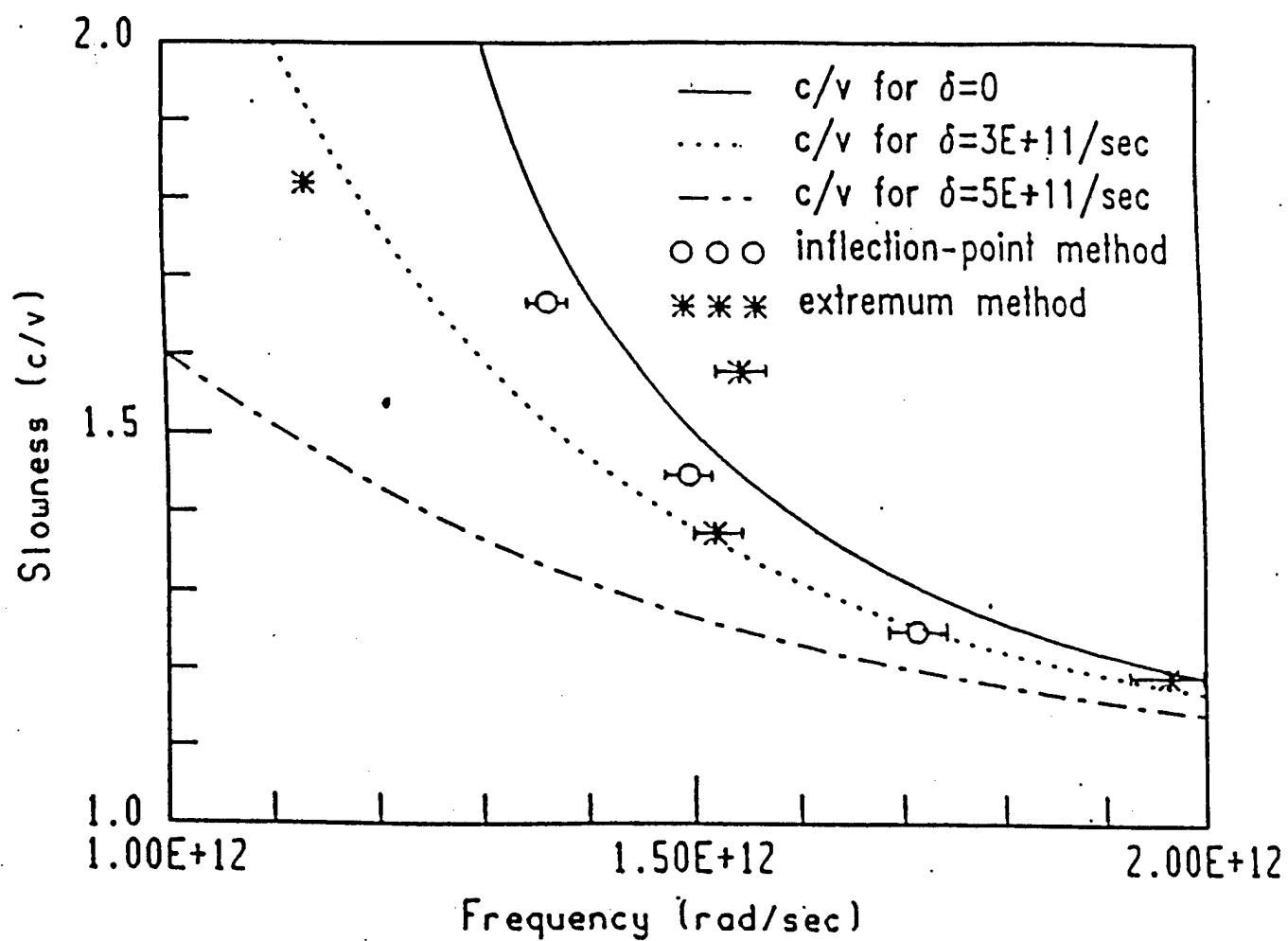


Fig. 12. Slowness, as inferred from Fig. 11, for which $\delta = 3 \times 10^{11}/\text{sec}$. Measurements are consistent to varying degrees with c/v_e curves for three different media.

if viewed all together, and is strengthened by properly weighting the data from inflection points (circles) and extrema (asterisks). In particular, we showed in Section 2 that asterisk data should have greater error than circle data: a conclusion supported further by the zigzagging of asterisks across Figs. 10 and 12. Therefore, asterisk data should have less weight than circle data. With that understanding, the data are conclusive.

There is convincing evidence, in the case $\omega_p = 10^{12}/\text{sec}$ and $\omega_r = 5 \times 10^{11}/\text{sec}$, that damping speeds-up frequency components noticeably, to a degree that is consistent with energy velocity. The effect is too subtle, or our measurements too crude, to resolve $2 \times 10^{11}/\text{sec}$ damping from $3 \times 10^{11}/\text{sec}$ damping, though the data are clearly inconsistent with critical damping $5 \times 10^{11}/\text{sec}$. That is, the data are in rough agreement with energy velocity, but not in fine agreement.

The numerical data have three sources of error: discretization error in computing precursors, discretization error in measuring instantaneous frequency (4), and crudeness of the inflection-point technique (5). The first two sources of error are analyzed in Appendix B, and are represented quantitatively by error bars in several figures. Appendix C estimates the error caused by the inflection-point technique (5), with the result that this section's conclusions are unaltered.

4. DEBYE MEDIA

Albanese, Penn, and Medina⁹ computed precursors for water. Their model is a conducting Debye medium

$$\sigma = \text{constant} \quad \epsilon(\omega) = \epsilon_1 + \frac{a}{1 + i\omega T} \quad (6)$$

for frequencies from zero to 100 GHz. (Reference 9 uses $\epsilon_1 = 5.5\epsilon_0$, $a = 72.7$, $T = 8.1 \times 10^{-12}$ sec, and $\sigma = 10^{-5}$.) Electrical properties at frequencies above 100 GHz are modeled differently. However, the incident field is a square-modulated 1-GHz sine wave of ten periods' duration; thus, the precursor is determined almost entirely by the Debye model (6). One of the precursor's most striking features is that it has few oscillations, which imply that wave speeds can be measured for only a few frequency components, and those speeds are approximately equal. That is, the damping constant T only slightly affects the speed of frequency components that are observable and measurable in that simulation. Similar effects—which are also slight—are seen in Section 3 and Ref. 5.

The earlier characterization of T as a damping constant should be explained. The damping constant δ of the Lorentz model (2) is aptly named because of its role in the model equation $\ddot{x} + 2\delta\dot{x} + \omega_f^2 x = \text{constant} \times e^{i\omega t}$. It is sensible to call T a damping constant for the Debye model because the permittivity (6) is a small- ω approximation¹³ to the Lorentz model (2), with damping $T = 2\delta$. Although Lorentz and Debye models have easily-identified damping constants, it may not be possible to extend the idea of a damping constant to all dispersive media. However, there is evidence from three independent sources—Section 3 and Refs. 5 and 9—that damping affects speed slightly or negligibly for oscillator-type models.

5. COMPARISONS OF GROUP AND ENERGY VELOCITY

A. Open Questions

Energy velocity is a generalization of group velocity,³ and in that sense v_e is better than v_g . That is, v_e is better in theory. But how much better is v_e empirically? In particular, how much better does v_e predict the speeds of frequency components that can be observed and measured?

B. Empirical Similarities

We explained after (3) how v_g and v_e predict equally well the speeds of frequency components observed and measured in Ref. 5. That may seem puzzling at first, because v_g is complex-valued in the stop bands^{3,11} of undamped Lorentz media, and it is also complex-valued for damped media. This subsection discusses stop bands at length, and then explains how v_g and v_e can sometimes be equally useful when there is damping.

Energy velocity (3) predicts the speed of all frequency components, including those in stop bands, but v_g cannot predict speeds in the stop bands^{3,11} ($\omega_r, \sqrt{\omega_r^2 + \omega_p^2}$) of undamped Lorentz media $(\omega_p, \omega_r, 0)$ because v_g is purely imaginary there.¹¹ We will show, however, that there has been no reliable frequency measurement in a stop band; consequently, the uselessness of v_g in stop bands has no proven empirical consequence.

It appears that the only papers that measure instantaneous frequency for Lorentz media are the present one, and Refs. 5 and 7. Figure 6 of Ref. 5 shows that the precursor there has no observable and measurable component in the

stop band ($4 \times 10^{16}/\text{sec}$, $6 \times 10^{16}/\text{sec}$). Components in the stop band also aren't observed here. Thus, only one set of stop-band measurements has ever been reported. Those measurements are in Figs. 8, 10, 12, and 14 of Ref. 7 (called [7, Figs.]), for which the stop band is also ($4 \times 10^{16}/\text{sec}$, $6 \times 10^{16}/\text{sec}$): The subject of that paper (signal velocity) and this one (v_g and v_e) differ. However, the parts of [7, Figs.] to the left of the intervals identified there with the mark " θ_c ," may be relevant here. That is because the left-of- θ_c parts are said, in text that follows equation (2.12) of Ref. 7, to be dominated by precursors. Yet we will see that the left-of- θ_c stop-band measurements of [7, Figs.] are not accurate enough for our purpose because the measured speeds are multiple-valued functions of frequency, and because of other matters relating to energy velocity. This is explained in the next two paragraphs.

Energy velocity (3) is a single-valued function of frequency. That is why Section 3 says that the zigzagging asterisks in our Fig. 10 represent measurements that are too inaccurate to be useful here. For example, if the asterisk measurements in Fig. 10 were reliable (they aren't, which is why we developed (5)), then the component $\omega = 1.3 \times 10^{12}/\text{sec}$ would have speeds $v = c/1.75$ and $v = c/1.9$. In another example, the different degrees of zigzagging in three data sets in the present paper's Fig. 5 make the relation of multiple-valued speeds and inaccuracy even more clear, especially in light of the text in Section 2. Figure 5 suggests further that the bandwidth of zigzags is comparable to the error in measuring instantaneous frequency. Thus, the degree of zigzagging in [7, Figs.] suggests that the figures' left-of- θ_c parts have data in the stop band merely because of inaccurate frequency measurements. Such a result is unsurprising because simple

differentiation (see the sixth paragraph of Section 2) shows that the zero-crossing technique of Ref. 7 is especially apt to be inaccurate when frequency components interfere, as they do in the simulations underlying [7, Figs.] That interference, and other sources of measurement error, are discussed in Ref. 7 on pages 1438 and 1439.

We have just seen that the left-of- θ_c stop-band measurements in [7, Figs.] are inconsistent with the energy-velocity prediction that speed is single-valued, but those measurements are inconsistent with v_e in other ways. For example, energy velocity (3) predicts for the medium of Ref. 7 that frequency components in its stop band (4×10^{16} /sec, 6×10^{16} /sec) travel no faster than one-eighth the speed of light in vacuum, but [7, Figs.] are all inconsistent with that prediction. To make a more thorough comparison with v_e , one can plot (3) directly on [7, Figs.] and then observe that every left-of- θ_c stop-band component travels faster than v_e allows.

We conclude that the relevant stop-band measurements in [7, Figs.] are too inaccurate for our purpose* because the corresponding speeds are multiple-valued, and all of those values are too high. The only other papers that measure instantaneous frequency appear to be the present one and Ref. 5, but neither has stop-band measurements. Therefore, the inability of v_g to make stop-band predictions has no proven empirical consequence.

* More precisely, no left-of- θ_c measurement in Ref. 7 is accurate enough that it can be relied on to be in a stop band. The measurements may still be useful in the context of Ref. 7, which emphasizes signal velocity.

In a final matter concerning Ref. 7, we want to make it quite clear that the paper's time traces are not in question. The time traces are unquestioned because the paper's departures from the predictions of energy velocity are most likely caused by inaccurate frequency measurements. Some inaccuracies are discussed in Ref. 7 on pages 1438 and 1439, and others are caused by the zero-crossing technique's special sensitivity to interference. Although better frequency-measurement techniques are now available in (5), Appendix B shows that the error in measuring frequency still predominates: Frequency measurements are delicate.

Let us now consider damped Lorentz media, for which group velocity is complex-valued. A complex-valued v_g seems useless; but if the damping δ affects the speed of observable frequency components negligibly, then v_e for $\langle \omega_p, \omega_r, \delta \rangle$ and v_g for the related undamped medium $\langle \omega_p, \omega_r, 0 \rangle$ differ negligibly in their predictions. That is exactly the case for the medium studied in Ref. 5; thus, as is explained after (3), v_g and v_e are equally useful there. In a related matter, Section 4 finds further evidence that damping attenuates the components it speeds up, making them difficult to observe. Those competing effects of speed-up and attenuation explain how v_e for a damped medium and v_g for a related undamped medium can predict equally well the speeds of observable frequency components.

C. Empirical Differences

The present paper appears to have the only empirical evidence that v_e is better than v_g . In particular, Section 3 identifies media for which v_e is noticeably better than v_g , though the difference is slight. Efforts to find Lorentz media in which v_e is far superior to v_g were unsuccessful, but not all Lorentz media were examined.

In spite of numerical evidence from several sources, it is still unknown whether energy velocity is any more than slightly better than group velocity from an empirical point of view. That uncertainty is striking, considering that many papers mention energy velocity.

6. ELEMENTARY INVERSION

This section makes an observation, apparently unnoticed since precursors were first

predicted¹⁴⁻¹⁶ in 1914, that wave speed determines permittivity elementarily.

Limitations of this elementary inversion are discussed. The conclusion is in the first two paragraphs after (8).

It is easy to measure group velocity for undamped media. Substitution of $v_g = d\omega/dk$ into (7) verifies that permittivity can then be computed from v_g as

$$\epsilon(\omega) = \omega^{-2} \left[\omega_0 n(\omega_0) + c \int_{\omega_0}^{\omega} \frac{d\omega'}{v_g(\omega')} \right]^2 \quad (7)$$

where $n(\omega_0)$ is the index of refraction at a starting frequency ω_0 . If group velocity is measured for high frequencies, as has been done here and in Ref. 5, then one could choose ω_0 to be the highest such frequency and assume $n(\omega_0) \approx 1$. After all,¹¹ $n(\omega) \rightarrow 1$ as $\omega \rightarrow \infty$. Thus, it is easy to measure the high-frequency part of permittivity for *undamped* media. The same measurement appears to determine with fair accuracy all but the damping constant for *damped* Lorentz media. The next two paragraphs examine difficulties faced by elementary inversion for an

isolated interval of frequencies that are too low for the approximation $n(\omega_0) \approx 1$ to be valid.

Identifying a starting point $\langle \omega_0, n(\omega_0) \rangle$ in an isolated band of low frequencies is problematic, especially because laboratory apparatus that produce precursors may not be suited for measuring an index of refraction. In some applications, however, one may have prior knowledge of starting-point data to within reasonable error. For high-frequency starting points, the error is small and the reconstruction good. For low-frequency starting points, starting-point error is likely the predominant error. This predominant error causes the mathematical difficulty that is considered next.

Assume in this paragraph that ϵ is causal, that group velocity v_g is known accurately for every frequency in an interval $[a, b]$, and that n is known for no point in $[a, b]$. Set ϵ_α to be the right side of (7) after the undetermined product $\omega_0 n(\omega_0)$ is replaced with an arbitrary parameter α :

$$\epsilon_\alpha(\omega) := \omega^{-2} \left[\alpha + c \int_{\omega_0}^{\omega} \frac{d\omega'}{v_g(\omega')} \right]^2. \quad (8)$$

A causal permittivity, such as ϵ , can't have a second-order pole at¹¹ $\omega = 0$. This section's last paragraph proves that ϵ_α has a second-order pole at $\omega = 0$ unless $\alpha = \omega_0 n(\omega_0)$. Thus, there is a unique causal ϵ_α , which is ϵ . In inverse scattering, uniqueness is often helpful, but not so here: Anything but the precisely correct—hence unlikely—choice of α yields noncausal, nonphysical permittivity. Thus, elementary inversion for an isolated band of low frequencies has a predominant error that ruins causality.

We conclude that elementary inversion (7) can safely be used for data covering an interval that includes high frequencies. Inversion then is valid throughout the interval, even if the interval also includes low frequencies. Elementary inversion may not be useful for isolated bands of low frequencies.

Time-domain experiments¹⁷⁻¹⁹ on dispersive materials were performed in the 1960s and 1970s and the data analyzed in the frequency domain with methods more complicated than (7). Time-domain experiments continue,²⁰ partly in response to new methods of data analysis²¹⁻²³ in the time domain. Elementary inversion (7) appears to be the simplest frequency-domain inversion available for time-domain data. Elementary inversion is useful to varying degrees in different media. It is useless for the Debye medium simulated in Ref. 9, useful for Lorentz media simulated in this paper, and more useful for the Lorentz medium simulated in Ref. 5. For example, permittivity can be computed by simply integrating, as in (7), the v_g measurements in Fig. 5 or the measurements in Fig. 6 of Ref. 5.

This paragraph proves a result used earlier in this section. We assume, for the reason given after (8), that neither ϵ nor ϵ_α has a pole of order two at $\omega = 0$; then we show $\alpha = \omega_0 n(\omega_0)$. Let $\Delta = \alpha - \omega_0 n(\omega_0)$. Then (8), $v_g = d\omega/dk$, $k = \omega n/c$, and $\epsilon = n^2$ imply $\epsilon_\alpha = \epsilon + A$, where the function $A = \Delta(\Delta + 2n\omega)\omega^{-2}$ also does not have a pole of order two at $\omega = 0$. The equation $A = \Delta(\Delta + 2n\omega)\omega^{-2}$ implies

$$\epsilon = n^2 = \frac{\Delta^2}{4\omega^2} - \frac{A}{2} + \frac{\omega^2 A^2}{4\Delta^2}. \quad (9)$$

Neither A nor ε has a pole of order two at $\omega = 0$. Thus, (9) implies $\Delta = 0$, finishing the proof.

7. CONCLUSION

Section 3 shows that damping can affect the speed of frequency components noticeably, though the effect is slight. The effect's small size is surprising because it implies that energy velocity is only slightly more accurate here than is group velocity. Section 5 notes that there are now four independent sources of evidence that damping's influence on wave speed is slight or negligible for some Lorentz and Debye media. One interpretation is that the effect is small because of two competing mechanisms. Specifically, damping attenuates severely the frequency components whose speeds are most changed.

One practical consequence of this work is that the elementary inversion technique in Section 5 may be useful for some damped media, as well as for undamped media. The technique uses wave speed measurements that include high-frequency data. Two numerical examples are mentioned between (8) and (9).

APPENDIX A: DIRECT-SCATTERING ALGORITHM

This paper's simulations all use computer programs from Krueger and Winther (personal communication). The algorithm that underlies the programs has not yet been published, although it was rederived in detail by one of us and is further validated in Ref. 24. The algorithm uses a wave-splitting technique to calculate time-domain Green's functions. (Wave splitting is described simply in Ref. 25.)

Similar time-domain Green's functions, which we call Krueger-Ochs Green's functions, have been used for isotropic²⁶ and anisotropic²⁷ nondispersive slabs that are continuously stratified, and for cylinders whose dispersion is of type²⁸ $D(r, t) = \epsilon(r)[E(r, t) + \int_0^\infty ds g(s)E(r, t - s)]$ where r is radial distance. These functions have also been used in transport theory.²⁹

In response to a referee's suggestion, we document the unpublished Krueger-Winther algorithm by describing a slight generalization. We state results only. Details are deferred to Ref. 24 and a possible future paper by Krueger and Winther.

We will solve Maxwell equations for pulses normally incident on a finitely thick, flat slab with properties¹¹ $\nabla \times E = -\mu_0 \partial_t H$, $\nabla \times H = J + \partial_t D$, $J(z, t) = \sigma(z)E(z, t)$, and

$$D(z, t) = \epsilon_0 \left[E(z, t) + \int_0^\infty ds g(s)E(z, t - s) \right] \quad (A1)$$

where μ_0 and ϵ_0 are constants and $g(t < 0) = E(z > 0, t < 0) = 0$. The slab's boundaries are $z = 0$ and $z = L$. Let $c = 1/\sqrt{\mu_0 \epsilon_0}$ and define dimensionless variables

$$x = z/L \quad \tau = ct/L \quad (A2)$$

in which the slab's boundaries are $x = 0$ and $x = 1$. The wave equation for the electric field is

$$[\partial_x^2 - \partial_\tau^2 + B(x)\partial_\tau] u(x, \tau) + \partial_\tau^2 \int_0^\tau ds \gamma(s)u(x, \tau - s) = 0 \quad (A3)$$

where $B(x) = -\mu_0 L c \sigma[z(x)] = -\mu_0 L c \sigma(Lx)$, $\gamma(\tau) = -L c^{-1} g[t(\tau)] = -L c^{-1} g(L c^{-1} \tau)$, and $u(x, \tau) = E[z(x), t(\tau)]$.

Define convenient basis functions

$$u^\pm(x, \tau) = \frac{1}{2} \left[u(x, \tau) \mp \int_0^\tau ds \partial_z u(x, s) \right]. \quad (A4)$$

The functions u^\pm are basis functions in the sense that $u = u^+ + u^-$. Outside the slab, where $B = \gamma = 0$, we have²⁵ $u^+ = u^+(z - ct)$ and $u^- = u^-(z + ct)$; thus, the time-domain boundary condition of *incidence* can be expressed conveniently in terms of u^+ and u^- . The wave equations for u^\pm are

$$\begin{aligned} 2(\partial_x + \partial_\tau)u^+ &= -2(\partial_x - \partial_\tau)u^- = B(x) [u^+(x, \tau) + u^-(x, \tau)] \\ &+ \partial_\tau \int_0^\tau ds \gamma(s) [u^+(x, \tau - s) + u^-(x, \tau - s)], \end{aligned} \quad (A5)$$

which are coupled integrodifferential equations. The last paragraph defines Krueger-Ochs Green's functions $G^\pm(x, \tau)$ and a function $a(x)$ such that

$$\begin{aligned} u^+(x, \tau) &= a(x)f(\tau - x) + \int_0^{\tau-x} ds f(s)G^+(x, \tau - s), \\ u^-(x, \tau) &= \int_0^{\tau-x} ds f(s)G^-(x, \tau - s) \end{aligned} \quad (A6)$$

solve (A5) subject to the boundary conditions $u^+(0, \tau) = f(\tau)$ and $u^\pm(x > 0, \tau < 0) = u^-(x > 1, \tau) = 0$, for which the incident field is f . Thus, computing G^\pm

solves the scattering problem. The logical flow of the solution is $\langle G^\pm, f \rangle \rightarrow u^\pm \rightarrow u = u^+ + u^- \rightarrow E(z, t) = u(z/L, ct/L)$.

Equation (A6) and the boundary condition $u^-(x > 1, \tau) = 0$ show that $u^+(1, \tau)$ is the transmitted field. For that reason, $G^+(1, \tau)$ is called the transmitted response to an incident delta function $f(s) = \delta(s)$, after an attenuated delta function $a(1)\delta(\tau - 1)$ is subtracted from the transmitted field in (A6). Also, the term $\int_0^{\tau-1} ds f(s) G^+(1, \tau - s)$ is called the precursor, for any incident field f for which the previous integral exists. The response G^+ and the precursor are computed without having to represent delta functions numerically. Indeed, delta functions are used here only in physical interpretations, not in derivations²⁶ or numerics.

Let

$$a(x) = \exp \left[\frac{1}{2} \int_0^x dx' B(x') \right]. \quad (A7)$$

Krueger-Ochs Green's functions G^\pm satisfy the coupled integrodifferential equations

$$\begin{aligned} 2(\partial_x + \partial_\tau)G^+(x, \tau) &= -2(\partial_x - \partial_\tau)G^-(x, \tau) \\ &= B(x) [G^+(x, \tau) + G^-(x, \tau)] + a(x)\partial_\tau \gamma(x, \tau - x) \\ &\quad + \int_0^{\tau-x} ds [\partial_s \gamma(x, s)] [G^+(x, \tau - s) + G^-(x, \tau - s)] \end{aligned} \quad (A8)$$

subject to boundary conditions

$$G^{\pm}(x, 0^+) = 0$$

$$G^{\pm}(x, \tau < x) = 0$$

$$G^+(x, x^+) = a(x) \int_0^x dx' B^2(x')/8 \tag{A9}$$

$$G^-(x, x^+) = a(x)B(x)/4$$

where x^+ stands for the limit $\tau \downarrow x$. The functions G^{\pm} are continuous except as described in (A9). The method of Ref. 30 can be used to prove that there is a unique pair of solutions G^{\pm} to (A8)-(A9). The integrodifferential equations are solved numerically with the method of characteristics. That method is applied to similar equations in Refs. 26 – 29.

APPENDIX B: ERROR BARS

This appendix is written mainly in terms of extrema. The results also apply to inflection points, because inflection points are extrema of a first derivative.

The error bars in Figs. 7, 8, 10, and 12 represent the roots-mean-square of random errors in ω_{inst} . There are two sources of random error. They are the inexact computation of time traces and an inexact method of identifying extrema. The next two paragraphs estimate the roots-mean-square of those two types of error. The root-mean-square (rms) of the superposition of the two errors is then calculated. That calculation determines the rms error of each extremum's time coordinate. Consecutive extrema T and t define an instantaneous frequency

$$\omega_{\text{inst}} := \pi/(T - t) \tag{B1}$$

and the errors in T and t thereby affect ω_{inst} . The rms of the resultant error in ω_{inst} is calculated in (B2), and is used to define error bars. In this paper, each pair of error bars represents a computed frequency ω_{inst} , plus-or-minus the rms error in ω_{inst} . Notice that the bars represent random errors, not systematic errors. Systematic errors are discussed in Section 2, where it is shown that the inflection-point technique has smaller systematic errors than the extremum technique. Appendix C shows that systematic errors insignificantly affect the agreement of inflection-point data and energy velocity.

Let us now estimate the random error caused by inexact computation of time traces. The estimate is based on convergence tests described in the second paragraph of Section 3. Recall that time traces are computed on two grids whose resolutions differ significantly, and the traces' extrema are found to coincide within the resolution of the coarser grid. That convergence test shows that the coarser computation attains what is commonly called convergence; thus, one expects the finer computation also to converge. Consequently, one expects the extrema of the finer computation and the extrema of a hypothetical, exactly-computed time trace to coincide within the grid spacing Δ of the finer grid. We therefore assume that errors in the time coordinates of the finer computation's extrema are distributed uniformly between $-\Delta$ and Δ . The corresponding distribution $P_1(\varepsilon)$ of errors ε is $1/(2\Delta)$ for $|\varepsilon| \leq \Delta$, and 0 otherwise; and the rms error $[\int_{-\Delta}^{\Delta} d\varepsilon P_1(\varepsilon) \varepsilon^2]^{1/2}$

is $\Delta/\sqrt{3}$. That is, the inexact computation of time traces causes errors in the time coordinates of extrema, and the rms of those errors is approximately $\Delta/\sqrt{3}$.

Let us now estimate the rms of the error in identifying extrema. This new error will be defined by describing the way extrema are identified in practice: A time trace is computed on a grid of time-resolution Δ , is subjected to convergence test, and is found to pass the test. The trace represents an electric field $E_\Delta(i\Delta)$ at times $i\Delta$, for various consecutive integers i . Each relative extremum $i_0\Delta$ is found to be sharp in the sense that, first, $|E_\Delta(i_0\Delta)| > \max\{|E_\Delta([i_0-1]\Delta)|, |E_\Delta([i_0+1]\Delta)|\}$, and, second, the numerically-computed time trace has only one relative extremum at each broad peak in Fig. 6, 9, or 11. The sharp extremum is then said to occur at time $i_0\Delta$. Figure 13 shows that error can result even if the resolution- Δ computation is exact. For that reason, we assume that the error illustrated in Fig. 13 is uncorrelated statistically with the error that is estimated in the previous paragraph. Because of the lack of correlation, it is not a restriction to assume, merely for this paragraph's error estimate and for calculations leading to (B2), that the resolution- Δ computation is exact: that is, to assume that each computed value $E_\Delta(i\Delta)$ equals the exact electric field $E(t)$ at $t = i\Delta$. Existence of $\partial_t E(t)$ —which follows from the constitutive relation (1) and the Maxwell equation for $\partial_t D$ —then implies that $E(t)$ is almost symmetric in a small neighborhood of any relative extremum T , as illustrated in Fig. 13. That symmetry helps determine the maximum possible difference between $i_0\Delta$ and T , given that $i_0\Delta$ is a sharp extremum. The maximum difference is illustrated in Fig. 13, in which $i_0\Delta$ is $T - \Delta/2$, minus an infinitesimal, and $E_\Delta(i_0\Delta)$ is infinitesimally larger than $E_\Delta([i_0+1]\Delta)$. In fact, $i_0\Delta$ is a sharp extremum if, and only if, it is in the interval $(T -$

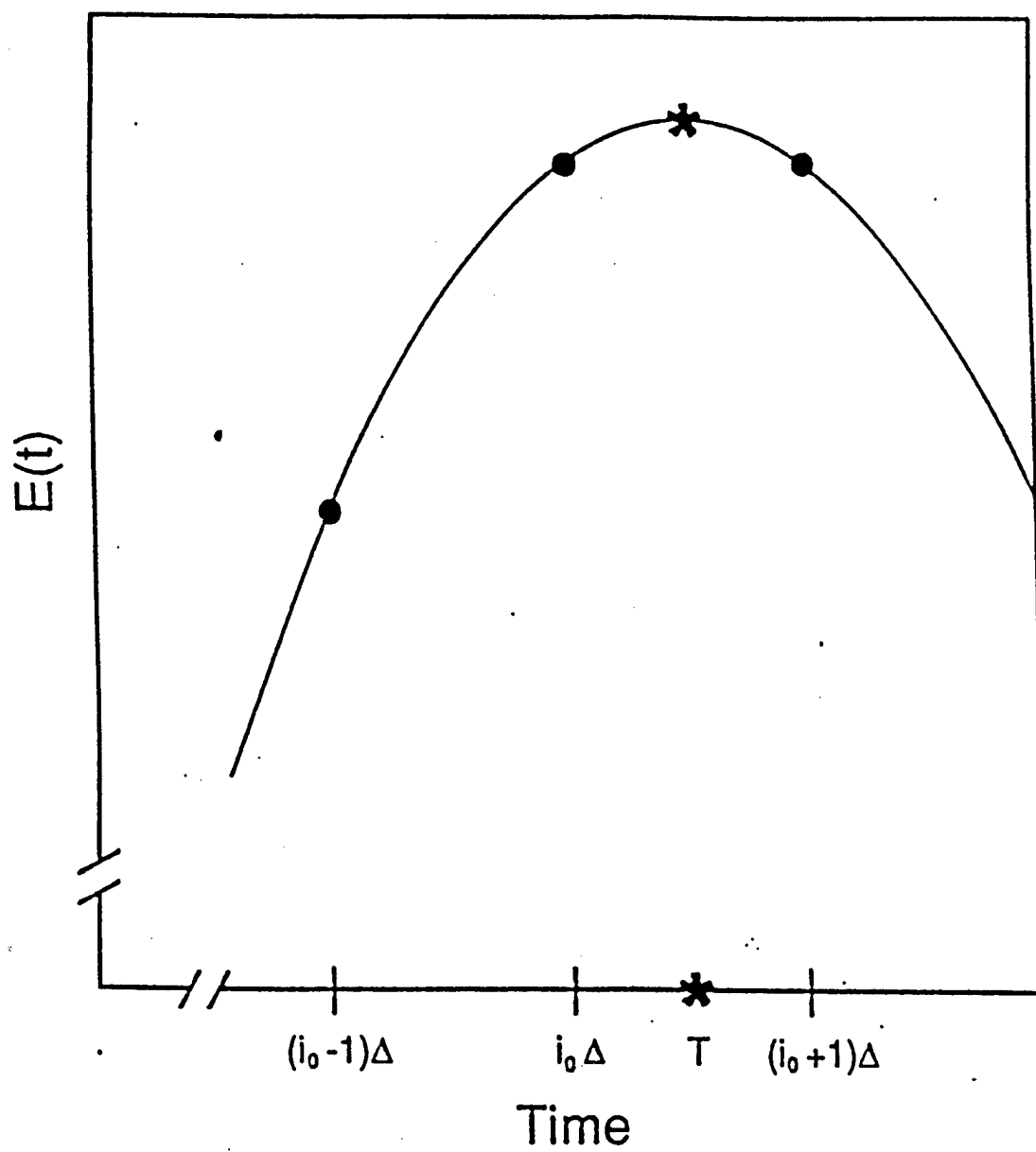


Fig. 13. Extrema (*) and grid points (•) are unlikely to coincide.

$\Delta/2, T + \Delta/2$). The corresponding distribution $P_2(\epsilon)$ of errors ϵ is, consequently, $1/\Delta$ for $|\epsilon| < \Delta/2$, and 0 otherwise; and the rms error $[\int_{-\Delta/2}^{\Delta/2} d\epsilon P_2(\epsilon) \epsilon^2]^{1/2}$ is $\Delta/\sqrt{12}$.

The roots-mean-square of two sources of random error have now been estimated. One rms error is $\Delta/\sqrt{3}$ and the other is $\Delta/\sqrt{12}$. The second estimate comes from a model in which the two sources of error are assumed, with justification, to be uncorrelated. Consequently, the rms of the total random error in the time coordinate of any extremum is $[(\Delta/\sqrt{3})^2 + (\Delta/\sqrt{12})^2]^{1/2} = \Delta\sqrt{5/12} \approx 2\Delta/3$.

The rms error that was just calculated affects the time coordinates T and t of consecutive extrema, which define the instantaneous frequency ω_{inst} in (B1). A relevant equation for the propagation of rms errors is known most widely in the context of Gaussian-distributed errors,³¹ but the equation also is valid for other distributions.³² That propagation-of-error equation implies

$$\|\epsilon_\omega\| = \left[\left(\|\epsilon_T\| \frac{\partial \omega_{\text{inst}}}{\partial T} \right)^2 + \left(\|\epsilon_t\| \frac{\partial \omega_{\text{inst}}}{\partial t} \right)^2 \right]^{1/2} \quad (\text{B2})$$

where $\|\epsilon_\omega\|$ is the rms error in ω_{inst} , $\|\epsilon_T\| = \|\epsilon_t\| = \Delta\sqrt{5/12}$ are the rms errors in T and t , and the partial derivatives in (B2) are calculated by differentiating (B1). In this paper, error bars span the frequency intervals $(\omega_{\text{inst}} - \|\epsilon_\omega\|, \omega_{\text{inst}} + \|\epsilon_\omega\|)$.

The analysis in the previous paragraph can be adapted, with changes, to the vertical coordinates $c/v = c(T + t)/(2 \cdot \text{depth})$ of Figs. 7, 8, 10, and 12. The adapted analysis shows that vertical error bars are much smaller than the height of the figures' point markers. Thus, the time traces in Figs. 6, 9, and 11 come

from convergent numerical computations, and the corresponding errors in c/v are minute, yet there are significant errors in measuring frequency. This observation supports the statement, made in the next-to-last paragraph of subsection 5B, that frequency measurements are delicate.

APPENDIX C: PERTURBATION OF INFLECTION POINTS

Section 2 shows that the inflection-point technique yields our most reliable data, but those data still have errors. Those errors are estimated here in two ways. The estimates do not change the paper's conclusions.

Inflection points follow imperfectly the slow upward drift in Fig. 6. There is an urge to displace points, especially the negative-valued one at 1.2×10^{-11} sec, to slightly later times: displaced points would follow the drift. To estimate the effect of such displacement, imagine that only the most deviant point—the one at 1.2×10^{-11} sec—were moved. Then the circle in Fig. 8 at 2.2×10^{12} /sec would draw toward a slightly lower frequency and the circle at 1.6×10^{12} /sec would move to a higher frequency, improving the fit to 2×10^{11} /sec damping. Thus, replacing inflection points with points that more closely follow the drift in Fig. 6 would reinforce the paper's conclusion slightly.

The next-to-last paragraph of Section 2 notes a second suggestion in the data that inflection points be moved to later times. In the context of that paragraph, systematic error can be estimated pessimistically by shifting two inflection points in Fig. 6 (the ones at 1.2×10^{-11} sec and 1.4×10^{-11} sec) by equal amounts, to about the midpoints of neighboring extrema. Such a shift would not affect

instantaneous frequency (4) but it would increase slowness, which is 1.3, by 1%. A 1% shift of the corresponding point in Fig. 8 would not bring it into line with zero damping. A similar shift of the inflection points that correspond to slowness 1.5, would be less justifiable because a neighboring extremum is outside the range from 0 to 1.6×10^{-11} sec for which convergence in Fig. 6 is evident. In any case, the estimated shift for slowness 1.5 would not bring the corresponding point in Fig. 8 into line with zero damping.

We have just shown that error from inflection points is acceptably small.

REFERENCES

1. Richard L. Smith, "The Velocities of Light," Am. J. Phys. 38, 978-984 (1970).
2. S. C. Bloch, "Eighth velocity of light," Am. J. Phys. 45, 538-549 (1977).
3. R. Loudon, "The propagation of electromagnetic energy through an absorbing dielectric," J. Phys. A: Gen. Phys. 3, 233-245 (1970).

4. Kurt Edmund Oughstun and George C. Sherman, "Propagation of electromagnetic pulses in a linear dispersive medium with absorption (the Lorentz medium)," J. Opt. Soc. Am. B 5, 817-849 (1988), Section 1.
5. Philippe Wyns, Daniel P. Foty, and Kurt E. Oughstun, "Numerical analysis of the precursor fields in linear dispersive pulse propagation," J. Opt. Soc. Am. A 6, 1421-1429 (1989).
6. Kurt Edmund Oughstun and George C. Sherman, "Uniform asymptotic description of electromagnetic pulse propagation in a linear dispersive medium with absorption (the Lorentz medium)," J. Opt. Soc. Am. A 6, 1394-1420 (1989).
7. Kurt E. Oughstun, Philippe Wyns, and Daniel Foty, "Numerical determination of the signal velocity in dispersive pulse propagation," J. Opt. Soc. Am. A 6, 1430-1440 (1989).
8. Kurt Edmund Oughstun and George C. Sherman, "Uniform asymptotic description of ultrashort rectangular optical pulse propagation in a linear, causally dispersive medium," Phys. Rev. A 41, 6090-6113 (1990).
9. Richard Albanese, John Penn, and Richard Medina, "Short-rise-time microwave pulse propagation through dispersive biological media," J. Opt. Soc. Am. A 6, 1441-1446 (1989).
10. Kurt Edmund Oughstun and Shioupyn Shen, "Velocity of energy transport for a time-harmonic field in a multiple-resonance Lorentz medium," J. Opt. Soc. Am. B 5, 2395-2398 (1988).

11. John David Jackson, *Classical Electrodynamics* 2nd edn. (Wiley, New York, 1975), pp. 285, 306-318.
12. Peter Pleshko, *Transients in Guiding Structures* (Ph.D. thesis, New York University, 1969), University Microfilms International, 300 N. Zeeb Road, Ann Arbor, MI 48106. See Section IID, esp. Fig. 16.
13. John R. Reitz, Frederick J. Milford, and Robert W. Christy, *Foundations of Electromagnetic Theory* 3rd edn. (Addison-Wesley, Reading, MA, 1980), pp. 439-440.
14. A. Sommerfeld, "Über die Fortpflanzung des Lichtes in dispergierenden Medien," *Ann. Phys.* 44, 177-202 (1914).
15. L. Brillouin, "Über die Fortpflanzung des Lichtes in dispergierenden Medien," *Ann. Phys.* 44, 203-240 (1914).
16. L. Brillouin, *Wave Propagation and Group Velocity* (Academic, New York, 1960).
17. A. M. Nicolson and G. F. Ross, "Measurement of the Intrinsic Properties of Materials by Time-Domain Techniques," *IEEE Trans. on Instrumentation and Measurement* IM-19, 377-382 (1970).
18. Magdy F. Iskander and Stanislaw S. Stuchly, "A Time-Domain Technique for Measurement of the Dielectric Properties of Biological Substances," *IEEE Trans. on Instrumentation and Measurement* IM-21, 425-429 (1972).
19. E. H. Grant, R. J. Sheppard, and G. P. South, *Dielectric Behavior of Biological Molecules in Solution* (Clarendon, Oxford, 1978), Section 3.6.

20. Peter Fuks, Gerhard Kristensson, and Gunnar Larson, "Permittivity profile reconstructions using transient electromagnetic reflection data," distributed as report "coden:lutedx (teat-7009) 1-88 (1990)" by Department of Electromagnetic Theory, Lund Institute of Technology, P. O. Box 118, S-221 00 Lund, Sweden.
21. G. Kristensson and R. J. Krueger, "Direct and inverse scattering in the time domain for a dissipative wave equation. Part 1: Scattering operators," J. Math. Phys. 27, 1667-1682 (1986); "Direct and inverse scattering in the time domain for a dissipative wave equation. Part 2: Simultaneous reconstruction of dissipation and phase velocity profiles," J. Math. Phys. 27, 1683-1693 (1986); "Direct and inverse scattering in the time domain for a dissipative wave equation. Part 3: Scattering operators in the presence of a phase velocity mismatch," J. Math. Phys. 28, 360-70 (1987); "Direct and inverse scattering in the time domain for a dissipative wave equation. Part 4: use of phase velocity mismatches to simplify equations," Inverse Problems 5, 375-88 (1989).
22. R. S. Beezley and R. J. Krueger, "An electromagnetic inverse problem for dispersive media," J. Math. Phys. 26, 317-325 (1985).
23. Anders Karlsson, "Direct and inverse electromagnetic scattering from a dispersive medium," distributed as report "TRITA-TET 89-1 (January 1989)" by Division of Electromagnetic Theory, Royal Institute of Technology, 100 44 Stockholm, Sweden.

24. Gerhard Kristensson, "Direct and inverse scattering problems in dispersive media—Green's functions and invariant imbedding techniques," in *Direct and Inverse Boundary Value Problems* (Ralph Kleinman, Rainer Kress, and Erich Martensen eds., Peter Lang, Frankfurt, 1991) Methoden und Verfahren der mathematischen Physik, Volume 37.
25. J. P. Corones, M. E. Davison, and R. J. Krueger, "Dissipative inverse problems in the time domain," in *Inverse Methods in Electromagnetic Imaging* (W.-M. Boerner et al. eds., Reidel, Dordrecht, Holland, 1985) Part 1, pp. 121–130.
26. R. J. Krueger and R. L. Ochs, Jr., "A Green's function approach to the determination of internal fields," *Wave Motion* 11, 525–543 (1989).
27. Rodney D. Stewart, *Transient Electromagnetic Scattering on Anisotropic Media* (Ph.D. thesis, Iowa State University, 1989).
28. K. L. Kreider, "Time dependent direct and inverse electromagnetic scattering for the dispersive cylinder," *Wave Motion* 11, 427–440 (1989).
29. K. L. Kreider, "Time dependent linear transport via Green's functions," *Transport Theory and Statistical Physics* 18, 513–526 (1989).
30. Thomas M. Roberts, "Causality Theorems," to appear in *Inverse Problems and Invariant Imbedding* (SIAM, Philadelphia).
31. James B. Scarborough, *Numerical Mathematical Analysis* 6th edn. (Johns Hopkins, Baltimore, 1966) articles 155 and 161.
32. W. Edwards Deming, *Statistical Adjustment of Data* (Wiley, New York, 1948) articles 20 and 21. Note the last sentence of article 21.

Inversion Method for Depth-dependent Dispersive Media

1 Problem Statement

We wish to use reflection data to determine the dispersive properties of a flat slab that has boundaries at $z = 0$ and L . The slab's dispersive properties are defined by the Maxwell equations $\nabla \cdot D = \nabla \cdot B = \nabla \times E + \partial_t B = 0$, $B = \mu_0 H$, and $\nabla \times H = \partial_t D + J$, and by the constitutive relations [1]–[2]

$$(1) \quad \begin{aligned} D(x, t) &= \epsilon_0 E(x, t) + \int_0^t ds W_D(x, t-s) E(x, s) \\ J(x, t) &= \sigma(x) E(x, t) + \int_0^t ds W_J(x, t-s) E(x, s). \end{aligned}$$

That two-sentence problem statement assumes that the permittivity ϵ_0 and permeability μ_0 of the slab are equal to their free-space values, as is true for many nonmagnetic materials. The slab (1) is stratified in one spatial dimension z , and the dispersive properties in (1) are functions of the variable t also. Such functions of the two variables z and t will be inferred from reflection data as a function of the time t and the angle of incidence θ . We will now use a gauge for dispersion to simplify (1) and to establish a fundamental physical limitation on the ability of purely electromagnetic experiments to determine σ , W_D , and W_J .

A dispersion gauge was developed recently [3]; it is easy to understand. A gauge is a

free parameter that does not affect fields. In electrostatics, for instance, the notation

$$(2) \quad \phi_{(\alpha)} = \phi + \alpha$$

reminds us that the scalar potential is arbitrary to within an additive gauge constant α because the electric field $E = -\nabla(\phi + \alpha)$ is independent of α . For that reason the potential $\phi_{(\alpha)}$ is said to be gauge dependent and E is said to be gauge independent. It is physically impossible to measure gauge-dependent quantities: That is why two potentials $\phi_{(\alpha)}$ and $\psi_{(\alpha)}$ can't be measured separately, although the difference $\phi_{(\alpha)} - \psi_{(\alpha)} = (\phi + \alpha) - (\psi + \alpha) = \phi - \psi$ is gauge-independent and physically measurable. Many undergraduate [4] and graduate [5] physics texts use the vector potential as a second example of the physical impossibility of measuring gauge-dependent quantities. This physical principle, that gauge-dependent quantities can't be measured directly, also applies to the dispersion gauge.

The dispersion gauge is any function $f(x, t)$ that has a time derivative and for which $f(x, 0+) = \lim_{t \rightarrow 0} f(x, t)$ exists and is finite. The gauge affects the displacement D , the current J , and the dispersion-related quantities σ , W_D , and W_J by way of

$$(3) \quad \begin{aligned} \nabla \times H &= \partial_t D_{(f)} + J_{(f)} \\ D_{(f)}(x, t) &= \epsilon_0 E(x, t) + \int_0^t ds W_{D,(f)}(x, t-s) E(x, s) \\ J_{(f)}(x, t) &= \sigma_{(f)}(x) E(x, t) + \int_0^t ds W_{J,(f)}(x, t-s) E(x, s) \\ W_{D,(f)}(x, t) &= W_D(x, t) - f(x, t) \\ W_{J,(f)}(x, t) &= W_J(x, t) + \partial_t f(x, t) \\ \sigma_{(f)}(x) &= \sigma(x) + f(x, 0+). \end{aligned}$$

It is easy to verify [3] that H and E are independent of f ; that is, H and E are independent of gauge. We will now show that the total current \mathcal{J} and the dispersion kernel γ

$$(4) \quad \mathcal{J}(x, t) = \partial_t D_{(f)}(x, t) + J_{(f)}(x, t)$$

$$(5) \quad \gamma(x, t) = \sigma_{(f)}(x) + W_{D,(f)}(x, t) + \int_0^t ds W_{J,(f)}(x, s)$$

are also independent of gauge. The total current \mathcal{J} is independent of the gauge f because the gauge independence [3] of H implies that both sides of the first equation in (3) are independent of f . The gauge independence of γ is established by using (3) to expand the terms on the right-hand side of (5). We have just established a fundamental result:

THEOREM 1.1 *Each of the quantities $D_{(f)}$, $J_{(f)}$, $\sigma_{(f)}$, $W_{D,(f)}$, and $W_{J,(f)}$ is gauge dependent. The fields E and H , the total current \mathcal{J} , and the dispersion kernel γ are gauge independent. Consequently $\gamma(x, 0+)$ and $\partial_t \gamma(x, t)$ also are independent of gauge. If W_D and W_J are sufficiently smooth, then $\gamma(x, 0+) = \sigma(x) + W_D(x, 0+)$ and $\partial_t \gamma(x, t) = W_J(x, t) + \partial_t W_D(x, t)$.*

This elementary theorem is important because, as the second paragraph of this section reminds us, gauge-dependent quantities can't be measured. That is, in the framework of the constitutive relations (1), it is impossible to measure the gauge-dependent quantities $\sigma_{(f)}$, $W_{D,(f)}$, and $W_{J,(f)}$ separately; for that reason, the following sections of this paper concentrate on measuring the gauge-independent combination $\partial_t \gamma = \partial_t W_{D,(f)} + W_{J,(f)}$.

A CAUTIONARY NOTE: Theorem 1.1 (above) has the following cautionary implication relating to energy density. Many energy-density computations are based on Poynting's

equation $E \cdot (\nabla \times H) = E \cdot J$, in which both sides are independent of gauge. However, some matters associated with the related energy-density computations are "open to some criticism," says [6] in a discussion of nondispersive media; but for dispersive media there is one more matter of concern: Some energy-density computations [6] have separate physical interpretations for the terms $E \cdot \partial_t D_{(f)}$ and $E \cdot J_{(f)}$; yet theorem 1.1 (above) implies that those terms can not be measured separately. The term $E \cdot J$, however, is independent of gauge, and can therefore be expected to be physically measurable.

2 Method of Solution

Apply the gauge $f = W_D$ to (3) to obtain the dispersive-conductivity representation

$$(6) \quad \begin{aligned} D(x, t) &= \epsilon_0 E(x, t) \\ J(x, t) &= \bar{\sigma}(x) E(x, t) + \int_0^t ds g(x, t-s) E(x, s) \\ \bar{\sigma}(x) &= \gamma(x, 0+) = \sigma(x) + W_D(x, 0+) \\ g(x, t) &= \partial_t \gamma(x, t) = W_J(x, t) + \partial_t W_D(x, t) \end{aligned}$$

of the constitutive relations in (1). Theorem 1.1 says that $\bar{\sigma}$ and g are gauge independent. One published assertion [7] may be interpreted as suggesting that $\bar{\sigma}$ must be 0; but the assertion, as printed in [7], is not substantiated in the text of [7]. In this presentation we assume merely that $\bar{\sigma}(x)$ is a known function; we do not necessarily assume $\bar{\sigma} = 0$. Our inverse problem, therefore, is to infer $g(x, t)$ from time-dependent reflection data as a function of the angle of incidence θ .

We assume that $\bar{\sigma} \in L_\infty[0, L]$ and $g \in L_\infty([0, L] \times [0, \infty))$. Then the techniques of [8] and [3] imply that there are integrable functions R and T such that

$$(7) \quad \begin{aligned} (\mathcal{R}f)(t) &= \int_0^t ds R(t-s) f(s) \\ (\mathcal{T}f)(t) &= \exp \left[- \int_0^L dz \bar{\sigma}(x)/(2c_0) \right] \left[f(t - L/c_0) + \int_0^{t-L/c_0} ds T(t - L/c_0 - s) f(s) \right] \end{aligned}$$

are the time-dependent reflected field $(\mathcal{R}f)(t)$ and transmitted field $(\mathcal{T}f)(t)$ produced by a field f incident on the spatially heterogeneous slab (6) of length L . The speed of light in free space $c_0 = 1/\sqrt{\mu_0 \epsilon_0}$ is used in (7).

The Redheffer operator product [9] shows that the reflection operator for a composite formed of two slabs is

$$(8) \quad \mathcal{R}_c = \mathcal{R}_1 + \mathcal{T}_1(1 - \mathcal{R}_2\mathcal{R}_1)^{-1}\mathcal{R}_2\mathcal{T}_1,$$

where each numerically subscripted operator has the form (7). A little thought shows that the inverse operator in (8) exists and has a resolvent-kernel representation [10] that is related to a Volterra integral equation of the second kind, whose difference kernel is $\int_0^{t-s'} ds' R_2(t-s-s')R_1(s')$. The resolvent-kernel representation and the integral representations in (7) are used to expand the four-operator composition $\mathcal{T}_1(1 - \mathcal{R}_2\mathcal{R}_1)^{-1}\mathcal{R}_2\mathcal{T}_1$ in (8) in terms of the integral kernels of the operators. A discretization of that four-operator composition is used to solve the inverse problem.

A long derivation shows that the integral kernel R_c^θ of the operator \mathcal{R}_c has the form

$$(9) \quad R_c^\theta(t + \delta) = A_1^\theta(t) + B_1^\theta(t)G_1(t + \delta) + C_1^\theta(t)R_2^\theta(t + \delta - 2x_1/c_0) + O(\delta^3),$$

in which $R_c^\theta(t + \delta)$ is the reflection-kernel data at a time $t + \delta$ that is slightly later than t , $G_1(t + \delta) = g[x_0, (t + \delta)]$ is evaluated at the first spatial discretization point $x_0 = 0$, $R_2^\theta(t + \delta - 2x_1/c_0)$ is the reflection kernel for the whole slab with the layer $[0, x_1)$ removed, and the quantities A_1^θ , B_1^θ , and C_1^θ depend on g for times equal to or earlier than t and on R_2^θ for times equal to or earlier than $t - 2x_1/c_0$. The superscripts in (9) are reminders that, although scattering is generally a function of the incident angle θ , the material properties $g(x, t)$ are independent of θ . The computation of A_1^θ , B_1^θ , and C_1^θ is described in the next section.

The next paragraph shows how (9) is used for inversion when the slab $[0, L)$ is discretized into three spatial intervals. The three-interval discretization is generalized to n layers later in this section.

This paragraph describes the central idea in the new inversion method used here. This central idea is illustrated by discretizing the slab $[0, L)$ into three spatial layers $[0, x_1)$, $[x_1, x_2)$, and $[x_2, L)$, and adding a free-space layer $[L, \infty)$. Omitting time dependences such as (t) , $(t + \delta)$, $(\tau + \delta - 2x_i/c_0)$, and so forth, we iterate (9) as follows:

$$\begin{aligned} R_c^\theta &= A_1^\theta + B_1^\theta G_1 + C_1^\theta (A_2^\theta + B_2^\theta G_2 + C_2^\theta R_3^\theta) = \\ (10) \quad R_c^\theta &= A_1^\theta + B_1^\theta G_1 + C_1^\theta A_2^\theta + C_1^\theta B_2^\theta G_2 + C_1^\theta C_2^\theta (A_3^\theta + B_3^\theta G_3 + C_3^\theta R_4^\theta) = \\ R_c^\theta &= (A_1^\theta + C_1^\theta A_2^\theta + C_1^\theta C_2^\theta A_3^\theta) + B_1^\theta G_1 + C_1^\theta B_2^\theta G_2 + C_1^\theta C_2^\theta B_3^\theta G_3. \end{aligned}$$

The recursive derivation (10) follows from (9) in the context of layer stripping. In particular, (9) relates the reflection R_c^θ from the four-layer composite $[0, \infty) = [0, x_1) \cup [x_1, x_2) \cup [x_2, L) \cup [L, \infty)$ to the dispersion kernel G_1 of the first layer $[0, x_1)$ and to the reflection R_2^θ from the three-layer, stripped composite $[x_1, \infty) = [x_1, x_2) \cup [x_2, L) \cup [L, \infty)$. But the three-layer composite can be similarly related, by using (9) again, to the reflection from the two-layer, stripped composite $[x_2, \infty) = [x_2, L) \cup [L, \infty)$. Thus, one iteration of (9) yields the first line of (10), in which R_3^θ is the reflection kernel for the two-layer, stripped composite $[x_2, L) \cup [L, \infty)$. The recursive derivation (10) terminates with the reflection kernel $R_4^\theta = 0$ because the reflection R_4^θ from the free-space layer $[L, \infty)$ is zero. Because of the recursive nature of the derivation, the numerical algorithm that is used to compute the coefficients A_1^θ , B_1^θ , and C_1^θ for the first composite $[0, \infty)$ can also be used to compute the general coefficients A_i^θ , B_i^θ , and C_i^θ for any of the stripped composites $[x_{i-1}, \infty)$. The algorithm for computing A_i^θ , B_i^θ , and C_i^θ is described in the next section. Please note that every θ -dependent term in (10) is marked with a θ so as to emphasize that the θ -independent unknowns G_1 , G_2 , and G_3 can be determined by measuring the reflection R_c^θ from the full composite $[0, \infty)$ for three angles of incidence θ , and then inverting the three-by-three matrix equation that is implicit in the last line of (10).

We will now present a matrix equation for an n -layer, $(n+1)$ -point spatial discretization $x_0, x_1, x_2, \dots, x_n$ of the slab $[0, L)$. The n -layer generalization of (10) is

$$(11) \quad B_1^\theta G_1 + \sum_{j=2}^n B_j^\theta G_j \prod_{k=1}^{j-1} C_k^\theta = R_c^\theta - A_1^\theta - \sum_{j=2}^n A_j^\theta \prod_{k=1}^{j-1} C_k^\theta,$$

in which all the G_j terms are on the left side of the equality. If R_c^θ is measured for N angles θ then (11) is equivalent to the matrix equation

$$(12) \quad M \cdot [G_1, G_2, \dots, G_n]^T = [v_1, v_2, \dots, v_N]^T,$$

for which the i, j element of the matrix M is

$$(13) \quad M_{i,j} = \begin{cases} B_{i,1}, & \text{if } j = 1; \\ B_{i,j} \prod_{k=1}^{j-1} C_{i,k}, & \text{otherwise} \end{cases}$$

and

$$(14) \quad v_i = R_{i,c} - A_{i,1} - \sum_{k=2}^n A_{i,k} \prod_{l=1}^{k-1} C_{i,l},$$

and T denotes transposition. For each $i = 1, 2, \dots, N$ the quantities $A_{i,j}$, $B_{i,j}$, $C_{i,j}$, and $R_{i,c}$ stand for A_j^θ , B_j^θ , C_j^θ , and R_c^θ evaluated at the incident angle $\theta = \theta_i$. If the number of measurement angles N is greater than the number of layers n , then the system (12) is overdetermined. If $N = n$ then

$$(15) \quad [\dot{G}_1, G_2, \dots, G_n]^T = M^{-1} \cdot [v_1, v_2, \dots, v_n]^T.$$

3 Computational Algorithm

An inverse scattering problem for heterogeneous dispersive media is defined in (6). The last steps in the algorithmic solution are (12)–(15). All that remains is to show how the quantities A_j^θ , B_j^θ , and C_j^θ in (12)–(15) are related to the material parameters defined in (6). That relation is presented here in the form of a computational algorithm. The algorithm comes from derivations that are much too long to report here.

The following three-page computational algorithm documents the extent of development of a solution to the inverse problem identified in this paper's first paragraph. The three-page algorithm itself contains no new ideas; the new ideas in this paper are all in section 1 and in the paragraph that includes equation (10). The algorithm is worthwhile because it is ready to be programmed.

First define $c = [\mu_0 \epsilon_0 - (\sin^2 \theta)/c_0]^{-1/2}$, $\xi = x/L$, and $\tau = ct/L$, in terms of the total length L of the slab and the angle of incidence θ . The slab interval is $[0, L)$ in the ordinary spatial coordinate x and $[0, 1)$ in the unitless coordinate ξ . In this section, functions of unitless variables such as $g(\xi, \tau)$ are understood to be related to functions of x and t according to the rule $g(\xi, \tau) = g(x/L, tL/c)$. We will discretize the unitless variables as $\xi = ih$ and $\tau = 2jh$, for any h that is the reciprocal of a positive integer.

For the sake of computational efficiency, in case the slab has some thick homogeneous layers, we define indexes $0 = L_0 < L_1 < L_2 < \dots < L_n = 1/h$ for the boundaries of the layers; in particular, for each i , $g(\xi, \tau)$ and $\bar{\sigma}(\xi)$ are constant $\forall \xi \in [hL_{i-1}, hL_i)$. The layer indexes do not restrict the generality of this work because, if there is no thick homogeneous layer, then we set $L_i = i$ for $i = 0, 1, 2, \dots, n$. The notation $L(i) = L_i$ is used later in subscripts such as $g_{L_i} = g_{L(i)}$.

The algorithm in this section is derived using layer stripping, as is symbolized in (10). If we strip layers 1 through $(i-1)$ from the laminated slab, then the remainder $[hL_{i-1}, 1)$ of the laminate is

$$(16) \quad \begin{aligned} g_R^{(i)}(\xi, \tau) &= g(\xi + hL_{i-1}, \tau)H(\xi) \\ \bar{\sigma}_R^{(i)}(\xi) &= \bar{\sigma}(\xi + hL_{i-1})H(\xi), \end{aligned}$$

where H is Heaviside's step function. Each stripped layer $[hL_{i-1}, hL_i)$ has the electromagnetic properties

$$(17) \quad \begin{aligned} g_L^{(i)}(\xi, \tau) &= g_R^{(i)}(\xi, \tau)H(hL_i - hL_{i-1} - \xi) \\ \bar{\sigma}_L^{(i)}(\xi) &= \bar{\sigma}_R^{(i)}(\xi)H(hL_i - hL_{i-1} - \xi). \end{aligned}$$

Let

$$(18) \quad g_j^{(i)} = g(hL_{i-1}, 2jh), \quad \bar{\sigma}^{(i)} = \bar{\sigma}(hL_{i-1})$$

represent the slab's properties at the left face of the i^{th} layer $[hL_{i-1}, hL_i]$, and let

$$(19) \quad p^{(i)} = -\mu_0 h(L_i - L_{i-1}) L c \bar{\sigma}^{(i)} / 2.$$

Let $G_R^{(i)\pm}(\xi, \tau)$ be Krueger-Ochs Green functions [8], such that

$$(20) \quad \begin{aligned} E_R^{(i)\pm}(\xi, \tau) &= \frac{1}{2} \left[E_R^{(i)}(\xi, \tau) \mp \int_0^\tau ds \partial_\xi E_R^{(i)}(\xi, s) \right] \\ E_R^{(i)}(\xi, \tau) &= E_R^{(i)+}(\xi, \tau) + E_R^{(i)-}(\xi, \tau) \\ E_R^{(i)+}(\xi, \tau) &= \exp[-\bar{\sigma}^{(i)} \xi L / (2c)] \left[f(\tau - \xi) + \int_0^{\tau - \xi} ds G_R^{(i)+}(\xi, \tau - s) f(s) \right] \\ E_R^{(i)-}(\xi, \tau) &= \int_0^{\tau - \xi} ds G_R^{(i)-}(\xi, \tau - s) f(s) \end{aligned}$$

solve the scattering problem of fields f incident on the stripped slab $g_R^{(i)}, \bar{\sigma}_R^{(i)}$ ($i = 1, 2, \dots, n$). Similarly, let $G_L^{(i)\pm}(\xi, \tau)$ be the Krueger-Ochs Green functions that solve the scattering problem for the isolated, stripped layer $g_L^{(i)}, \bar{\sigma}_L^{(i)}$ ($i = 1, 2, \dots, n$). Such Krueger-Ochs Green functions were originally developed analytically and numerically for nondispersive media [8], then generalized and numerically validated for normal incidence on dispersive media [11], and then generalized to oblique incidence [3].

Let us now re-introduce the time arguments that were omitted from (10)–(15). Equation (11) then becomes

$$(21) \quad \begin{aligned} B_1^\theta g(hL_0, \tau + \delta) + \sum_{j=2}^n B_j^\theta g(hL_{j-1}, \tau + \delta - 2hL_{j-1}) \prod_{k=1}^{j-1} C_k^\theta &= \\ &= R_c^\theta(\tau + \delta) A_1^\theta(\tau) - \sum_{j=2}^n A_j^\theta(\tau - 2hL_{j-1}) \prod_{k=1}^{j-1} C_k^\theta. \end{aligned}$$

Define

$$(22) \quad \begin{aligned} A_j^{(i)} &= A_i^\theta[2(j - L_{i-1})h] \\ B^{(i)} &= B_i^\theta \\ C^{(i)} &= C_i^\theta \\ G_{R,i,J}^{(i)\pm} &= G_R^{(i)\pm}(ih, 2Jh) \\ G_{L,i,J}^{(i)\pm} &= G_L^{(i)\pm}(ih, 2Jh), \end{aligned}$$

with $A_j^{(i)} = 0$ when $j < L_{i-1}$. Replace τ and δ with $2Jh$ and $2h$ in (21) to obtain

$$(23) \quad B^{(1)} g_{J+1}^{(1)} + \sum_{k=2}^n B^{(k)} g_{J+1-L(j-1)}^{(k)} \prod_{l=1}^{k-1} C^{(l)} = R_c^\theta[2(J+1)h] - A_J^{(1)} - \sum_{k=2}^n A_J^{(k)} \prod_{l=1}^{k-1} C^{(l)}.$$

Equation (23) is of the same form as (11), except that (23) denotes the time dependence more explicitly. Equations (21)–(23) indicate correctly that $B^{(i)}$ and $C^{(i)}$ are time independent; in fact, a long derivation shows that

$$(24) \quad \begin{aligned} B^{(i)} &= (h/2)[2 + hp^{(i)}] / [2 - hp^{(i)} - h^2 g_0^{(i)}] \\ C^{(i)} &= \exp[p^{(i)} \lambda_i / c] \left\{ 1 + 2h G_{L,\lambda(i),0}^{(i)+} + h^2 \left[G_{L,0,0}^{(i)-} G_{R,0,0}^{(i+1)-} + G_{L,\lambda(i),0}^{(i)+} G_{L,\lambda(i),0}^{(i)+} \right] \right\}, \end{aligned}$$

where $\lambda(i) = \lambda_i = L_{i+1} - L_i$.

The only task remaining is to show how to compute $A_j^{(i)}$. That task is the longest one in this section and, because of a triple integral in (27), it is also the most computationally intensive task here. The triple integral is of convolutional form, however, so the fast-Fourier-transform (fft) technique for computing convolutions can be applied. The fft technique would speed up the triple-integral computation, but, if one of the integrands has a Fourier transform that is broad banded, then the fft technique may be significantly less accurate than would a straightforward trapezoid-rule computation of the triple integral in (27).

Define

$$\begin{aligned}
 K^{(i)}(t) &= \int_0^t ds G_R^{(i+1)-}(0, t-s) G_L^{(i)-}(0, s) \\
 \rho^{(i)}(t) &= K^{(i)}(t) + \int_0^t ds K^{(i)}(t-s) \rho^{(i)}(s) \\
 \eta^{(i)}(t) &= \rho^{(i)}(t) + G_L^{(i)+}(h\lambda_i, t) \\
 r_{k,J}^{(i)} &= \exp[khp^{(i)}] g_J^{(i)} \\
 \Lambda_{k,J}^{(i)\pm} &= h \left[g_0^{(i)} G_{L,k,J}^{(i)\pm} + g_J^{(i)} G_{L,k,0}^{(i)\pm} + 2 \sum_{j=1}^{J-1} g_j^{(i)} G_{L,k,J-j}^{(i)\pm} \right].
 \end{aligned}
 \tag{25}$$

The quantity $\rho^{(i)}$ is the resolvent kernel [10] for a Volterra integral equation of the second kind, whose difference kernel is $K^{(i)}(t, s) = K^{(i)}(t-s)$. A time-discretized version of $\rho^{(i)}(t)$ can be computed by inverting a triangular matrix, which can be done with Gaussian elimination and scaling. Next, compute

$$\begin{aligned}
 A_J^{(i)} &= b_J^{(i)} + \beta_J^{(i)} \\
 b_J^{(i)} &= \left[2 - hp^{(i)} - h^2 g_0^{(i)} \right]^{-1} \times \\
 &\quad \times \left\{ 2G_{L,1,J}^{(i)-} + h \left[p^{(i)} G_{L,1,J}^{(i)+} + p^{(i)} G_{L,1,J}^{(i)-} + r_{1,J}^{(i)} + \Lambda_{1,J}^{(i)+} + \Lambda_{1,J}^{(i)-} + 2h \sum_{j=1}^J g_j^{(i)} G_{L,0,J+1-j}^{(i)-} \right] \right\} \\
 \beta_1^{(i)} &= h G_{R,0,0}^{(i+1)-} \exp[p^{(i)} \lambda_i / c] \left\{ 2G_{L,\lambda(i),1}^{(i)+} + h \left[G_{L,0,1}^{(i)-} G_{R,0,0}^{(i+1)-} + G_{L,0,1}^{(i)+} G_{L,0,0}^{(i)+} \right] \right\} \\
 \beta_J^{(i)} &= \exp[p^{(i)} \lambda_i / c] \left[\zeta_{0,J}^{(i)} + \zeta_{1,J}^{(i)} + \zeta_{2,J}^{(i)} + \zeta_{3,J}^{(i)} \right], \text{ for } J \geq 2.
 \end{aligned}
 \tag{26}$$

Finally, compute

$$\begin{aligned}
 \zeta_{3,J}^{(i)} &= \int_0^{2Jh} ds G_L^{(i)+}(h\lambda_i, 2Jh + 2h - s) \int_0^s ds' \rho^{(i)}(s-s') \int_0^{s'} ds'' G_R^{(i+1)-}(0, s' - s'') G_L^{(i)}(h\lambda_i, s'') \\
 \zeta_{2,J}^{(i)} &= \left(\int_{2h}^{2Jh} ds \left\{ \left[1 + h G_{L,\lambda(i),0}^{(i)+} \right] \rho^{(i)}(2Jh + 2h - s) + G_L^{(i)}(h\lambda_i, 2Jh + 2h - s) \circ \right. \right. \\
 &\quad \circ \int_0^s ds' G_R^{(i+1)-}(0, s - s') G_L^{(i)+}(h\lambda_i, s') + \int_0^{2Jh} ds \rho^{(i)}(2Jh - s) \circ \\
 &\quad \left. \left. \circ \int_0^s ds' G_R^{(i+1)-}(0, s - s') \left[G_L^{(i)+}(h\lambda_i, s' + 2h) + h G_{L,\lambda(i),1}^{(i)+} G_L^{(i)+}(h\lambda_i, s') \right] \right\} \right)
 \end{aligned}
 \tag{27}$$

(28)

$$\begin{aligned}
\zeta_{1,J}^{(i)} = & \left[\int_{2h}^{2Jh} ds \left(\left\{ \left[1 + hG_{L,\lambda(i),0}^{(i)+} \right] G_R^{(i+1)-}(2Jh+2h-s) + h\eta^{(i)}(2h)G_R^{(i+1)-}(0,2Jh-s) \right\} \times \right. \right. \\
& \times G_L^{(i)+}(h\lambda_i, s) + \left[\eta^{(i)}(2Jh+2h-s) + hG_{L,\lambda(i),0}^{(i)+} \rho^{(i)}(2Jh+2h-s) + \right. \\
& \left. \left. + hG_{L,\lambda(i),1}^{(i)+} \rho^{(i)}(2Jh-s) \right] G_R^{(i+1)-}(0, s) \right) + \\
& + hG_{R,0,0}^{(i+1)-} \left[1 + hG_{L,\lambda(i),0}^{(i)+} \right] \times \\
& \times \int_{2h}^{2Jh} ds \left[K^{(i)}(2Jh+2h-s) \rho^{(i)}(s) + G_R^{(i+1)-}(0, 2Jh+2h-s) G_L^{(i)-}(0, s) \right] \Big] \\
\zeta_{0,J}^{(i)} = & \left[h \left\{ G_{R,0,1}^{(i+1)-} \left[\eta^{(i)}(2Jh) + G_{L,\lambda(i),J}^{(i)+} \right] + 2G_{R,0,0}^{(i+1)-} G_{L,\lambda(i),J+1}^{(i)+} + G_{R,0,J}^{(i+1)-} \left[\eta^{(i)}(2h) + G_{L,\lambda(i),1}^{(i)+} \right] \right\} + \right. \\
& + h^2 \left(G_{R,0,0}^{(i+1)-} \left[G_{R,0,1}^{(i+1)-} G_{L,0,J}^{(i)-} + G_{L,0,1}^{(i)-} G_{R,0,J}^{(i+1)-} + G_{R,0,0}^{(i+1)-} G_{L,0,J+1}^{(i)-} \right] + \right. \\
& + G_{L,\lambda(i),0}^{(i)+} \left[2G_{R,0,1}^{(i+1)-} \eta^{(i)}(2Jh) + 2G_{R,0,J}^{(i+1)-} \eta^{(i)}(2h) + G_{R,0,0}^{(i+1)-} G_{L,\lambda(i),J+1}^{(i)+} \right] + \\
& + G_{L,\lambda(i),1}^{(i)+} \left\{ G_{R,0,0}^{(i+1)-} \left[\eta^{(i)}(2Jh) + \rho^{(i)}(2Jh) \right] + \rho^{(i)}(2Jh-2h) G_{R,0,1}^{(i+1)-} + G_{R,0,J-1}^{(i+1)-} \eta^{(i)}(2h) \right\} \Big) + \\
& \left. + O(h^3) \right].
\end{aligned}$$

Of all the $\zeta_{k,J}^{(i)}$ terms, it is $\zeta_{0,J}^{(i)}$ that uses the most ink, but, because it has no integrals, $\zeta_{0,J}^{(i)}$ is easily computed. It is the triple-integral term $\zeta_{3,J}^{(i)}$ in (27) that is the most computationally intensive of the $\zeta_{k,J}^{(i)}$ terms.

It was already noted, in the second paragraph of this section, that the long equations in this section contain no new ideas. The new ideas in this paper are all in section 1 and in the paragraph that includes equation (10).

4 Related Work

A time-domain inverse problem for heterogeneous dispersive media was solved previously in the setting of horizontal-shear acoustic waves [12]. The essential difference between that inversion method and the one presented here is the way in which some crucial matrix entries are computed. In the present paper, the entries of the matrix M and the vector $[v_1, v_2, \dots, v_N]$ in (12) are computed directly, as described in (13)–(14) and in section 3. One of the most interesting new ideas in [12], however, is the method by which its analogous matrix entries are computed; such a computational method would later be called “an implicit scheme” [13]. The implicit scheme in [12] uses numerical experiments to determine matrix elements in a sensible way that is validated numerically in [12]. The method in the present paper, however, uses direct computation in place of numerical experiments. In short, [12] has the first implicit scheme for heterogeneous dispersive (acoustic) media, and the present paper has the first explicit scheme for heterogeneous dispersive (electromagnetic) media.

5 Conclusion

An inverse scattering problem for heterogeneous dispersive media is defined in this paper's first paragraph. The statement of the problem is simplified using the new gauge ideas in section 1. The key to understanding the layer-stripping idea at the center of this paper's algorithmic solution to the inverse problem is to first understand how the derivation in (10) follows from equation (9).

References

- [1] J. Hopkinson, *Residual charge of the Leyden jar.—Dielectric properties of different glasses*, Philos. Trans. Roy. Soc. London, 167 (1877) pp. 599–626, especially p. 601.
- [2] R. Albanese, J. Penn, and R. Medina, *Short-rise-time microwave pulse propagation through dispersive biological media*, J. Opt. Soc. Amer. A, 6 (1989) pp. 1441–1446, especially section 3.
- [3] T. M. Roberts, *Causality Theorems*, in *Invariant Imbedding and Inverse Problems*, J. P. Coronnes, G. Kristensson, P. Nelson, and D. L. Seth eds., SIAM, Philadelphia, 1992, pp. 114–128, especially sections 3, 4, and 7.
- [4] J. B. Marion and M. A. Heald, *Classical Electromagnetic Radiation*, 2nd edn., Academic Press, New York, 1980, especially section 4.6.
- [5] E. J. Konopinski, *Electromagnetic Fields and Relativistic Particles*, McGraw-Hill, New York, 1981, especially p. 174 and index.
- [6] J. A. Stratton, *Electromagnetic Theory*, McGraw-Hill, New York, 1941, especially section 2.19.
- [7] J. D. Jackson, *Classical Electrodynamics*, 2nd edn., Wiley, New York, 1975, subsection 7.10(c), especially the first line of p. 310.
- [8] R. J. Krueger and R. L. Ochs, *A Green's function approach to the determination of internal fields*, Wave Motion, 11 (1989), pp. 525–543, especially section 3.
- [9] J. Coronnes and R. Krueger, *Obtaining Scattering Kernels Using Invariant Imbedding*, J. Math. Anal. Appl., 95 (1983), pp. 393–415, especially section III.
- [10] P. Linz, *Analytical and Numerical Methods for Volterra Equations*, SIAM, Philadelphia, 1985, especially theorems 3.1–3.3 and 3.5.
- [11] T. M. Roberts and M. Hobart, *Energy velocity, damping, and elementary inversion*, J. Opt. Soc. Amer. A, 9 (1992) 1091–1101.
- [12] J. Coronnes and A. Karlsson, *Transient direct and inverse scattering for inhomogeneous viscoelastic media: obliquely incident SH mode*, Inverse Problems, 4 (1988) 643–660, especially the paragraph that contains (5.1)–(5.2).
- [13] A. Karlsson, *Direct and inverse electromagnetic scattering from a dispersive medium*, technical report TRITA-TET 89-1, Division of Electromagnetic Theory, Royal Institute of Technology, 100 44 Stockholm, Sweden, 1989, especially p. 5.

1. INTRODUCTION

The computation of electromagnetic pulses in dispersive media is a highly developed field. For instance, a single paper,¹ published in 1976, contains numerics for the propagation of TE- and TM-polarized electromagnetic pulses that are incident obliquely on an inhomogeneous, anomalously dispersive medium. Computational electromagnetics has developed so extensively since 1976 that it now appears that, given enough computer resources, one can compute the propagation of just about any single pulse through just about any single medium. But these studies of single pulses, even of millions of single pulses, have not demonstrated that *every* microwave pulse travels through water² with one-ninth the speed of light in vacuum. That fundamental factor-of-nine effect, which appears to have been unnoticed until now, is established here by studying an electromagnetic wave equation and its scattering operators, which are the natural places to find broadly applicable rules that govern propagation. We will show that the time of arrival of transmitted pulses in anomalously dispersive media is related to a slow speed given by the DC phase velocity in each medium. This paper has several other new results, which relate to the widths and peak amplitudes of pulses, and to quantities that resemble power density. These new results, concerning broad classes of pulses, are validated here using standard numerical methods; a new numerical method for estimating errors is also developed and used, and some results of laboratory experiments on pulse propagation in a muscle-equivalent material are explained. Our results will be shown to be helpful in proposing optimum sample lengths to be used in Time Domain Spectroscopy studies for the accurate determination of the infinite-frequency and static permittivities of Debye-type dispersive media.³⁻⁴ Also, as shown in Section 4, our results can form the basis for a sensitivity analysis of the dependence of the medium response on the parameters obtained from different fits to the same band-limited experimental data.

This work was done, in part, to assist in the development of health-and-safety regulations for electromagnetic pulses in human environments. Our goal was to develop methods to support the regulation of basic quantities such as the peak amplitude and the power density of incident pulses, so that it would not be necessary to regulate every detail of a pulse's time trace. Toward that end

we formulated a problem in making inferences from incomplete data. We asked: Knowing only the peak amplitude and power density of an incident pulse, what can be said about the peak amplitude of the propagated pulse? We also asked what the incomplete data would imply about the values inside the dispersive medium of the time derivative of the magnetic field H and of a different quantity that is related to power density. Of those three quantities—peak amplitude and power density and $\partial_t H$ —it is $\partial_t H$ whose size is most closely linked to the time scale of short-risetime pulses; further, $\partial_t H$ is particularly important because it would be largely responsible for electromotive-force currents in any circuit-like structure that is inside a dispersive medium. Our results in this matter of incomplete data are quite concrete. We will show, for instance, that the peak amplitude of the electric-field part of a propagated microwave pulse is always less than 0.150 V/m, for depths greater than 2.00 mm in water, whenever the incident electric pulse's peak amplitude is less than 1.00 V/m and its power density is less than 5.29×10^{-14} Watt/m², regardless of the other details of the microwave pulse's time trace. We have similar results for power density and for $\partial_t H$. The development of such general rules for pulse propagation may put the computational basis for pulse-safety standards on as firm a basis as for the existing standards⁵ for continuous waves and periodic wave trains.

This paper's dispersion models and time scales are motivated by laboratory experiments. We use a one-term Debye⁶ model that fits laboratory data for water² up to 100 GHz, and our numerical tests involve pulses with or without DC-frequency content whose time scales are characteristic of short-pulse radar. Our methods apply to all other Debye-like media, and can be generalized for the two-term and five-term Debye models that fit laboratory data for muscle and muscle-equivalent materials.³⁻⁴ Our methods can also be generalized for non-Debye media.

2. PDE FORMULATION AND RESULTS

A. PDEs

The equations governing the scattering and propagation of an obliquely incident pulse on a homogeneous dispersive half-space occupying $z \geq 0$ are the time-domain Maxwell's equations for the fields H_x, H_z, E_y . This set of equations is coupled through a polarization current ($\frac{\partial P_y}{\partial t}$) to an ordinary differential equation that describes the evolution of an orientational polarization (P_y) mechanism of Debye type⁶ (a relaxation process): $\tau \frac{\partial P_y}{\partial t} + P_y = \Delta \epsilon E_y$, where $\Delta \epsilon = \epsilon_s - \epsilon_\infty$, ϵ_s and ϵ_∞ are respectively the zero- and infinite-frequency relative permittivities, and τ is the dielectric relaxation time. This o.d.e. together with the constitutive law, $D_y = \epsilon_o(\epsilon_\infty E_y + P_y)$, result in the model frequency-domain relative permittivity $\epsilon(\omega) = \epsilon_\infty + \frac{\Delta \epsilon}{1 - i\omega\tau}$, where ϵ_o is the permittivity of vacuum. This model is fitted to frequency-domain experimental data for a range of frequencies ω in order to fix the various medium parameters. Typical values for water in the microwave frequency range are $\epsilon_s = 80.35$, $\epsilon_\infty = 1.00$, $\tau = 8.13$ psec. The phase velocity of each frequency component in such a medium is $v^{phase}(\omega) = \frac{c}{\text{Re}\sqrt{\epsilon(\omega)}}$, with c being the speed of light in vacuum. In the subsequent analysis $v^{phase}(0)$ and $v^{phase}(\infty)$ will arise. Finally, operational considerations fix the pulse shape, f , and its duration, T_p .

The electric field incident on the half-space from the air side ($z < 0$) is a plane pulse $E_y^{inc}(x, z, t) = f(t - x \sin \phi_{inc}/c - z \cos \phi_{inc}/c)$ of duration T_p . We assume the pulse has been in contact with the interface since $t = -\infty$. On the interface, $z = 0$, the total electric field is $E_y(x, 0, t) = g(t - x/v)$ where $v = c/\sin \phi_{inc}$; the total field is known by direct measurement of either the field on the interface or of the scattered field in $z < 0$. Defining the time-like variable $\xi = t - x/v$ we find that $E_y(x, z, t) = E_y(0, z, \xi) \rightarrow \tilde{E}_y(z, \xi)$, $H_{x,z}(x, z, t) = H_{x,z}(0, z, \xi) \rightarrow \tilde{H}_{x,z}(z, \xi)$, and that $\tilde{H}_z(z, \xi) = \frac{1}{v\mu_o} \tilde{E}_y(z, \xi)$. Changing coordinates $(x, z, t) \rightarrow (z, \xi)$ in the resulting one-dimensional system, and eliminating \tilde{H}_y through differentiation with respect to ξ and \tilde{P}_y by using the operator $\partial_\xi + \frac{1}{\tau}$, we obtain a single third-order partial differential equation for the electric field $E = \tilde{E}_y$ (shown in factored form),

$$\partial_\xi(\partial_\xi - c_o \partial_z)(\partial_\xi + c_o \partial_z)E + \frac{\beta}{\tau}(\partial_\xi - c_1 \partial_z)(\partial_\xi + c_1 \partial_z)E = 0, \quad z > 0, \quad (2.1)$$

where $c_o = c/(\sqrt{\epsilon_\infty} \cos \phi_{inc})$, $\beta = 1 + \Delta \epsilon/(\epsilon_\infty \cos^2 \phi_{inc})$, and $c_1 = c_o/\sqrt{\beta}$. For $\phi_{inc} = 0$,

$\xi = t$. The signaling problem for (2.1) is completed by giving the boundary condition $E(0, \xi) = g(\xi)$, and the initial data $E(z, 0) = E_\xi(z, 0) = E_{\xi\xi}(z, 0) = 0$. \tilde{H}_z follows once E is known, and $\tilde{H}_z = \frac{1}{\mu_0} \int_0^\xi \frac{\partial E(z, \xi')}{\partial z} d\xi'$. The following results are derived in Subsection 3A.

Equation (2.1) describes the propagation of all possible waves of different orders, and their corresponding speeds, that can be excited by an arbitrary pulse. The coefficients exhibit an explicit dependence on the angle of incidence, and on the parameters that describe the medium. It is a strictly hyperbolic⁷ partial differential equation since the principal part of the operator has real distinct eigenvalues (three eigenvalues, $\pm c_0$ and 0), and a complete set of eigenvectors. Causality follows from this last sentence. The characteristic contributed by the zero eigenvalue can be visualized by considering that $\partial_\xi + c_2 \partial_z = \partial_\xi$ when $c_2 = 0$. The main feature of (2.1) is the two wave equations exhibiting distinct speeds, c_0 and c_1 . Pulse propagation is governed by these two speeds in mutually exclusive spatial regions. Disturbances mainly described by the principal part of the operator in (2.1) will be called high-order waves, while those described by the remaining operator will be called lower-order waves.⁸ The speed c_1 , while not a characteristic speed (it is sub-characteristic, $c_1 < c_0$), is important in the analysis and has several ramifications for experiments. Also, $c_1 = v^{phase}(0)$ and $c_0 = v^{phase}(\infty)$; i.e., the main disturbances will propagate with the distinct speeds which are equal to limiting values of the phase velocity. It is worthwhile to emphasize that experimental data indicates $c_1 \ll c_0$, e.g., $c_1 \sim 0.1116c_0$ for water in the microwave range; the problem is stiff so the pulse travels in the half-space with either of two speeds that are disparate.

The high-order term describes the dominant behavior for depths $z < O(c_0\tau)$ m, and the effect of the lower-order term on the the high-order waves is an exponential decay with z . The penetrating pulse propagates with speed c_0 in this shallow depth ($\sim 10^{-4}$ m for water) which we name the "skin-depth" for pulses since it is reminiscent of the well known frequency-domain concept.² From experimentally obtained data typical of tissue $\tau = O(10^{-12})$ sec, and $\beta = O(10)$. Thus $\frac{\beta}{\tau}$ is large, and we expect the bulk of the penetrated pulse to travel with the speed c_1 since (2.1) is then approximately $E_{\xi\xi} - c_1^2 E_{zz} = 0$. The main disturbance will be a lower-order wave. The effect of the high-order term on the lower-order waves, which travel with speed

c_1 , is diffusive in character and important for $z > O(c_0\tau)$ m. The main response diffuses around the ray $z_s = c_1\xi$ on which the peak of the response is found. The peak amplitude on the sub-characteristic ray decays as $1/\sqrt{z}$, or as $1/\sqrt{\xi}$ (for fixed depth). A consequence of this is that the peak of the energy-like quantity E^2 will decay as $1/z$ ($1/\xi$).

The response will also depend crucially on the pulse duration. This parameter appears through scaling ξ with T_p , and z with cT_p . Now $\frac{\rho}{\tau} \rightarrow \frac{\rho T_p}{\tau}$, and c_0 and c_1 are normalized by c . Pulses with appreciable amplitude most often have $T_p \sim 10^{-8} - 10^{-10}$ sec, so $\frac{\rho T_p}{\tau}$ is still large. Pulses that are long with respect to the relaxation time ($T_p \rightarrow \infty$, or equivalently if $\tau \rightarrow 0$) will propagate unattenuated in the half-space with amplitude equal to the DC value of the frequency-domain transmission coefficient regardless of the pulse's DC-frequency content. The field just after the interface (no "skin-depth" since $c_0\tau \rightarrow 0$) satisfies a lossless wave equation with speed c_1 . On the other hand, very short pulses ($T_p \rightarrow 0$, or equivalently if $\tau \rightarrow \infty$) will not penetrate far. In this case the electric field in the half-space (since now $c_0\tau \rightarrow \infty$) sees a high constant conductivity medium thus it satisfies a telegraphers wave equation whose far-field is the diffusion equation.

B. Green Functions

This subsection describes some rules of wave propagation that are derived from time-domain Green functions. The history of these Green functions is reviewed in Subsection 3B. We will first state some results involving upper bounds on propagated peak amplitudes and power-density-type quantities. These upper bounds are easily computed and they are independent of the detailed nature of the incident fields. The bounds are developed for normal incidence here and for oblique incidence in Subsection 3B. The present section concludes with a description of wave speeds and with brief-pulse and long-pulse approximations. These rules are all illustrated numerically using the water parameters $\epsilon_s = 80.35$, $\epsilon_\infty = 1.00$, and $\tau = 8.13$ psec from Subsection 2A; and the results are easily generalized to other Debye media and to non-Debye media. The necessary derivations and numerical validations are in Subsection 3B and Appendix A.

For normal incidence, let the y -polarized incident electric field be $f(t - z/c_0)$ in the air-filled half-space $z < 0$. In the water-filled half-space $z \geq 0$, the resulting electric field is

$$E(z, t) = E_y(z, t) = \exp\left(\frac{-z}{6.15 \times 10^{-5} \text{m}}\right) f\left(t - \frac{z}{c_0}\right) + \int_0^{t-z/c_0} ds f(s) G_E(z, t-s). \quad (2.2)$$

The Green function $G_E(z, t)$ is graphed in Fig. 1 for several depths $z > 0$. For the boundary $z = 0$, Ref. 9 derives $G_E(0, t) = -t^{-1} \exp[-t/(2.00 \times 10^{-13} \text{s})] I_1[t/(2.05 \times 10^{-13} \text{s})]$, where I_1 is the modified Bessel function of the first kind; the oblique-incidence generalization is (3.12). The magnetic field $H_x(z, t) = -\int_{z/c_0}^t ds \partial_z E_y(z, s)/\mu_0$ also has a Green-function representation similar to (2.2).

Many of our new results are based on (2.2) and Fig. 1. Safety standards may be affected by this type of analysis; so, in Appendix A, we show how to estimate the percentage error in computations, with the following results for our computations: (1) The pointwise numerical error in $G_E(0.500 \text{ mm}, t)$ is no more than 1.70% of the peak value (with respect to t) of $|G_E(0.500 \text{ mm}, t)|$; (2) The pointwise numerical error in $G_E(4.00 \text{ mm}, t)$ is no more than 0.800% of the peak

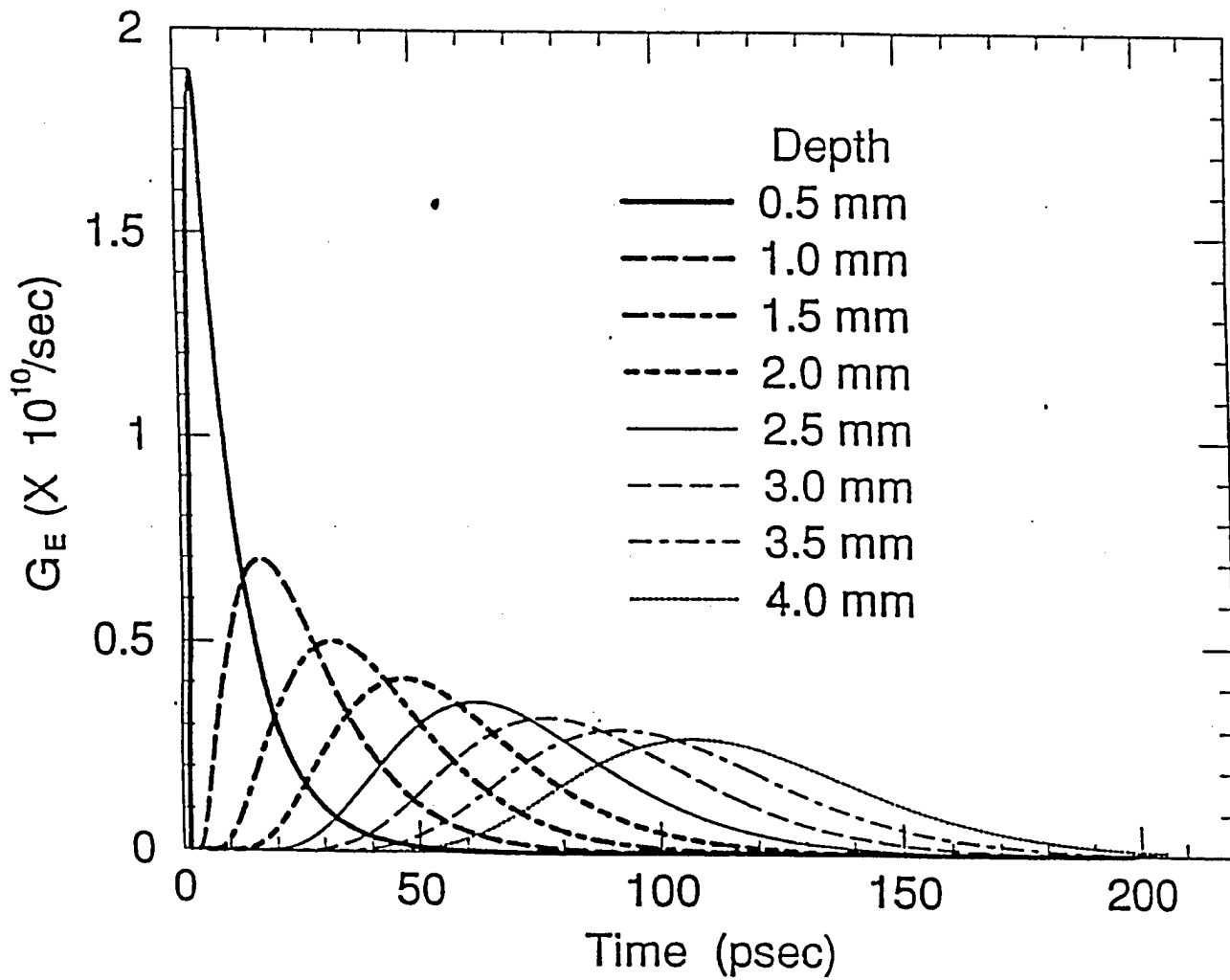


Fig. 1. The time dependence of the Green function $G_E(z, t)$ for water at several depths z .

value of $|G_E(4.00 \text{ mm}, t)|$; and (3) For intermediate depths, the relative error in $G_E(z, t)$ decreases monotonically from 1.70% at $z = 0.500 \text{ mm}$ to 0.800% at $z = 4.00 \text{ mm}$. The closed-form expression for $G_E(0, t)$ is exact.⁹

We will use the following three norms:

$$\begin{aligned} \|h(z, \cdot)\|_1 &= \int_0^\infty dt |h(z, t)| \\ \|h(z, \cdot)\|_2 &= \left(\int_0^\infty dt |h(z, t)|^2 \right)^{1/2} \\ \|h(z, \cdot)\|_\infty &= \text{least upper bound of } |h(z, \cdot)|, \end{aligned} \quad (2.3)$$

where, for each depth z , the least upper bound $\|h(z, \cdot)\|_\infty$ is evaluated with respect to t . Then, for each depth z from 0.500 mm through 4.00 mm,

$$\|E(z, \cdot)\|_\infty \leq \|f(\cdot)\|_\infty \exp \left(\frac{-z}{6.15 \times 10^{-5} \text{ m}} \right) + \min \left[\begin{array}{l} (0.202) \|f(\cdot)\|_\infty, \\ F_1(z) \|f(\cdot)\|_2, \\ F_2(z) \|f(\cdot)\|_1 \end{array} \right], \quad (2.4)$$

regardless of the detailed nature of the incident electric field $f(t)$. The right side of (2.4) is easily computed, given the functions $F_1(z) = \|G_E(z, \cdot)\|_2$ and $F_2(z) = \|G_E(z, \cdot)\|_\infty$, which are graphed in Fig. 2. Inequality (2.4) defines upper bounds on the peak amplitudes of $E(z, \cdot)$. This inequality, and all of our other Green-function results, are validated numerically in Subsection 3B. The upper bound on the right side of (2.4) is almost attained in one of the numerical validations. In that sense, the upper bound is sharp.

We will now show how relation (2.4) could be used in a safety standard for the peak amplitudes of internal electric fields. Suppose, for this hypothetical example, that it has been determined that peak electric fields must be no greater than 0.200 V/m at depths greater than 1.00 mm, and no greater than 0.150 V/m at depths greater than 3.00 mm. That hypothetical internal-field standard is translated, using (2.4) and Fig. 2, into a more easily regulated standard on incident electric fields $f(t)$. The easily regulated standard is

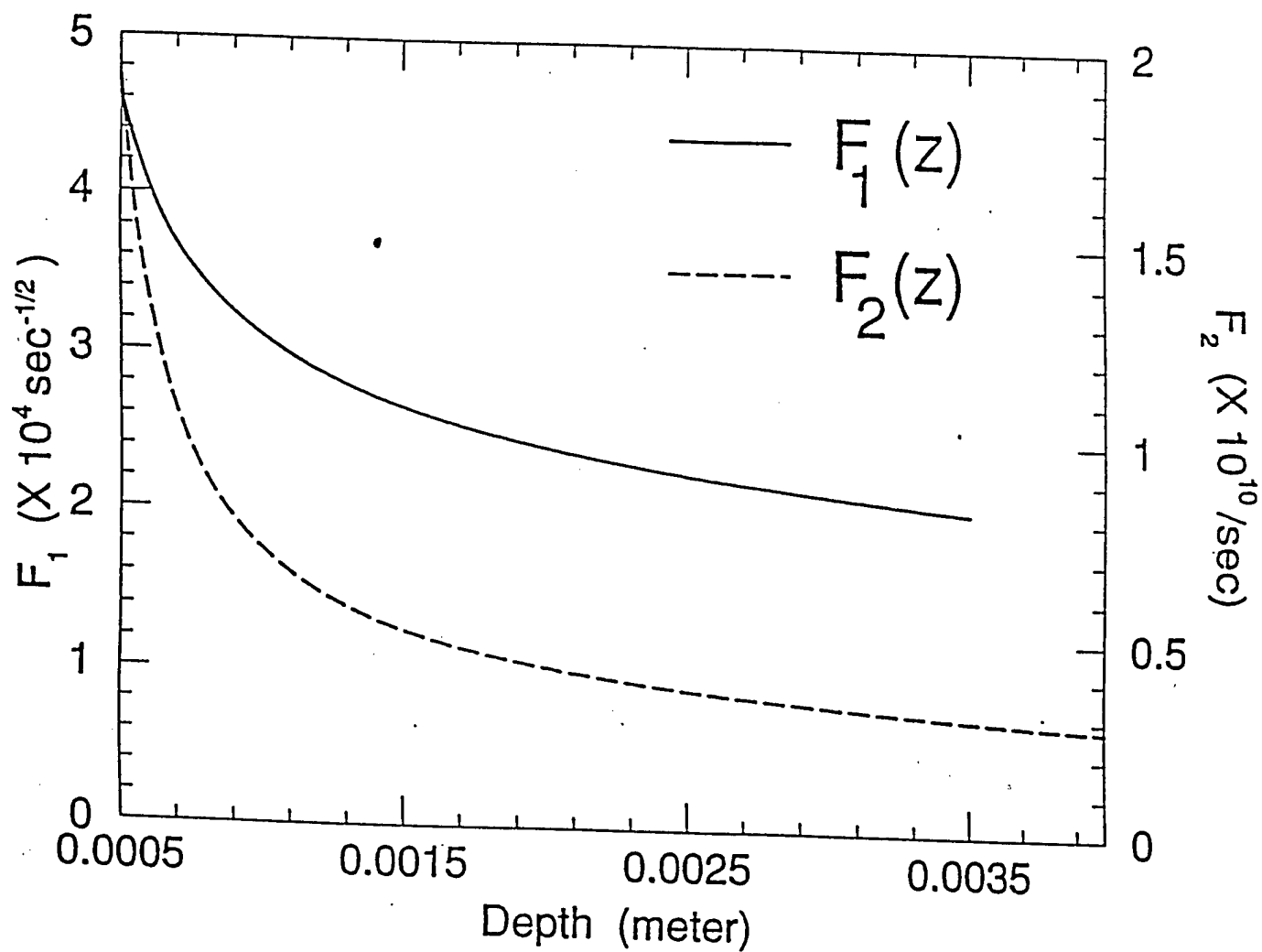


Fig. 2. The L_2 norm $F_1(z)$ and the L_∞ norm $F_2(z)$ of the Green function $G_E(z, \cdot)$ for water. These norms and Eqn. (2.4) reduce the upper-bound computations to a calculator exercise.

- (1) Peak value of $|f(t)| \leq 0.740 \text{ V/m}$ or
- (2) $\left[\text{Peak value of } |f(t)| \leq 40,000 \text{ V/m and } \int_0^\infty dt |f(t)|^2 \leq 4.00 \times 10^{-11} \text{ V}^2\text{s/m}^2 \right]$ or
- (3) $\left[\text{Peak value of } |f(t)| \leq 50,000 \text{ V/m and } \int_0^\infty dt |f(t)| \leq 2.80 \times 10^{-11} \text{ Vs/m} \right]$.
- (2.5)

By reading the two graphs in Fig. 2 and using a calculator, one can use (2.4) to show that any incident field that satisfies item (1) or item (2) or item (3) of (2.5) is guaranteed to produce internal fields that comply with the hypothetical internal-field standard, regardless of all other details of $f(t)$.

Upper bounds also exist for quantities that resemble power densities.¹⁰ In particular, for any incident field $f(t)$ and for each depth z from 0.500 mm through 4.00 mm, the power-density-type term¹⁰ $[\|E(z, \cdot)\|_2]^2 = \int_0^\infty dt |E(z, t)|^2$ satisfies

$$\int_0^\infty dt |E(z, t)|^2 \leq \left\{ \|f(\cdot)\|_2 \exp\left(\frac{-z}{6.15 \times 10^{-5} \text{ m}}\right) + \min \left[\frac{(0.202) \|f(\cdot)\|_2}{F_1(z) \|f(\cdot)\|_1} \right] \right\}^2.$$

(2.6)

Subsection 3B numerically validates the inequality in (2.6), showing that the upper bound on the right side of (2.6) is almost attained in at least one case.

We will now show how the upper bounds in (2.6) could be used in a safety standard for an power-density-type quantity related to internal electric fields. Suppose, for this hypothetical example, that it has been determined that the power-density-type quantity $\int_0^\infty dt |E(z, t)|^2$ must be no greater than $1.50 \times 10^{-12} \text{ V}^2\text{s/m}^2$ at depths greater than 1.00 mm, and no greater than $1.00 \times 10^{-12} \text{ V}^2\text{s/m}^2$ at depths greater than 3.00 mm. Equation (2.6) and Fig. 2 translate this hypothetical standard for internal fields into a more easily regulated standard on incident electric fields $f(t)$:

$$\begin{aligned}
(1) \quad & \int_0^\infty dt |f(t)|^2 \leq 2.40 \times 10^{-11} \text{ V}^2\text{s/m}^2 \quad \text{or} \\
(2) \quad & \left[\int_0^\infty dt |f(t)|^2 \leq 36.0 \text{ V}^2\text{s/m}^2 \quad \text{and} \quad \int_0^\infty dt |f(t)| \leq 3.90 \times 10^{-11} \text{ Vs/m} \right].
\end{aligned}
\tag{2.7}$$

Subsection 3B shows that some pulses almost attain the upper bounds in (2.6), which was used to obtain (2.7).

The upper-bound concepts in (2.4) and (2.6) are easily extended to magnetic fields and their time derivatives, and to oblique incidence. Subsection 3B has numerical results for all of those extensions. One can see there that making the angle of incidence more oblique will decrease the penetration into the medium of power-density-type quantities and also peak electric and magnetic fields. A related closed-form, modified-Bessel-function expression for the oblique-incidence reflection kernel $R^\theta(t) = G_{E,\theta}(0,t)$ is given in (3.12).

We will now state some Green-function results concerning wave speeds. These results are derived in Subsection 3B. For simplicity, the results are stated for normal incidence. Our first conclusion is that the main bulk of an electromagnetic pulse travels through water with speed c_0 for 0.3 mm, and then slows until, for all depths beyond 0.7 mm, the pulse travels with the constant speed $c_0/9.0$. That behavior contrasts with the wavefront speed, which is mathematically well defined but is not always observable in a laboratory. The wavefront speed is precisely c_0 for all depths.¹¹ Section 4 discusses various Debye models that are consistent, to within about 10%, with the band-limited water data² used here. The large-depth speeds (all $\approx c_0/9.0$) for those Debye models vary by only about 10%. The shallow-depth speed and the wavefront speed of any Debye model, however, are both equal to $c_0 = 1/\sqrt{\mu_0\epsilon_\infty}$. The shallow-depth and wavefront speeds, consequently, change considerably as one varies the Debye parameter ϵ_∞ from 1.00 through 10.0, as described in Section 4. Therefore, a measurement of the wavefront speed or the shallow-depth speed would determine the Debye parameter ϵ_∞ .

We conclude with some Green-function results concerning short-pulse and long-pulse approximations. The propagation of any finite-valued incident electric

pulse $f(t)$ is given simply by (2.2) and Fig. 1. We get additional insight by considering approximations for what we will call elemental pulses f_e : An element $f_e(t)$ is zero except on a single time interval, during which it is either strictly negative or strictly positive. For instance, a square pulse is an element, but a one-cycle sinusoid is not an element. Elements are important because any incident pulse f is a sum of positive-valued elements and negative-valued elements. If the duration of an element $f_e(t)$ is much briefer than 30 psec, then the propagated pulse element is approximately $\|f_e(\cdot)\|_1 G_E(z, t)$ (see Fig. 1) for all depths greater than 0.7 mm. If the duration of an element $f_e(t)$ is much longer than 50 psec, then the propagated pulse element is approximately $0.2f_e[t - 9.0(z - 1 \text{ mm})/c + 17 \text{ psec}] = 0.2f_e(t - 9.0z/c - 13 \text{ psec})$ for all depths from 1 mm through the depth at which the duration of $G_E(z, t)$ becomes comparable to the duration of $f_e(t)$. These approximations are derived in Subsection 3B.

3. DERIVATIONS

A. PDEs

To extract from (2.1) the equation describing the early-time evolution (in the “skin-layer”) of the response we set everywhere in (2.1) $\partial_\xi \sim -c_o \partial_z$ except in the operator $\partial_\xi + c_o \partial_z$ since it expresses the propagation of the high-order waves. Any other terms in the resulting equation will describe the effect of the lower-order waves. The main disturbance for early times is modeled by

$$(\partial_\xi + c_o \partial_z)E + \frac{\beta}{\tau} \frac{c_o^2 - c_1^2}{2c_o^2} E = 0; \quad z < c_o \tau, \quad (3.1)$$

subject to the boundary condition $E(0, \xi) = g(\xi)$. The solution of (3.1) is

$$E(z, \xi) = g\left(\xi - \frac{z}{c_o}\right) \exp \left[- \left(\frac{\epsilon_s/\epsilon_\infty - 1}{2 \cos^2 \phi_{inc}} \right) \left(\frac{z}{c_o \tau} \right) \right]. \quad (3.2)$$

We see that the response decays exponentially in a thin region of depth $z \sim O(c_o \tau)$, where the speed of propagation is c_o . Note that the decay constant is inversely proportional to $\cos^2 \phi_{inc}$ thus normal incidence will result in the greatest amplitude in the medium. To describe the evolution of the lower-order waves, which travel with speed c_1 , we set in (2.1) $\partial_\xi \sim -c_1 \partial_z$ except in the operator $\partial_\xi + c_1 \partial_z$ which expresses the hyperbolic nature of the lower-order waves. The main disturbance is now modeled by

$$(\partial_\xi + c_1 \partial_z)E = \frac{\tau}{\beta} \frac{c_o^2 - c_1^2}{2} \partial_z^2 E; \quad z > c_o \tau. \quad (3.3)$$

The boundary condition is approximately $E(z_o, \xi') = h(\xi')$, where z_o is the depth after which (3.1) no longer applies, ξ' is the time with origin at z_o/c_o (the time it takes for the pulse to reach z_o in the “skin-depth”), and $h(\xi')$ represents (3.2) evaluated at z_o . Equation (3.3) is an advection-diffusion equation, and describes the response after a depth of $O(c_o \tau)$ m. The peak of the response is on the sub-characteristic ray $z_s = c_1 \xi'$. The solution is very easily obtained from the solution of the diffusion equation. It is¹²

$$E(z, \xi') = \sqrt{\frac{\beta}{2\pi\tau(c_o^2 - c_1^2)}} z \times \int_0^{\xi'} d\kappa \frac{h(\kappa)}{(\xi' - \kappa)^{\frac{3}{2}}} \exp \left(- \left[\frac{\beta}{2\tau(c_o^2 - c_1^2)} \right] \left\{ \frac{[z - c_1(\xi' - \kappa)]^2}{\xi' - \kappa} \right\} \right). \quad (3.4)$$

Various techniques can be used to estimate the integral in (3.4) since β/τ is large. Here we are interested only in the primary behavior of E as a function of depth. For $\frac{\beta}{\tau} \gg 1$ the response is

$$E^\delta(z, \xi') = h(0) \sqrt{\frac{\beta}{2\pi\tau(c_o^2 - c_1^2)}} \frac{z}{\xi'^{\frac{3}{2}}} \exp \left\{ - \left[\frac{\beta}{2\tau(c_o^2 - c_1^2)} \right] \left[\frac{(z - c_1\xi')^2}{\xi'} \right] \right\}. \quad (3.5)$$

On $z_s = c_1\xi'$ we find that $\max\{E^\delta\} \sim 1/\sqrt{z}$, or $\sim 1/\sqrt{\xi'}$. This is verified with the numerical experiments in Section 4.

B. Green Functions

This subsection derives our Green-function results in the order in which they are described in Subsection 2B. Equation (2.2), for instance, is a Green-function representation. These Green functions have become a standard technique in computational electromagnetics. They were first developed for non-dispersive media,¹³ and were then used to compute fields in dispersive media.¹⁴ That dispersive-medium work has not yet been published, owing to the death of R. Krueger, but generalizations are available.¹⁵⁻¹⁷ The Green function programs used in the present paper were developed by the authors of Ref. 16, along the lines of Appendix A of that paper.

The L_∞ and L_2 norms in (2.3) have special physical significance. The L_2 norm is important because $(c\epsilon_0/2)(\|E\|_2)^2$ is the power density, whose mks units are Watt/m², of an electric pulse in free space.¹⁰ Consequently, we will focus on the peak-value ($p = \infty$) and power-density ($p = 2$) cases of the inequalities

$$\|E(z, \cdot)\|_p \leq e^{-az} \|f(\cdot)\|_p + \|G(z, \cdot)\|_r \|f(\cdot)\|_q, \quad (3.6)$$

which are obtained by applying the Young theorem¹⁸ to (2.2), and for which $a = 1.63 \times 10^4 \text{ m}^{-1}$. In particular, although (3.6) is valid whenever $1 \leq p, q, r \leq \infty$ satisfy $r^{-1} = p^{-1} + q^{-1} - 1$, we are most interested in the cases

$$\|E(z, \cdot)\|_\infty \leq e^{-az} \|f(\cdot)\|_\infty + \min \begin{bmatrix} \|G_E(z, \cdot)\|_1 \|f(\cdot)\|_\infty, \\ \|G_E(z, \cdot)\|_2 \|f(\cdot)\|_2, \\ \|G_E(z, \cdot)\|_\infty \|f(\cdot)\|_1 \end{bmatrix} \quad (3.7)$$

and

$$[\|E(z, \cdot)\|_2]^2 \leq \left\{ e^{-az} \|f(\cdot)\|_2 + \min \begin{bmatrix} \|G_E(z, \cdot)\|_1 \|f(\cdot)\|_2, \\ \|G_E(z, \cdot)\|_2 \|f(\cdot)\|_1 \end{bmatrix} \right\}^2. \quad (3.8)$$

In numerical computations for water, $\|G_E(z, \cdot)\|_1$ was observed to decrease slowly and monotonically from 0.2019 at 0.5 mm to 0.2014 at 3.5 mm. It is as if, for those depths in water, the advection-diffusion equation (3.3) were approximated by a heat equation and $G_E(z, t)$, which is positive valued for depths beyond 0.5 mm, were analogous to a temperature distribution whose total conserved heat is proportional

to $\|G_E(z, \cdot)\|_1$. Equations (3.6)–(3.8), the almost-constant nature of $\|G_E(z, \cdot)\|_1$, and numerical Green-function computations produced the results in (2.4)–(2.7).

We now consider five numerical examples that validate the inequalities in (2.4). We will see that the minimum upper bounds in (2.4) are almost attained for some incident pulses. For these five examples, we choose the following hypothetical restrictions on the incident electric pulses $f(t)$:

$$\begin{aligned} \|f(\cdot)\|_\infty &\leq 1.00 \text{ V/m and} \\ \|f(\cdot)\|_2 &\leq 6.32 \times 10^{-6} \text{ Vs}^{1/2}/\text{m and} \\ \|f(\cdot)\|_1 &\leq 4.00 \times 10^{-11} \text{ Vs/m.} \end{aligned} \tag{3.9}$$

Then (2.4) shows that any incident pulse f that satisfies (3.9) will produce an internal field whose peak amplitude satisfies

$$\|E(z, \cdot)\|_\infty \leq \left[\exp\left(\frac{-z}{6.15 \times 10^{-5} \text{ m}}\right) \text{ V/m} \right] + \min \left[\begin{array}{c} 0.202 \text{ V/m,} \\ (6.32 \times 10^{-6} \text{ Vs}^{1/2}/\text{m}) F_1(z), \\ (4.00 \times 10^{-11} \text{ Vs/m}) F_2(z) \end{array} \right], \tag{3.10}$$

where $F_1(z)$ and $F_2(z)$ are graphed in Fig. 2. Each sum of the exponential in (3.10) and a term from the “min” clause of (3.10) yields one of the three top-most, boldface curves in Fig. 3. Relation (3.10) guarantees that the depth-dependent peak amplitudes of $E(z, \cdot)$ are less than the minimum of the three boldface upper-bound graphs. That prediction was tested using five incident pulses f that comply with (3.9). Those incident pulses are: (1) a 40-psec-duration square pulse with 1-V/m amplitude; (2) the absolute value $f_2(t) = |f_4(t)|$ of the 4-cycle, 80-GHz sinusoid in item 4 below; (3) the absolute value $f_3(t) = |f_5(t)|$ of the 1-cycle, 80-GHz sinusoid in item 5 below; (4) a 4-cycle 80-GHz sinusoid with 1-V/m amplitude; and (5) a 1-cycle 80-GHz sinusoid with 1-V/m amplitude. The norms of the pulses, which are tabulated below, all satisfy (3.9).

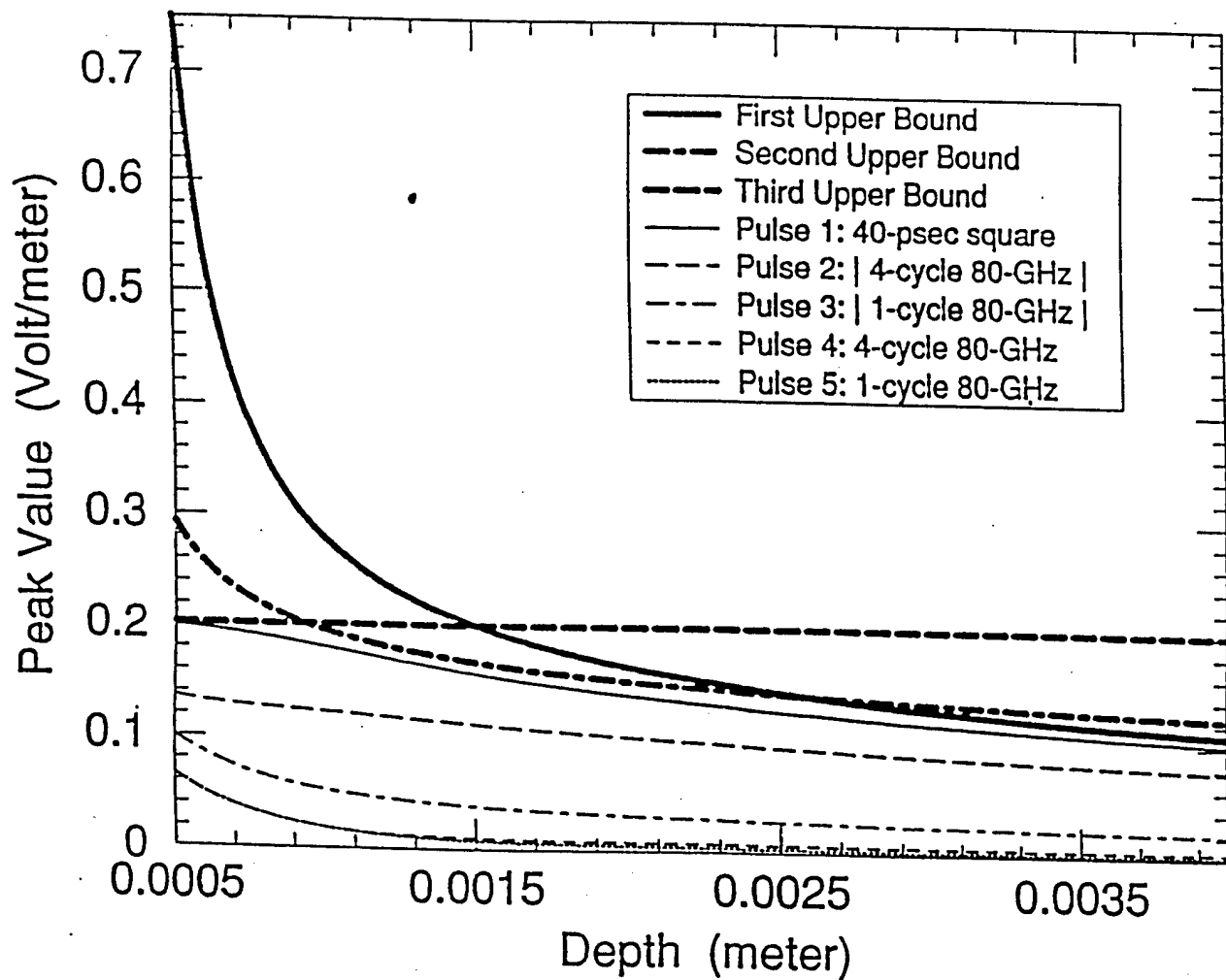


Fig. 3. Five numerical validations of the upper-bound concept for the depth-dependent peak amplitudes of $E(z, \cdot)$. The boldface curves are upper bounds from relation (3.10).

Table 1. Five incident pulses that satisfy the conditions in (3.9). The first incident pulse is 1 V/m for $0 \leq t \leq 40$ psec, and it is 0 for all other times. The second pulse is the absolute value of $(1\text{V/m}) \sin[2\pi t/(8 \times 10^{10}\text{s})]$ for $0 \leq t \leq 50$ psec, and it is 0 for all other times.

Example	Duration	Type	$\ \cdot\ _\infty$ (V/m)	$\ \cdot\ _2$ (Vs ^{1/2} /m)	$\ \cdot\ _1$ (Vs/m)
1	40-psec	square pulse	1.00	6.32×10^{-6}	4.00×10^{-11}
2	4 cycles	80-GHz sine	1.00	5.00×10^{-6}	3.18×10^{-11}
3	1 cycle	80-GHz sine	1.00	2.50×10^{-6}	7.96×10^{-12}
4	4 cycles	80-GHz sine	1.00	5.00×10^{-6}	3.18×10^{-11}
5	1 cycle	80-GHz sine	1.00	2.50×10^{-6}	7.96×10^{-12}

The peak amplitudes of the five internal fields $E(z, \cdot)$, corresponding to the above-tabulated incident fields, are also graphed in Fig. 3; the curves for Examples 4 and 5 almost overlap. Those peak amplitudes are all less than the (boldface) upper bounds described earlier. The five examples, therefore, numerically validate the upper bound concept in (2.4). Fig. 3 also shows that the upper bounds are sharp in the sense that the peak amplitude of one pulse (Example 1) almost attains the minimum upper bound. That example involves a pulse with a nonzero DC-component¹⁹⁻²¹ $\int_0^\infty dt f(t)$. It makes intuitive sense that the presence of a DC component in a pulse would tend to diminish the attenuation of the pulse in any medium, as an elementary analysis²² affirms for a non-Debye medium.

Having just validated the upper-bound concept (2.4) for peaks, we now validate (2.6): The two top-most, boldface curves in Fig. 4 correspond to the upper bounds $(e^{-az}\|f\|_2 + \|G_E\|_1\|f\|_2)^2$ and $(e^{-az}\|f\|_2 + \|G_E\|_2\|f\|_1)^2$ in (2.6), subject to the hypothetical restriction (3.9). The other five curves represent the power-density-type quantities $\|E_x(z, \cdot)\|_2^2$ produced by the five incident fields in Table 1. We

see that the field produced by Example 1 of Table 1 almost attains the minimum upper bound in Fig. 4. This completes our validation of the upper-bound concepts.

As explained above (2.1), oblique incidence is taken into account using a simple, widely-known transformation of variables. Using the transformation, we obtain numerical results for 45°-incident electric fields $f[t - (x + z)/(\sqrt{2}c)]$. In water ($z \geq 0$) the y component of the electric field is

$$E(x, z, t) = E\left(0, z, t - \frac{x}{\sqrt{2}c}\right)$$

$$E(0, z, t) = \exp\left(\frac{-z}{4.35 \times 10^{-5}\text{m}}\right) f\left(t - \frac{z}{\sqrt{2}c}\right) + \int_0^{t-z/(\sqrt{2}c)} ds f(s) G_{E,45^\circ}(z, t-s). \quad (3.11)$$

The function $G_{E,45^\circ}(z, t)$ is graphed in Fig. 5 for several depths $z > 0$. The numerical errors in Fig. 5 were quantitatively estimated using the method of Appendix A. The results are: (1) For each depth z , from 0.160 mm through 2.88 mm, the error in the computed values of $G_{E,45^\circ}(z, t)$ are no more than 3.19% of the peak value, with respect to time, of the actual values $|G_E(z, t)|$; and (2) The relative errors decrease, but not necessarily monotonically, from 3.19% at 0.160 mm to 2.07% at 2.88 mm. At the boundary $z = 0$ and for all $t > 0$, $G_{E,45^\circ}(0, t) = -t^{-1} \exp[-t/(1.01 \times 10^{-13}\text{s})] I_1[t/(1.03 \times 10^{-13}\text{s})]$, where I_1 is the modified Bessel function of the first kind. More generally, the oblique-incidence transformation and Ref. 9 imply, for all $t > 0$, that

$$R^\theta(t) = G_{E,\theta}(0, t) = \frac{-1}{t} \exp\left[-\left(b + \frac{a}{2\varepsilon_\infty \cos^2 \theta}\right)t\right] I_1\left(\frac{at}{2\varepsilon_\infty \cos^2 \theta}\right). \quad (3.12)$$

That exact result uses the modified Bessel function of the first kind to represent the reflections in the air-filled half-space ($z < 0$) that are caused by waves that are incident obliquely on the Debye half-space ($z \geq 0$) defined by

$$D(z, t) = \begin{cases} \varepsilon_\infty \varepsilon_0 E(z, t), & z < 0 \\ \varepsilon_\infty \varepsilon_0 E(z, t) + a\varepsilon_0 \int_0^t ds e^{-b(t-s)} E(z, s), & z \geq 0 \end{cases} \quad (3.13)$$

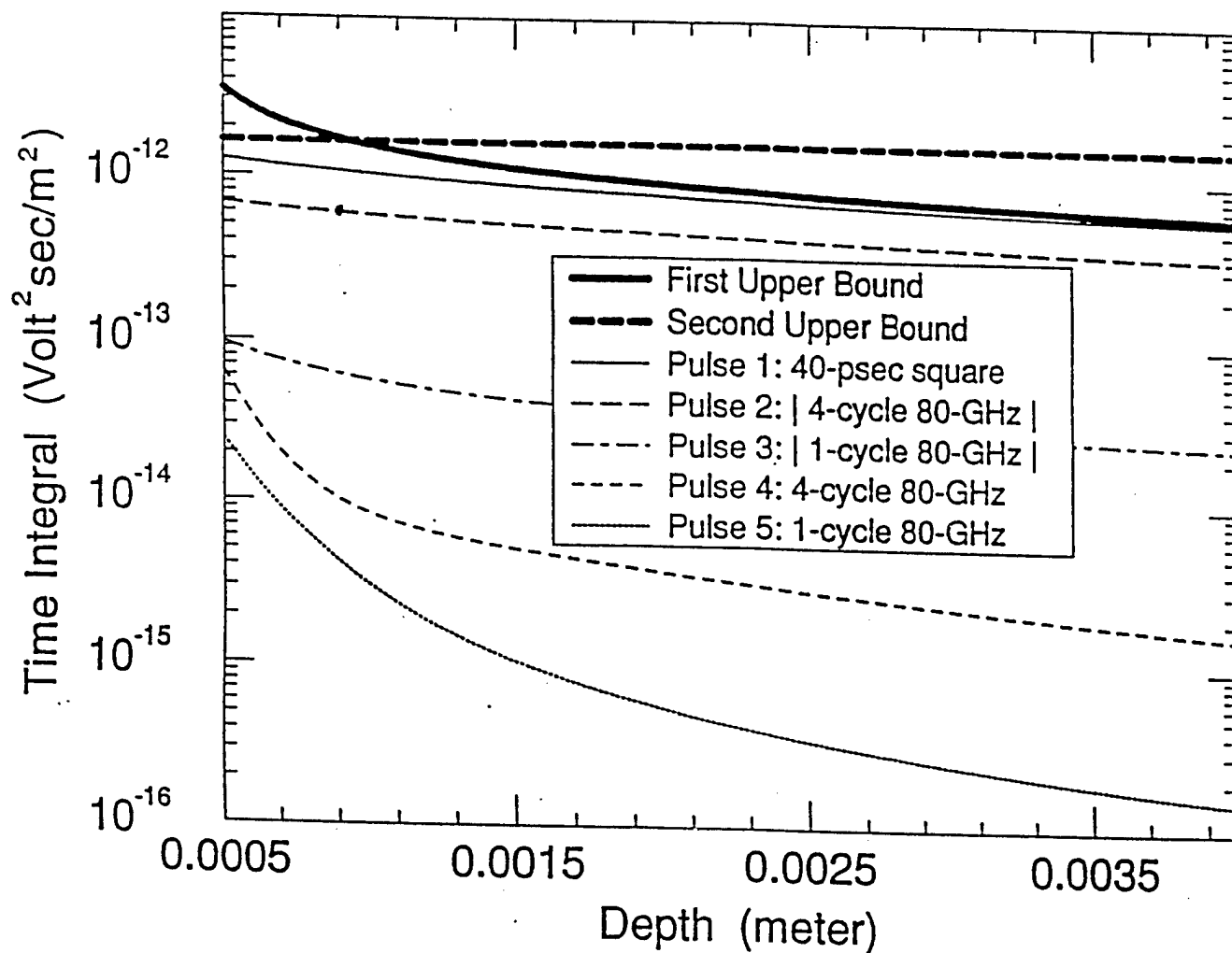


Fig. 4. Five numerical validations of the upper-bound concept for the power-density-type time integral $\int_0^\infty dt |E(z,t)|^2$. The boldface upper bounds are from relation (2.6).

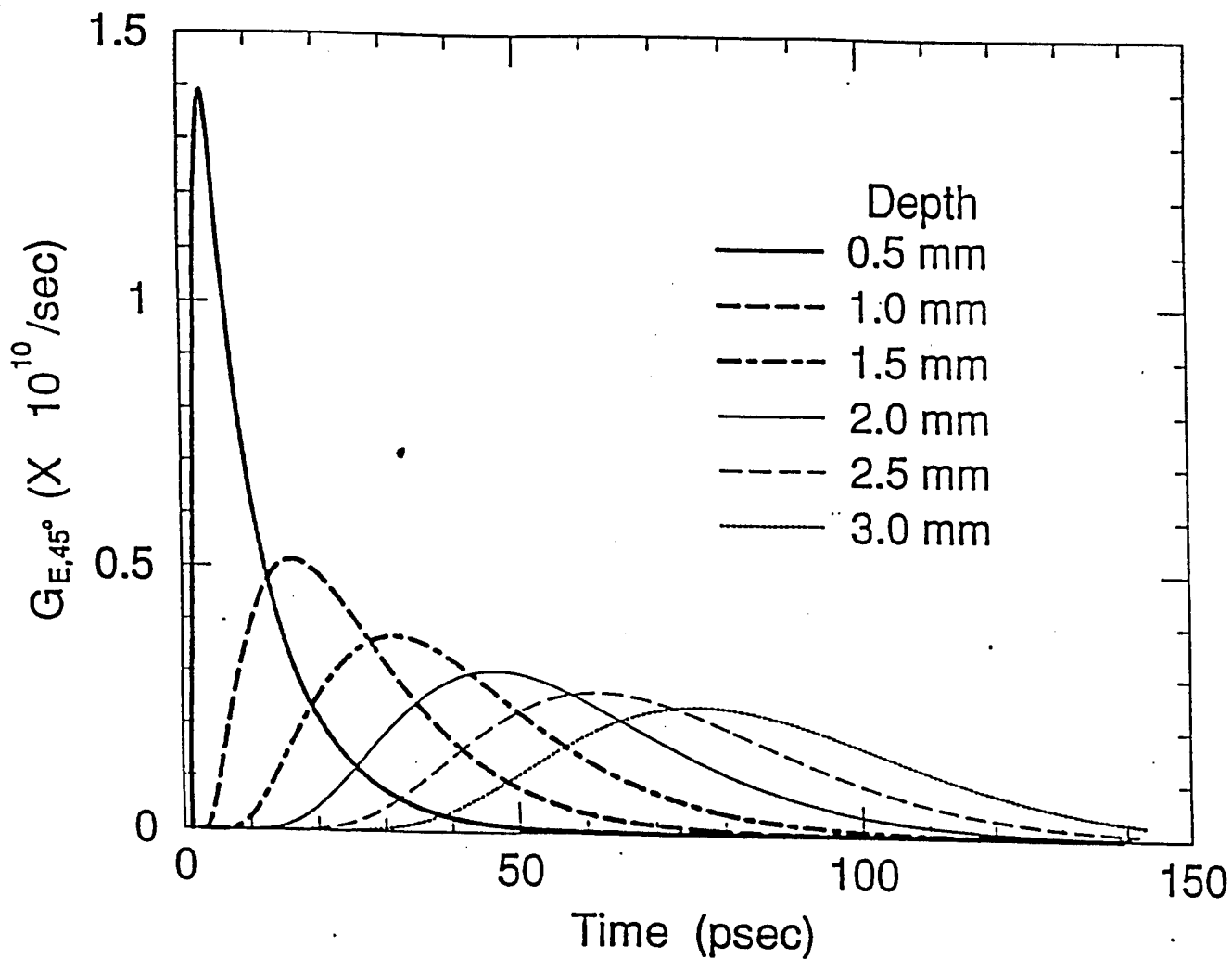


Fig. 5. The time dependence of the Green function $G_{E,45^\circ}(z,t)$ for several depths z . This Green function is used for pulses that are incident on water at an angle of 45° .

In particular, the reflected field is exactly $\int_0^t ds f(s) R^\theta(t-s)$ for any incident field f . Equation (3.12) was used numerically to validate the $z = 0$ boundary values of the oblique-incidence Green-function computations that yielded Figs. 5, 6 and 8. Equation (3.12) was also used to validate, at $z = 0$, the previous percentage-error estimates for oblique incidence. At $z = 0$, the estimated relative error was 1.91%; the true relative error was 1.87%.

Applying the Young-theorem result (3.6) to the oblique-incidence representation (3.11) yields obvious oblique-incidence generalizations of the upper-bound results (2.4)–(2.6); for instance, $\|E(0, z, \cdot)\|_2 \leq \|f(\cdot)\|_2 \exp[-z/(4.35 \times 10^{-5} \text{m})] + \min[\|G_{E,45^\circ}(z, \cdot)\|_1 \|f(\cdot)\|_2, \|G_{E,45^\circ}(z, \cdot)\|_2 \|f(\cdot)\|_1]$. The norms $F_3(z) = \|G_{E,45^\circ}(z, \cdot)\|_2$ and $F_4(z) = \|G_{E,45^\circ}(z, \cdot)\|_\infty$ are graphed in Fig. 6, and $\|G_{E,45^\circ}(z, \cdot)\|_1$ was observed to decrease slowly and monotonically from 0.149 at 0.240 mm to 0.144 at 3.00 mm. We numerically tested these oblique-incidence inequalities using the five pulses in Table 1. The inequalities were validated in each case, and the minimum upper bound was almost attained in the case of a DC-component pulse (Example 1).

We will now substantiate the results in the last two paragraphs of Subsection 2B. The results rely mainly on (2.2) and Fig. 1. Note that the first term on the right side of (2.2) represents a wave that travels with speed c_0 and decays exponentially by a factor of 132 in each 0.300 mm interval. Therefore the convolution term in (2.2) predominates for depths greater than 0.300 mm. The major features, such as the peaks, of the convolution kernel G_E are seen in Fig. 1 to travel more slowly than c_0 for depths greater than 0.500 mm. The peak of $G_E(z, t)$, for instance, is shown in Fig. 7 to travel with speed c_0 for the first 0.300 mm, and then to slow gradually to $c_0/9.0$. (The small non-monotonic feature at shallow depths is a numerical artifact caused by applying the $\max(\cdot)$ function to a peak that is broad.) The numerically determined fast speed c_0 and the slow speed $c_0/9.0$ agree quantitatively with analytical results in Subsection 2A, and also substantiate the results in the next-to-last paragraph of Subsection 2B.

The last paragraph of Subsection 2B concerns elemental pulses $f_e(t)$, which are zero except on a single time interval, during which they are either strictly positive or strictly negative. For example, the Green function $G_E(z, t)$ is an elemental

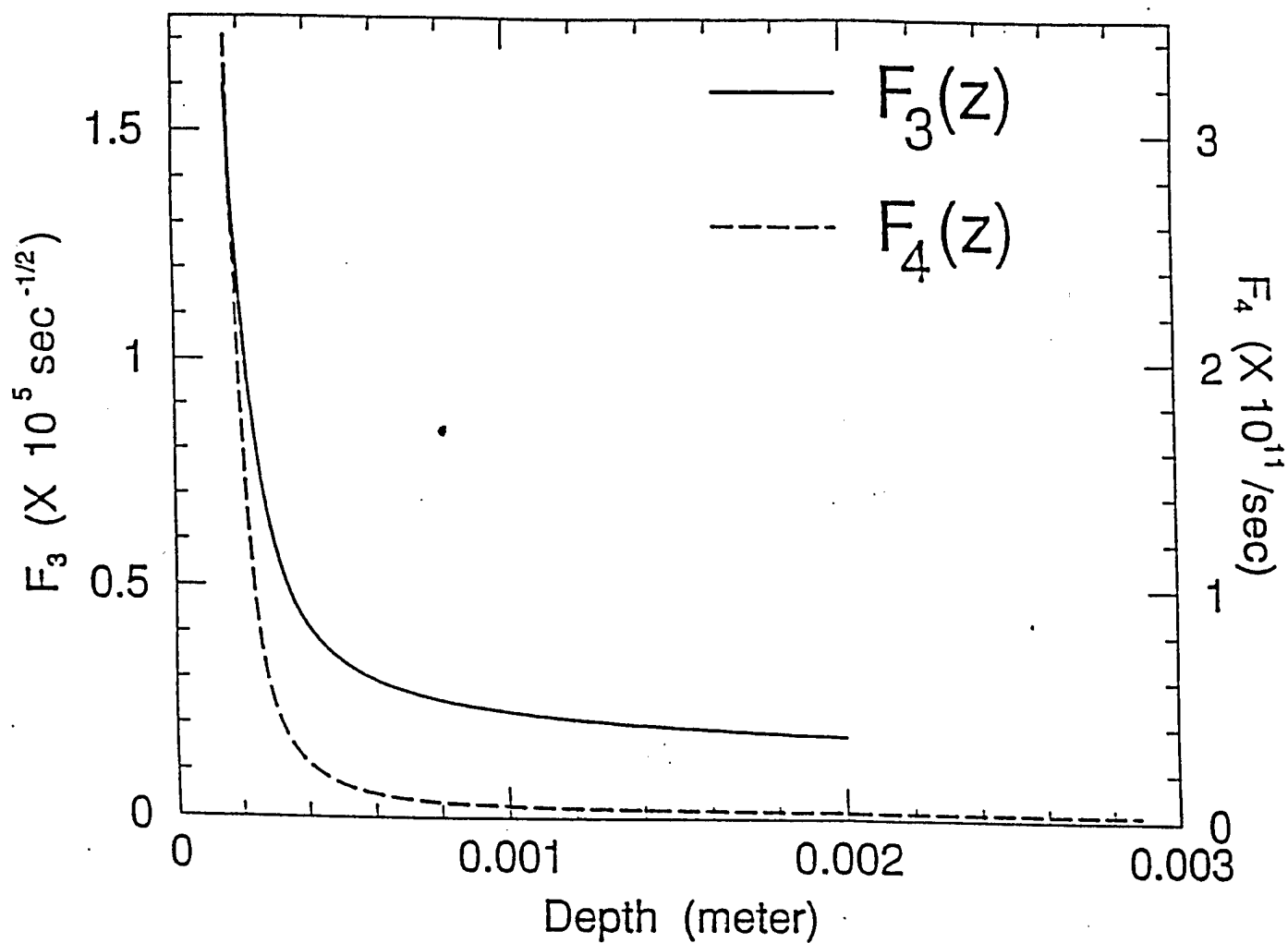


Fig. 6. The L_2 norm $F_3(z)$ and the L_∞ norm $F_4(z)$ of the Green function $G_{E,45}(z, \cdot)$.
The paragraph below (3.13) relates these norms to upper bounds for obliquely incident pulses.

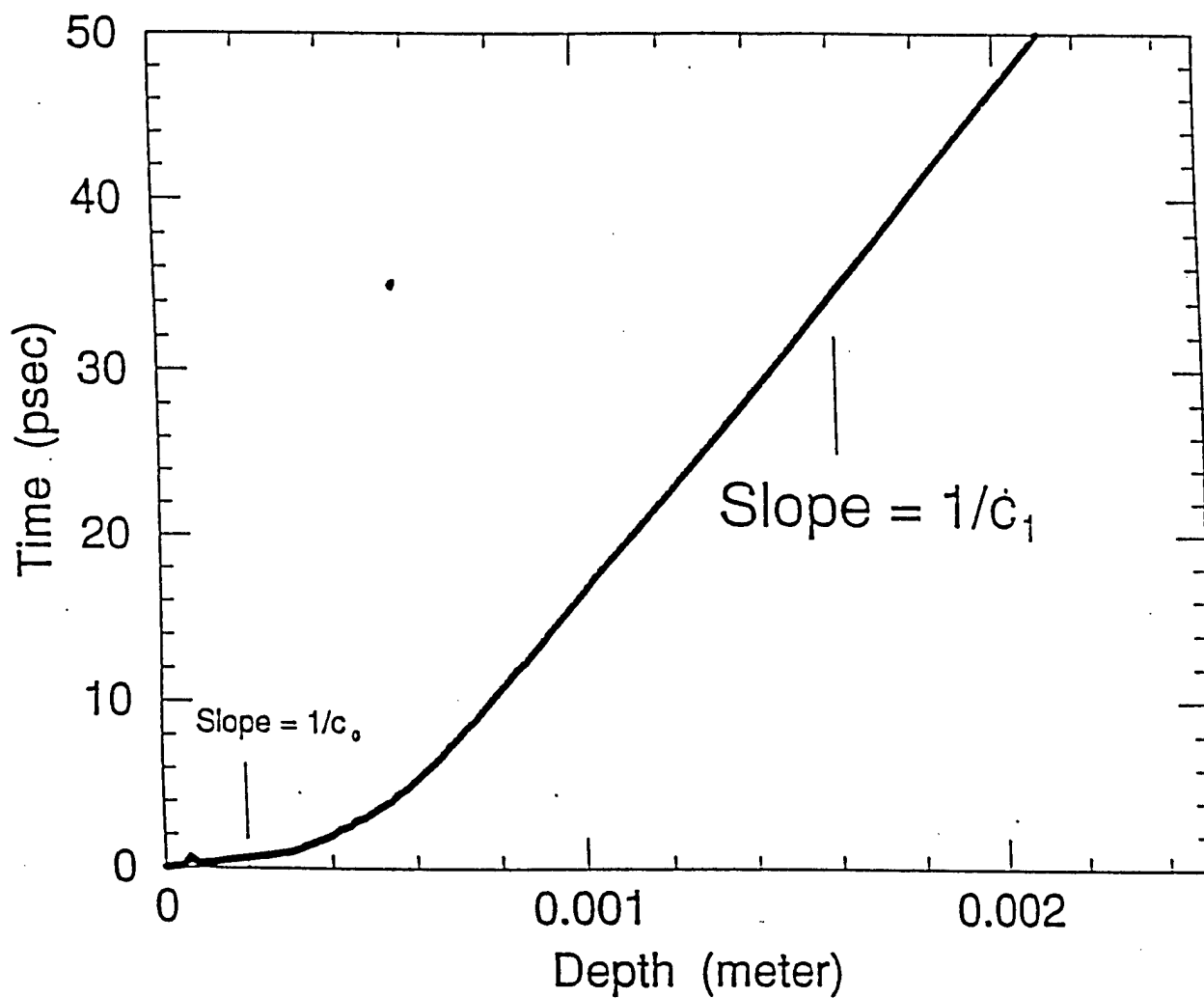


Fig. 7. The time of arrival of the peak of the Green function $G_E(z, t)$ at various depths in water.

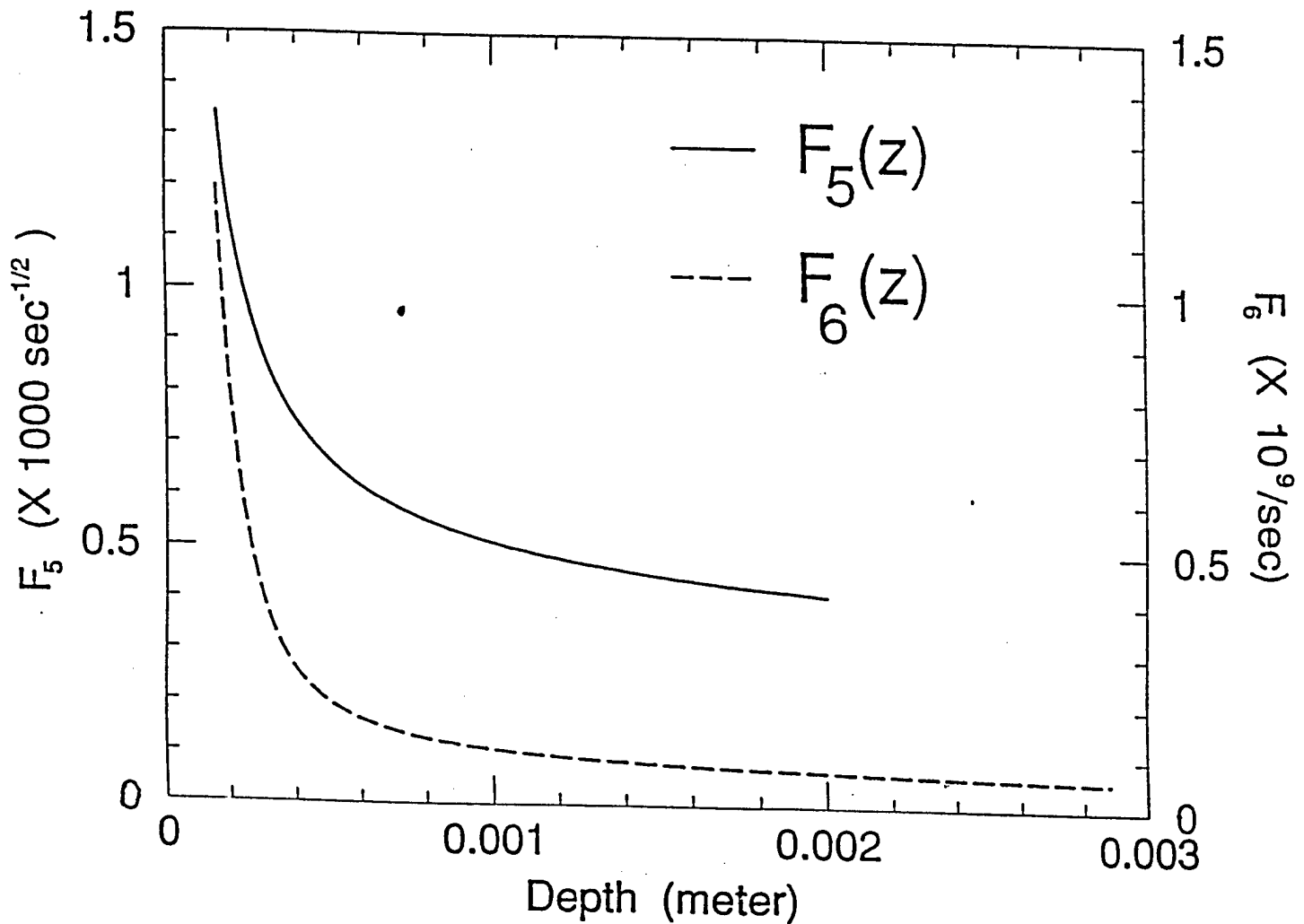


Fig. 8. The L_2 norm $F_5(z)$ and the L_∞ norm $F_6(z)$ of the Green function $G_{H,45^\circ}(z, \cdot)$ for magnetic fields produced by pulses that are incident on water at an angle of 45° . The last paragraph of Section 3 relates this figure to upper bounds for $\partial_t H$.

pulse for all of the depths graphed in Fig. 1. The statements in Subsection 2B that concern the propagation of elemental pulses all rely on the following approximation: If an elemental pulse $f_{\text{brief}}(t)$ is much briefer than an elemental pulse $f_{\text{long}}(t)$, and if $f_{\text{brief}}(t)$ is concentrated at the time t_0 , then $|\int_0^t ds f_{\text{brief}}(t-s)f_{\text{long}}(s)| = |\int_0^t ds f_{\text{long}}(t-s)f_{\text{brief}}(s)| \approx \|f_{\text{brief}}(\cdot)\|_1 |f_{\text{long}}(t-t_0)|$. That approximation is associated with the concept of δ -sequence functions in the elementary theory of Dirac delta functions. We also note that the exponential term in (2.2) quickly becomes negligible because it decays by a factor of 132 across each 0.300 mm interval of depth. These three results—the negligible exponential, the approximation of the convolution, and the observation that G_E is an elemental pulse—together with (2.2) and Fig. 1 yield the brief-pulse result in Subsection 2B, which has the term $\|f_e\|_1 G_E(z, t)$. The long-pulse result in that subsection uses the additional observation, below (3.8), that $\|G_E(z, \cdot)\|_1$ is approximately constant, and the time shift in the long-pulse result in Subsection 2B also relies on Fig. 7 and results from the previous paragraph.

In a final matter we would like to make it clear that we do not know what are the medical effects of isolated pulses. We have, however, developed methods that are flexible enough that they may be useful once the medical effects are known. Although we originally developed the upper-bound method along the lines of peak amplitudes and power densities, following Ref. 5, the method can easily be extended to, say, the time derivative of the magnetic field $H_x(z, t)$. To demonstrate the extension, we computed the Green function G_H in $H_x(0, z, t) = -\left[e^{-az}f(t-z/c_\infty) + \int_{z/c_\infty}^t ds f(t-s)G_H(z, s)\right]/(\mu_0 c_\infty)$ using the methods of Refs. 13–17, and we validated the computation as described in Section 4. The Green-function representation for H_x yields the following analog of (3.6): $\mu_0 c_\infty \|\partial_t H_x(z, \cdot)\|_p \leq e^{-az} \|\partial_t f(\cdot)\|_p + |f(0)| \|G_H(z, \cdot)\|_p + \|G_H(z, \cdot)\|_r \|\partial_t f(\cdot)\|_q$, where $r^{-1} = p^{-1} + q^{-1} - 1$ and $1 \leq p, q, r \leq \infty$. The norms $F_5(z) = \|G_{H,45^\circ}(z, \cdot)\|_2$ and $F_6(z) = \|G_{H,45^\circ}(z, \cdot)\|_\infty$ for that inequality are graphed in Fig. 8 for the 45°-incidence, magnetic Green function $G_{H,45^\circ}$.

4. NUMERICAL VALIDATION AND LABORATORY EXPERIMENTS

We validated the numerical results obtained with the Green's function approach by comparing the computed electric and magnetic fields in a Debye half-space (Section 2, $\phi_{inc} = 0$) to those computed with a finite difference method.²³⁻²⁴ Figure 9 shows electric field time-traces computed at three spatial locations in the half-space due to a $T_p = 40$ -psec square pulse of initial amplitude 1 V/m. We note excellent agreement to within a width of the line over an amplitude scale of 10 orders of magnitude. This indicates a better than 1-part-per-billion agreement. (The small difference increases to two-pen-strokes' width at the shallowest depth, but only after the field itself decreases by a factor one thousand.) Also, the speeds of the first arrival and of the peak of the response can be deduced from this graph. We see that the first arrival occurs with speed $c_o = c$, while the peak of the response arrives with the speed $c_1 = 0.1116c$ as predicted in Section 2. Figure 10 shows a comparison of magnetic fields, computed with the two methods at three depths in the half-space, for a square-modulated sinusoidal pulse of $T_p = 50$ -psec duration and carrier frequency 80 GHz. Again similarly excellent agreement is noted.

Next, we confirm the analytical results presented in Subsection 2A by solving, with the Green's function method, for the impulse response, $f(t - x/c) = \delta(t - x/c)$, of the Debye half-space described there for $\phi_{inc} = 0$ ($\xi = t$). To determine the two speeds predicted by (2.1) the peak of the impulse response was obtained from the simulation results. The temporal versus the spatial location of the peak's occurrence is graphed in Figure 7. The slope of the graph is the reciprocal of the speed of the peak of the response. The relative unimportance of the characteristic $z = c_o t$ (equivalently, the wavefront speed) with respect to the sub-characteristic $z = c_1 t$ is immediately evident. The value of the slope is given in Figure 7 for two ranges of depth. We see that for depths of $O(c_o \tau)$ the response travels with the speed c_o , and then slows down in another $O(c_o \tau)$ interval. This additional interval will be much smaller or altogether absent for band-limited pulses. Eventually, the pulse travels with the speed c_1 for the remainder of the half-space. The diffusive character of the main disturbance in the half-space is exemplified in Figure 11 where the numerically obtained $\max\{E^2\}$ is compared with the analytically predicted behavior $(1/\sqrt{z})$ as a function of depth. The

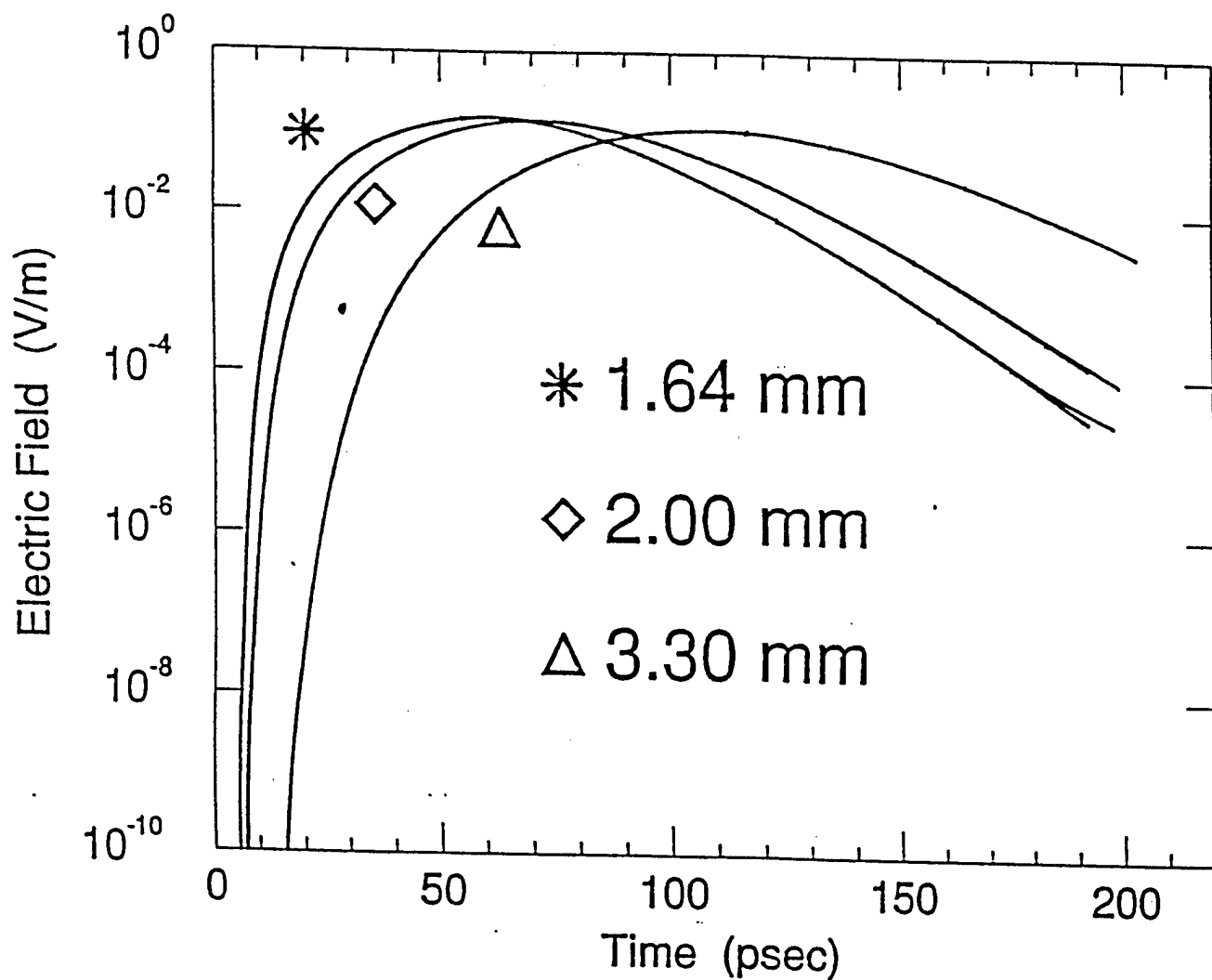


Fig. 9. The electric fields, at three depths in water, that result from a normally incident 40-psec square pulse of 1-V/m amplitude. At the three depths graphed, the fields are precisely 0 until $5.46 \overline{psec}$, $8.20 \overline{psec}$, and $9.60 \overline{psec}$ respectively.

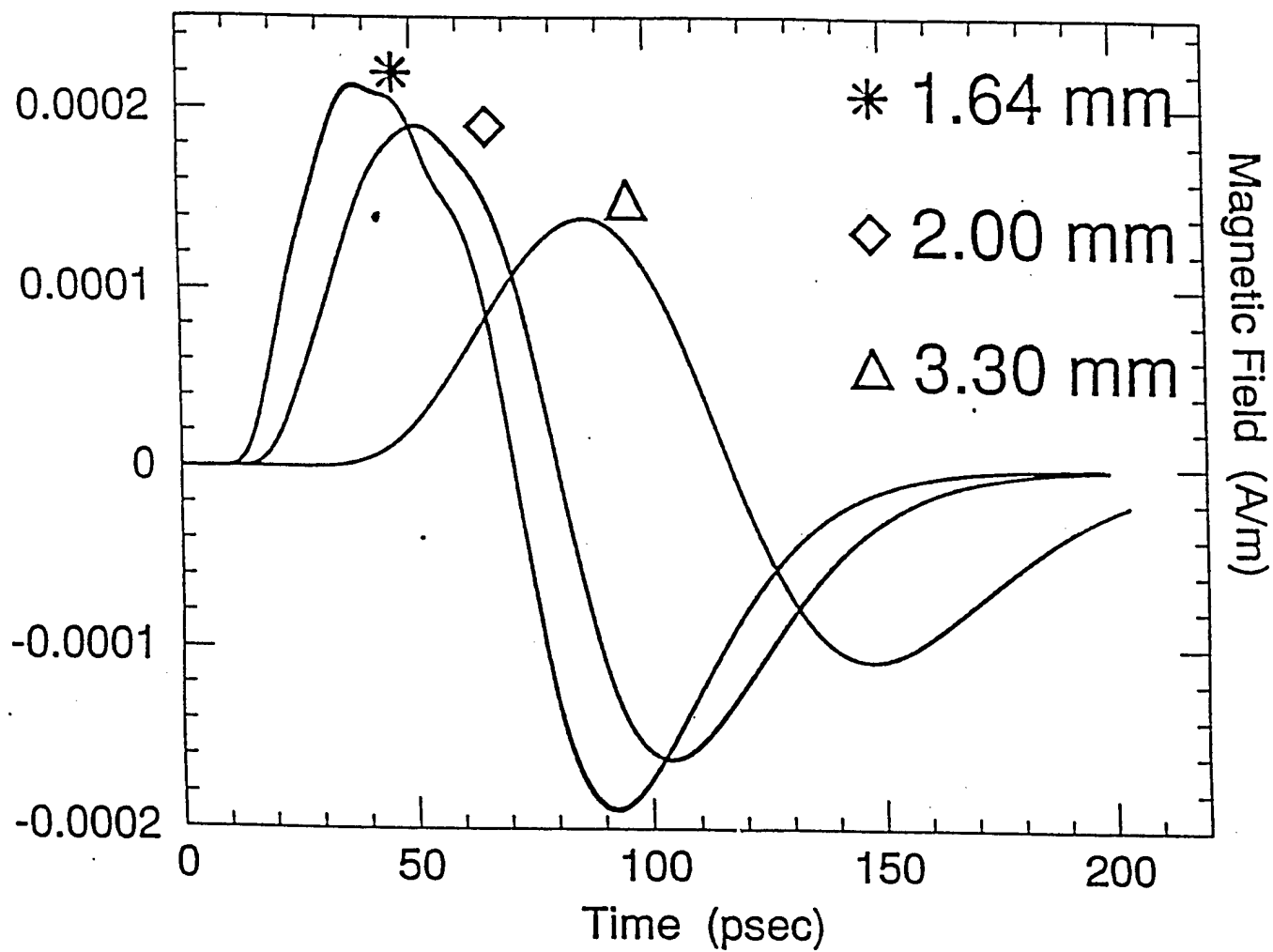


Fig. 10. The magnetic fields that result from a normally incident 4-cycle 1-V/m-amplitude square-modulated sinusoid of 50-psec duration.

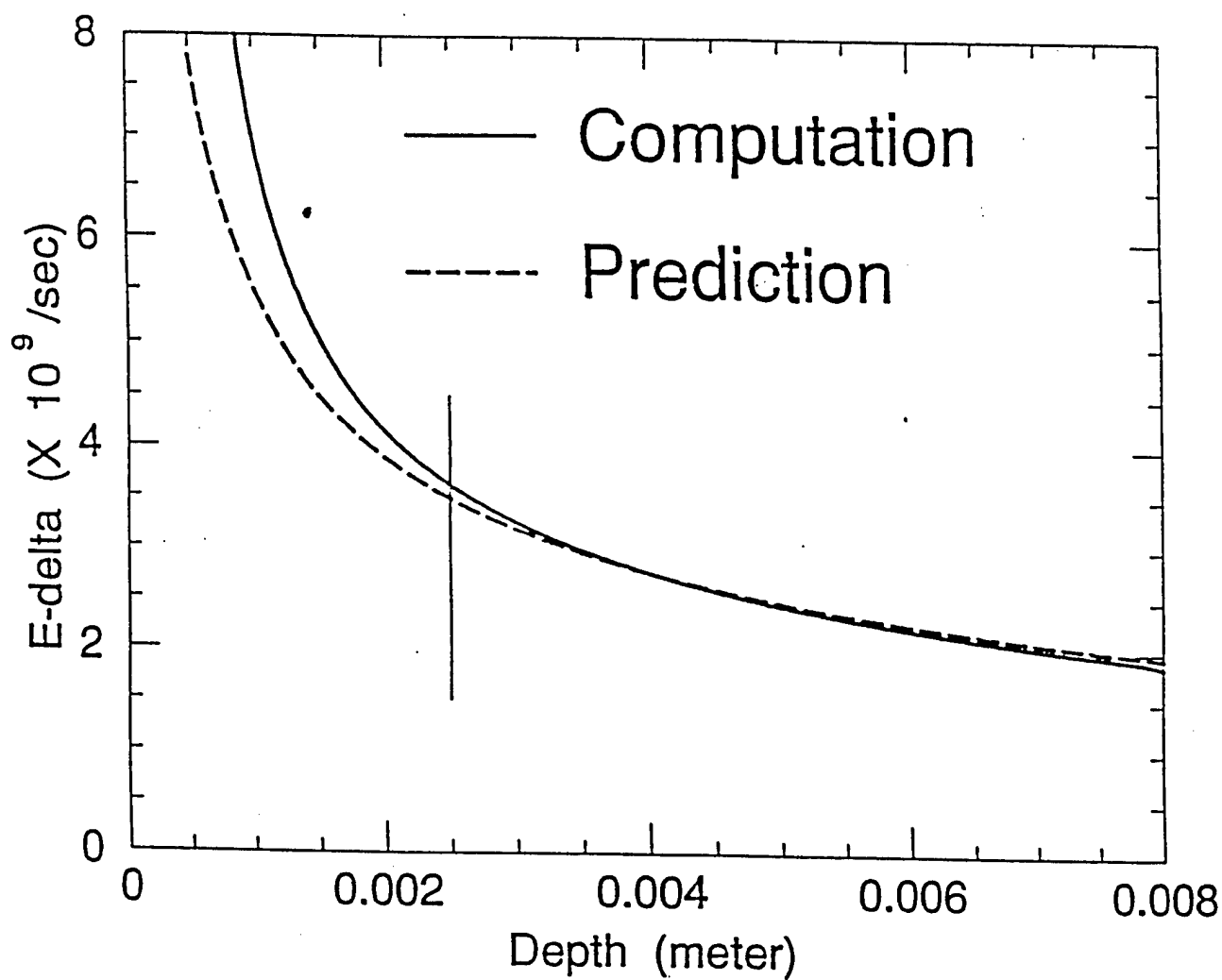


Fig. 11. The predicted and computed decays of the peak field as a function of depth.

constant of proportionality for the $1/\sqrt{z}$ prediction was fit to the data at the center-point (4 mm) of the graph. We note that although the slow speed is achieved very early on ($z \sim 0.1$ mm), it takes some time for the pulse to start diffusing ($z \sim 2.5$ mm). This delay depends on the frequency content of the incident signal, and will be shorter for band-limited pulses. From the discussion and figures it is evident that the envelope and duration of the incident pulse control the magnitude and nature of the response of the medium. Any high-frequency carrier component decays exponentially with depth. Similar behavior was observed in numerical simulations with square pulses of various durations. All long duration pulses were found to travel unattenuated with amplitude $T(\omega = 0) \times \max\{E^{inc}\}$, and square modulated sinusoidal pulses of various carrier frequencies and durations (1 to 10 cycles) behaved like the Green's function with the carrier component exponentially small.

We also checked the sensitivity of our calculations to the way in which we modeled the water data of Ref. 2. Reference 25 points out that many other data sets are available for water, so we were satisfied with any model that fit the data in Ref. 2 to within 10%. In particular, we examined several Debye-model fits to the data in Ref. 2 for frequencies that are below 100 GHz and for which the data are also said, in the reference, to be reliable. Our experience in fitting those data is that ϵ_∞ can be taken to be any number from 1.00 through 10.0, and then values for the two other Debye parameters, ϵ_s and τ , can be found that fit the data to within 10%. In that sense, the value of ϵ_∞ is somewhat arbitrary; for most of our simulations we chose $\epsilon_\infty = 1.00$, which is consistent with an assumption in Ref. 2. The corresponding Debye parameters are $\epsilon_\infty = 1.00$ and $\epsilon_s = 80.35$ and $\tau = 8.13 \times 10^{-12} \text{s}^{-1}$ in the notation of Subsection 2A, or, equivalently, $a = 9.76 \times 10^{12} \text{s}^{-1}$ and $b = 1.23 \times 10^{11} \text{s}^{-1}$ in the notation of (3.13). This fit is referred to as Model 1 in Fig. 12; it is the fit that is used in most of the numerical computations in this paper. Another model that fits the water data to within 10% accuracy is defined by $\epsilon_\infty = 5.50$ and $\epsilon_s = 78.20$ and $\tau = 8.1 \times 10^{-12} \text{s}^{-1}$, or, alternatively, $a = 8.98 \times 10^{12} \text{s}^{-1}$ and $b = 1.23 \times 10^{11} \text{s}^{-1}$. This second model is used only in Fig. 12, where it is called Model 2. The propagation of an incident 5-cycle 8-GHz 1-V/m-amplitude square-modulated sinusoid was computed for these two models. Figure 12 shows the resulting electric field produced at a 9.75-mm depth for both models. We compared the electric fields at 31 other representative

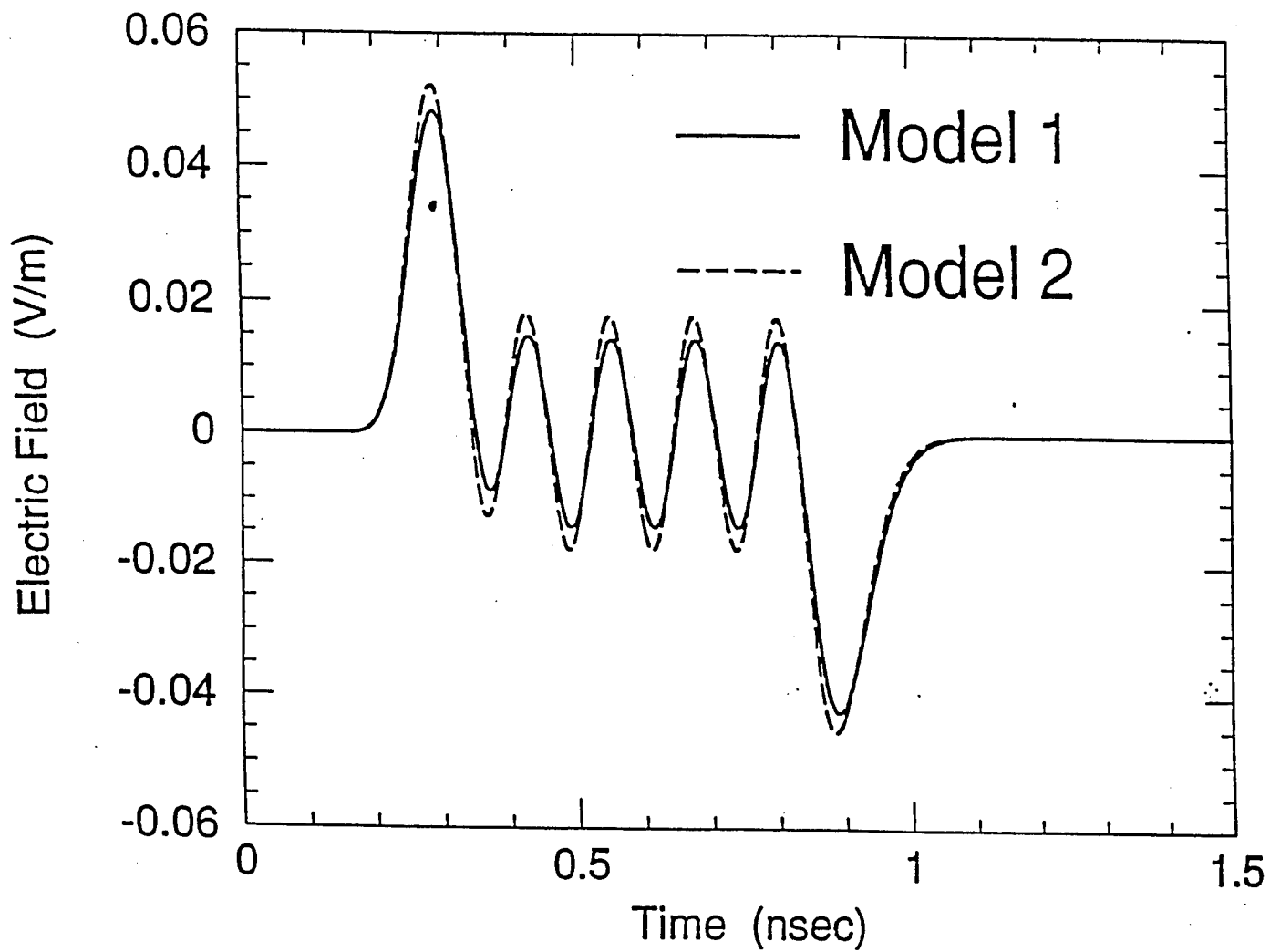


Fig. 12. Electric fields for two models of water. The fields, which result from the same incident pulse, are computed at a 9.75-mm depth for each model.

depths, from 0 cm through 4 cm, and observed similar agreement, commensurate with two different 10%-accuracy fits to the water data. A similar degree of agreement was also seen for the two models in computations for the following incident fields: (1) A 1-cycle 8-GHz square-modulated sinusoid; (2) A 1-cycle 10-GHz square-modulated sinusoid; (3) A 50-psec square pulse; and (4) A 100-psec square pulse. These results are numerical evidence that the computed internal fields are stable as the water model is perturbed by about 10%.

Now we wish to provide an explanation, based on the understanding developed herein, of the observations in Ref. 3 whereas no significant differences in SAR (Specific Absorption Rate) distribution between pulsed and CW (Continuous Wave) exposures were measured for a MEM (Muscle Equivalent Material) exhibiting two relaxation times. The dielectric model was composed of two Debye mechanisms, which fit experimentally determined permittivity and conductivity data for MEM at 2.07, 2.8, 5.6, and 9.3 GHz. The two relaxation times were $\tau_1 = 6.63$ psec, and $\tau_2 = 83.7$ psec. The material was illuminated with a train of square-modulated pulses of various durations and repetition rates. We will explain the observations in Ref. 3 for the smallest pulse repetition rate used (200 pulses per second) for which the pulse duration was $0.5 \mu\text{sec}$. All other results in Ref. 3 with different pulse settings are similarly explained. For this incident signal the author of Ref. 3 used a carrier of 5.6 GHz. Thus, the pulse duration was $T_p = 5 \times 10^{-7}$ sec, the quiescent interval between pulses was $T_q = 5 \times 10^{-3}$ sec, and each pulse contained 2800 cycles of carrier. Further, it happened that $T_p \gg \max\{\tau\} = \tau_2$, thus the medium would not respond in a dispersive manner, rather it exhibited an effective relative permittivity of $\epsilon'_1 + \epsilon'_2 - \epsilon_\infty = 42.4 + 15.8 - 4.3 = 53.9$ to the envelope of the pulses. With these parameter values in mind we expect the medium to sense a CW signal of carrier 5.6 GHz, even in the pulsed case. Since the MEM has low heat diffusivity, i.e., it takes about 40 sec for a temperature change of 0.04°C to occur, its temperature will change immeasurably in the time T_q between pulses. Consequently, the temperature will remain constant until the next pulse arrives again to be seen by the medium as part of a CW exposure, hence the observed indistinguishability of the CW SAR versus the pulsed SAR. As the carrier frequency is increased the CW vs. pulsed exposure SARs should start disagreeing at smaller depths. This is related to the frequency-

dependent skin depth for the carrier component which is 9.7 mm at 5.6 GHz. All the measurements of SAR were obtained at depths well within the skin depth. The effects of the pulsing should be observable at depth greater than $c_0\tau_2 \sim 1.2$ cm since then the carrier component will have decayed sufficiently (it is exponentially decaying as in the CW case) so the remaining field will be due to the square envelope and will behave diffusively.

The results presented in our paper also help in accurately predetermining sample thickness to be used in single and total transmission Time Domain Spectroscopy (TDS) studies such as those presented in Ref. 26. In the single transmission approach one studies the first arrival through a long sample so that the highest frequency components will have decayed sufficiently in order not to mask the lower frequency components which, as we showed in Section 2, are significantly slower (for water $c_1 \sim c_0/9$). The first suggestion arising from the analysis of Section 2 (verified by the numerical simulations) is that the sample can be as short as $2c_0\tau$ when one is interested in measuring the static permittivity of a Debye-like material with single transmission TDS. On the other hand, in the total transmission approach the first arrival time through a short sample is used to best measure the infinite-frequency permittivity of the material under test. Therefore, a sample length shorter than $c_0\tau$ should be appropriate in order to capture the time of arrival of the highest frequencies and thus determine ϵ_∞ . (The next-to-last paragraph of Section 2 has related comments.) For the test case presented in the results section of Ref. 26 [Eqn. (8) there] it happens that $\epsilon_s = 17.3$, $\epsilon_\infty = 3.3$, $\tau = 460$ psec. Thus, the highest frequency components travel with a speed $c_o = 0.5505c$, the lowest frequency components travel with speed $c_1 = 0.2673c$, and $c_o\tau = 7.6$ cm. The experimenters could have used a slab of material of at least 15 cm to reliably measure ϵ_s , and a slab thickness of at most 7 cm to measure ϵ_∞ , instead of using 50 cm and 2.7 cm respectively to do the measurements. In Figure 13 we show the $x-t$ location of the peak of the impulse response for this medium. (The two data points in one corner of the graph are minor numerical artifacts that are related to the similar numerical artifacts in Fig. 7.) The graph as a whole confirms our predictions of the sample lengths with which TDS will be most successful in measuring the permittivities.

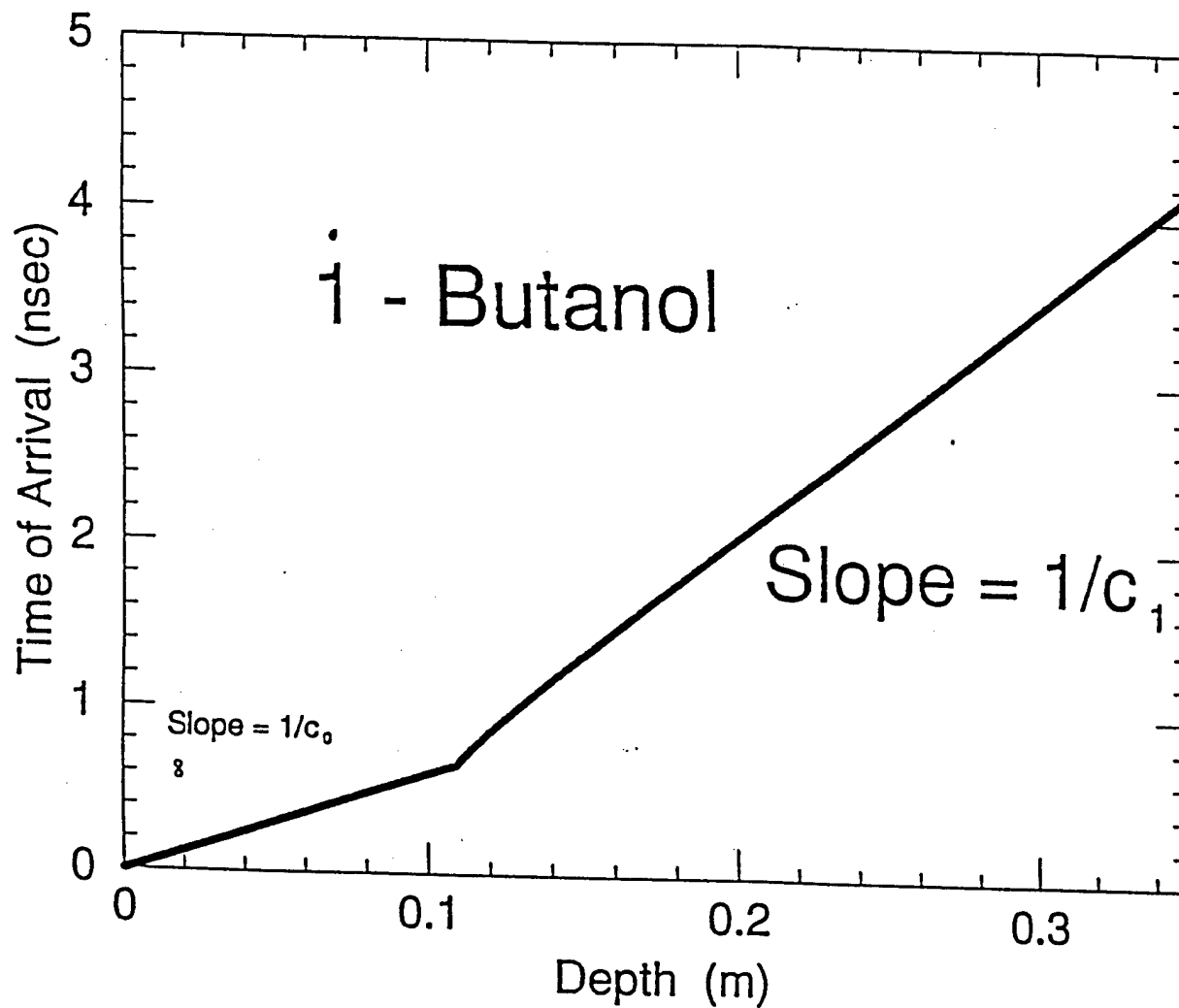


Fig. 13. The time of arrival of the peak of the Green function $G_E(z, t)$ at various depths in the medium of Ref. 26.

5. CONCLUSION

There are many generalized methods for computing the response of any single dispersive medium to any single incident pulse. This paper has contributed nothing along those lines; instead, we have developed several related results that are general in a different way. We have found, for instance, that the power density and the peak amplitude of an incident pulse place upper bounds on the peak amplitude suffered inside a dispersive medium—independent of the other details of the incident pulse. Our Green-function results reduce the computation of such upper bounds to little more than a calculator exercise, and we have given numerical examples in which these sharp upper bounds are almost attained. We have reported similar upper-bound estimates for a quantity related to power density, and for the time derivative of the magnetic field. That time derivative, $\partial_t H$, is largely responsible for electromotive-force currents in circuit-like structures; it is especially large for short-risetime pulses. Such upper bounds could, potentially, help in the regulation of electromagnetic interference or damage produced in dispersive media.

Although our methods apply to dispersive media generally, we have used a Debye model for microwave-pulse propagation in water as a specific numerical example. For that water example, we reported a factor-of-nine effect in the wave speeds that seems to have been unnoticed until now, and we explained this large effect analytically using PDEs. The PDE analysis also yielded simple short-pulse and long-pulse approximations, as did an analysis of the numerical Green functions involved in the upper-bound concepts described earlier. We studied rates of decay in Subsection 2A, and approximations for detailed time traces are given in Subsection 2B and Eqns. (3.2) and (3.4). Section 4 uses that work to explain the results of some laboratory experiments, and to offer suggestions for future experiments.

APPENDIX A: ERROR ESTIMATES

This appendix develops an easily used method for estimating the percentage error in grid-dependent computations. The estimates are validated numerically in some cases for which exact solutions are known, and the estimates are also used in cases for which exact solutions are not known. These estimates use only one of the many definitions of relative error for functions of two variables, but the estimates can easily be adapted to other measures of relative error and to functions of more than two variables. We were motivated to estimate percentage errors because quantitative estimates of uncertainty could help in setting safety standards or in the use of other computations for which measures of numerical uncertainty are vital.

The error estimates in this paper are empirical. The estimates are obtained by computing with several different grid sizes, noticing a pattern in the relative errors of the different computer runs, and using that inferred pattern to sum the series on the right side of the inequality $\|f_c - f_e\|_\infty \leq \|f_c - f_1\|_\infty + \|f_1 - f_2\|_\infty + \|f_2 - f_3\|_\infty + \dots$. The concepts of rate and order of convergence are not used in these empirical estimates. The logic behind the estimates is slightly intricate, but the resulting method uses only least upper bounds and geometric means and geometric series, which are extraordinarily simple concepts.

We will estimate relative errors for functions of two variables. The error in a computed solution $f_c(z, t)$ relative to the exact solution $f_e(z, t)$ can be defined as

$$E_{\text{rel}}[f_c, f_e] = \frac{\|f_c(z, \cdot) - f_e(z, \cdot)\|_\infty}{\|f_e(z, \cdot)\|_\infty}. \quad (\text{A1})$$

The relative error (A1) is a function of the depth z . For instance, if the relative error is known to be less than 1% over a range of depths z , then, for those depths, the exact solution $f_e(z, t)$ can differ from the computed solution $f_c(z, t)$ by no more than 1% of the peak value (with respect to t) of $|f_e(z, t)|$. The just-mentioned peak value of $|f_e(z, \cdot)|$ is unknown in all practical cases in which the exact solution f_e is unknown; however, in the present hypothetical case of 1% relative error, the peak value of the unknown quantity $|f_e(z, \cdot)|$ can differ by no more than 1% from the peak value of the known quantity $|f_c(z, \cdot)|$. A brief derivation involving a geometric series then shows that, in the case of 1% relative error, the graph of the exact solution

$f_c(z, t)$ is guaranteed to fall between the graph of $f_c(z, t) + 1.01\% \|f_c(z, \cdot)\|_\infty$ and the graph of $f_c(z, t) - 1.01\% \|f_c(z, \cdot)\|_\infty$. The quantities $\pm 1.01\% \|f_c(z, \cdot)\|_\infty$ are called error bars.

We will now go step by step through the error estimates illustrated in Fig. 14. Those estimates are for Green-function computations of waves normally incident on water. The computations were done for five different grids, and the results are called $f_1(z, t), f_2(z, t), \dots, f_5(z, t)$ in order of the increasing fineness of the grids. Because of computer limitations, the finer-grid computations were done for shallower depths than were the coarser-grid computations. For zero depth, the light circles on the $z = 0$ axis of Fig. 14 represent $\|f_1(0, \cdot) - f_2(0, \cdot)\|_\infty / \|f_5(0, \cdot)\|_\infty$, $\|f_2(0, \cdot) - f_3(0, \cdot)\|_\infty / \|f_5(0, \cdot)\|_\infty$, $\|f_3(0, \cdot) - f_4(0, \cdot)\|_\infty / \|f_5(0, \cdot)\|_\infty$, and $\|f_4(0, \cdot) - f_5(0, \cdot)\|_\infty / \|f_5(0, \cdot)\|_\infty$, running from top to bottom along the vertical axis. For instance, the error in $f_4(0, t)$ relative to the most finely computed result $f_5(0, t)$ is 0.157%. The even spacing of the four light circles along the logarithmic, vertical axis of Fig. 14 suggests that the four relative errors are in geometric progression; in fact, the ratio of the second-largest relative error to the largest relative error is 0.368, the ratio of the next two smaller relative errors is 0.284, the ratio of the two smallest relative errors is 0.268, and the geometric mean of the three previous numbers is 0.304. For those reasons we assume

$$\frac{\|f_{n+1}(0, \cdot) - f_{n+2}(0, \cdot)\|_\infty}{\|f_5(0, \cdot)\|_\infty} \approx (0.304)^n \frac{\|f_1(0, \cdot) - f_2(0, \cdot)\|_\infty}{\|f_5(0, \cdot)\|_\infty}, \quad (A2)$$

even for hypothetical results, such as f_{100} , which would come from computations involving a much-finer grid than was used for the actual computation of f_5 . We also assume that the exact result $f_c(z, t)$ is the $n \rightarrow \infty$ limit of $f_n(z, t)$. The triangle inequality for norms then implies $\|f_1 - f_c\|_\infty \leq \|f_1 - f_2\|_\infty + \|f_2 - f_3\|_\infty + \|f_3 - f_4\|_\infty + \dots$. We use (A2) in the right side of the previous inequality to get a geometric series, which sums to

$$\frac{\|f_1(0, \cdot) - f_c(0, \cdot)\|_\infty}{\|f_5(0, \cdot)\|_\infty} \lesssim \frac{1}{1 - 0.304} \frac{\|f_1(0, \cdot) - f_2(0, \cdot)\|_\infty}{\|f_5(0, \cdot)\|_\infty} = 8.08\% \quad (A3)$$

at $z = 0$. That 8.08% estimated relative error is plotted as the top-most heavy circle on the vertical axis of Fig. 14. The analysis was repeated for the relative errors of other computations f_i , yielding

$$\frac{\|f_i(0, \cdot) - f_e(0, \cdot)\|_\infty}{\|f_5(0, \cdot)\|_\infty} \lesssim 1.44 \frac{\|f_i(0, \cdot) - f_{i+1}(0, \cdot)\|_\infty}{\|f_5(0, \cdot)\|_\infty}, \quad (A4)$$

for $i = 1, 2, 3, 4$. Those estimated relative errors are also plotted as heavy circles on the vertical axis of Fig. 14.

Reference 9 has an exact, closed form, modified-Bessel-function expression of the zero-depth Green function for a half-space of Debye medium. That exact solution f_e was used to compute the true relative errors $E_{rel}[f_i, f_e]$ at $z = 0$. Those true relative errors are plotted as the bold Xs on Fig. 14. The true relative errors (bold Xs) validate the error estimates (bold circles) because the two sets of errors match closely; for instance, the error estimate (A4) for $f_3(0, \cdot)$ was that there would be 0.844% error relative to f_e , and the actual error in $f_3(0, \cdot)$ relative to f_e was 0.797%. Our percentage-error method involving geometric means and geometric series is thereby validated.

The relative errors $\|f_i(z, \cdot) - f_{i+1}(z, \cdot)\|_\infty / \|f_5(z, \cdot)\|_\infty$ were then computed at the depths $z = 0.480$ mm, 1.04 mm, 1.52 mm, and 2.00 mm, for $i = 1, 2, 3, 4$. Those results are plotted as some of the light circles to the right of the vertical axis in Fig. 14. Error estimates for $f_3(z, \cdot)$ were computed using the geometric-series technique in (A2)–(A4), with the results plotted as several bold asterisks on Fig. 14. The ratios of relative errors and the geometric means of the ratios were computed separately for each depth. In particular, the geometric means for the four depths mentioned in this paragraph are 0.302, 0.328, 0.315, and 0.333 for 0.480 mm through 2.00 mm, consecutively. We will now explain how the relative errors for depths beyond 2.00 mm were computed.

The finest-discretization run was not computed beyond 2.00 mm for reasons related to computer resources. Thus, only f_1 , f_2 , f_3 , and f_4 were analyzed for the depths from 2.48 mm through 4.00 mm. These analyses were done as described in the previous paragraph, and the geometric means were also computed separately for each depth. Similarly, the runs f_1 , f_2 , and f_3 were analyzed for depths from

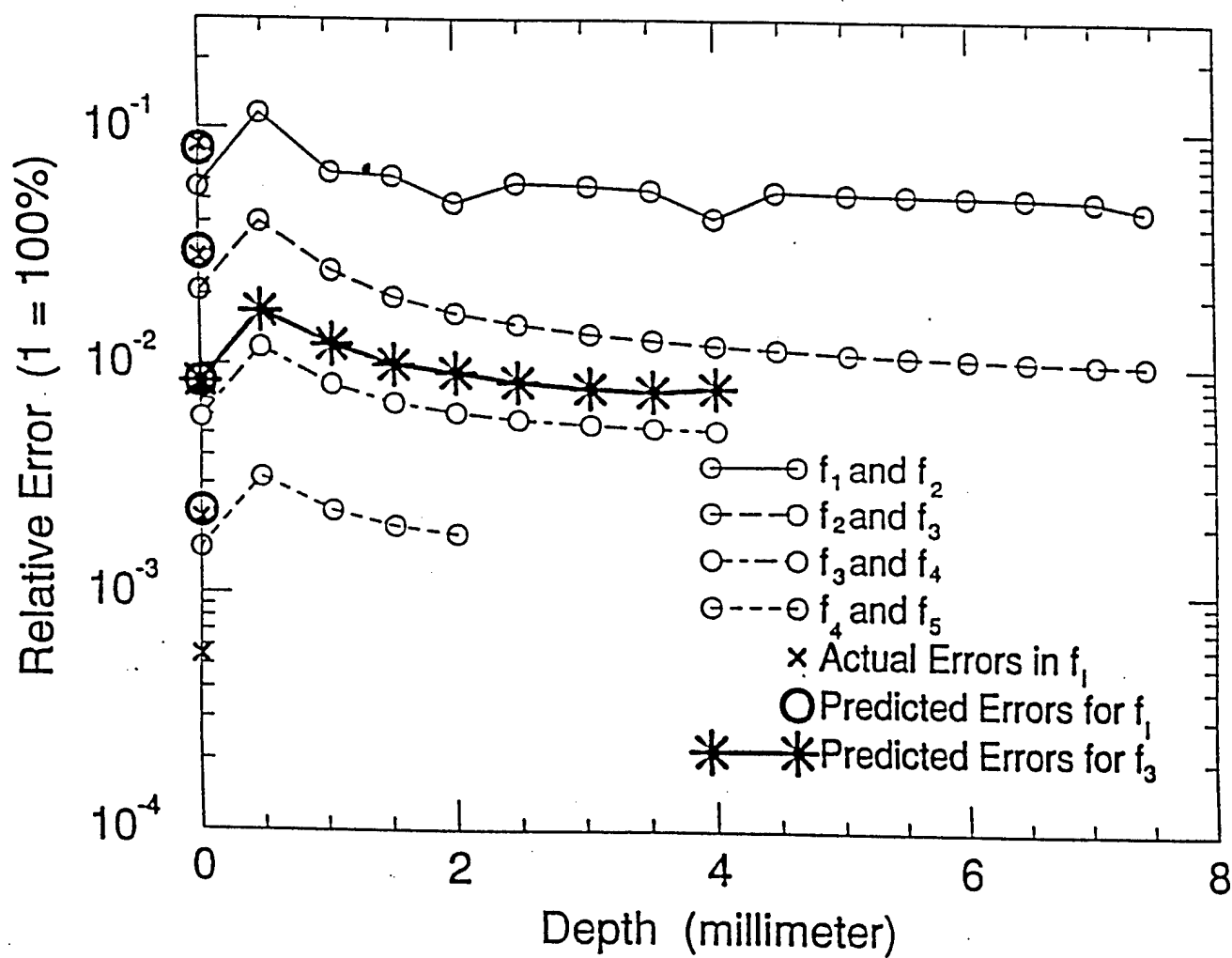


Fig. 14. Relative errors for the computation of G_E for water. The bold marks represent the final error estimates and their numerical validations. The lighter marks represent intermediate steps in the computation of error estimates.

5.04 mm through 7.04 mm. In these computations, and in all other computations described in this appendix, the L_∞ norms were computed using 90 evenly spaced time points.

The final result in Fig. 14 is symbolized by the bold asterisks there. The result is that $f_3(z, t)$ has errors relative to f_e that are expected to fall monotonically from about 1.70% at $z = 0.480$ mm to about 0.799% at $z = 4.00$ mm. The error in $f_3(0, t)$ relative to $f_e(0, t)$ is actually 0.797%. Figure 14 shows that the relative errors are non-monotonic from 0.00 mm through 0.500 mm; therefore, we make no further inferences about the relative errors in that first half-millimeter.

REFERENCES

- [1] J. C. Lin and C. K. Lam, "Coupling of Gaussian electromagnetic pulse into a muscle-bone model of biological structure," *J. Microwave Power* 11, 67-75 (1976).
- [2] J. D. Jackson, *Classical Electrodynamics* 2nd ed., (Wiley, New York, 1975). See Secs. 7.5e, 7.7, and 7.11g.
- [3] W. D. Hurt, "Measurement of specific absorption rate in human phantoms exposed to simulated Air Force radar emissions," USAFSAM-TR-84-16 (June 1984) (Armstrong Laboratory, Brooks AFB, TX, 1984).
- [4] W. D. Hurt, "Multiterm Debye dispersion relations for permittivity of muscle," *IEEE Trans. Biomed. Engnr.* BME-32, 60-64 (1985).
- [5] *IEEE Standard for Safety Levels with Respect to Human Exposure to Radio Frequency Electromagnetic Fields, 3kHz to 300 GHz*, IEEE C95.1-1991 (IEEE Standards Board, New York, 1991).
- [6] P. Debye, *Polar Molecules* (Dover, New York, 1929). See p. 90.
- [7] F. John, *Partial Differential Equations*, 4th ed. (Springer-Verlag, New York, 1991). See pp. 152 and 160.
- [8] G. B. Whitham, *Linear and Nonlinear Waves* (New York, Wiley, 1974).
- [9] R. S. Beezley and R. J. Krueger, "An electromagnetic inverse problem for dispersive media," *J. Math. Phys.* 26, 317-325 (1985), Sec. IV. Equate their function $R(t)$ with our $G_E(0, t)$. See also our Eqn. (3.12).
- [10] J. A. Stratton, *Electromagnetic Theory* (McGraw-Hill, New York, 1941) Sec. 2.19. From (11) and $E_{inc} = f(t - z/c)$, one can show that the incident power density of the electric part $f(t)$ of an incident pulse is $(\epsilon_0/2) \int_{-\infty}^{\infty} dz |f(z/c)|^2 = (c\epsilon_0/2) \int_{-\infty}^{\infty} dt |f(t)|^2 = (c\epsilon_0/2) [\|f(\cdot)\|_2]^2$, whose mks units are Watt/m².

- [11] T. M. Roberts, "Causality Theorems," in *Invariant Imbedding and Inverse Problems*, J. P. Corones, G. Kristensson, P. Nelson, and D. L. Seth, eds. (Society for Industrial and Applied Mathematics, Philadelphia, Pa., 1992), pp. 114, 121, and 122-123.
- [12] E. Zauderer, *Partial Differential Equations of Applied Mathematics* (Wiley, New York, 1983), pp. 218-223 and 615-618.
- [13] R. J. Krueger and R. L. Ochs, Jr., "A Green's function approach to the determination of internal fields," *Wave Motion* **11**, 525-543 (1989).
- [14] R. Krueger and R. Winther, "Internal field, inhomogeneous dispersive medium" and other unpublished notes and computer programs, Ames Laboratory, Ames, Iowa 50011 (personal communication, 1989).
- [15] G. Kristensson, "Direct and inverse scattering problems in dispersive media — Green's functions and invariant imbedding techniques," in *Direct and Inverse Boundary Value Problems*, Vol. 37 of *Methoden und Verfahren der mathematischen Physik*, R. Kleinman, R. Kress, and E. Martensen, eds. (Peter Lang, Frankfurt, Germany, 1991).
- [16] T. M. Roberts and M. Hobart, "Energy velocity, damping, and elementary inversion," *J. Opt. Soc. Am. A* **9**, 1091-1101 (1992).
- [17] A. Karlsson, H. Otterheim, and R. Stewart, "Transient wave propagation in composite media: Green's function approach," *J. Opt. Soc. Am. A* **10**, 886-895 (1993).
- [18] M. Reed and B. Simon, *Methods of Modern Mathematical Physics II: Fourier Analysis, Self-Adjointness* (Academic, New York, 1975), pp. 28, 29, and 32.
- [19] C. E. Baum, "EMP simulators for various types of nuclear EMP environments: An interim categorization," *IEEE Trans. on Antennas and Propagat.* **26**, 35-53 (1978). See Sect. II.
- [20] J.-Y. Chen and O. P. Gandhi, "Currents induced in an anatomically based model of a human for exposure to vertically polarized electromagnetic pulses," *IEEE Trans. Microw. Theor. Tech.* **39**, 31-39 (1991). See Figs. 3(a) and 4.

- [21] F. M. Tesche, "Prediction of the E and H fields produced by the Swiss mobile EMP simulator (MEMPS)," *IEEE Trans Electromagn. Compat.* 4, 381-390 (1992). See Figs. 7, 10(a), 13(b), and 15(b).
- [22] In Sec. 7.11g of Ref. 2, take large-depth limits while keeping the relative time $|t - t_1|$ fixed. Then use (7.146)-(7.148), (7.141), and (3.89) to show that the large-depth, fixed-relative-time values of the Brillouin precursor decay as $(\text{depth})^{-1/3}$ if the frequency-domain amplitude $A(\omega)$ is nonzero at $\omega = 0$, and that the values decay as $(\text{depth})^{-2/3}$ if $A(\omega)$ has a first-order zero at $\omega = 0$. The error is $O(\omega^4)$.
- [23] R. M. Joseph, S. C. Hagness, and A. Taflove, "Direct time integration of Maxwell's equations in linear dispersive media with absorption for scattering and propagation of femtosecond electromagnetic pulses," *Optics Letters* 16, 1412-1414 (1991).
- [24] F. J. German, "The analysis of pulse propagation in linear dispersive media with absorption by the finite-difference time-domain method," unpublished report and computer program, Department of Electrical Engineering, Auburn University, Auburn, Alabama 36849 (personal communication, 1993).
- [25] M. R. Querry, D. M. Wieliczka, and D. J. Segelstein, "Water (H_2O)," in *Handbook of Optical Constants of Solids II*, Edward D. Palik, ed. (Academic Press, Boston, 1991), pp. 1059-1065.
- [26] B. Geelblom and E. Noreland, "Transmission Methods in Dielectric Time Domain Spectroscopy," *J. Phys. Chem.* 81, 782-788 (1977).

STINFO OFFICE
ARMSTRONG LABORATORY/OEPP
2402 E DRIVE
BROOKS AFB TX 78235-5114

OFFICIAL BUSINESS